MODEL IDENTIFICATION AND MODEL BASED ANALYSIS OF MEMBRANE REACTORS

Dissertation

zur Erlangung des akademischen Grades

Doktoringenieur

(Dr.-Ing)

von M. Sci. Fan Zhang

geb. am 26. December 1977 in Tianjin, China

genehmigt durch die Fakultät für Elektrotechnik und Informationstechnik

der Otto-von-Guericke-Universität Magdeburg

Gutachter: Prof. Dr.-Ing. Achim Kienle

Prof. Dr.-Ing. Andreas Seidel-Morgenstern

Dr.-Ing. Michael Mangold

Promotionskolloguium am 13. October 2008

Forschungsberichte aus dem Max-Planck-Institut
für Dynamik komplexer technischer Systeme

Band 24

Fan Zhang

Model Identification and Model Based Analysis of Membrane Reactors

Shaker Verlag
Aachen 2008

Bibliographic information published by the Deutsche Nationalbibliothek
The Deutsche Nationalbibliothek lists this publication in the Deutsche Nationalbibliografie; detailed bibliographic data are available in the Internet at http://dnb.d-nb.de.

Zugl.: Magdeburg, Univ., Diss., 2008

Printed in Germany.

ISBN 978-3-8322-7727-7
ISSN 1439-4804

Shaker Verlag GmbH • P.O. BOX 101818 • D-52018 Aachen
Phone: 0049/2407/9596-0 • Telefax: 0049/2407/9596-9
Internet: www.shaker.de • e-mail: info@shaker.de

Kurzzusammenfassung

Diese Arbeit beschäftigt sich mit Fragestellungen der Modellidentifikation und modellgestützten Analyse von Membranreaktoren.

Im ersten Teil der Arbeit werden Probleme der Parameteridentifikation und der optimalen Versuchsplanung für den Gastransport in porösen Membranen mit einer oder mehreren Schichten untersucht. Ein genetischer Algorithmus wird verbessert, um die auftretenden globalen Optimierungsprobleme zu lösen. Im zweiten Teil der Arbeit werden die stationären Lösungen verschiedener Membranreaktormodelle einer nichtlinearen Analyse unterzogen, und die Bildung örtlicher Muster wird studiert.

In Kapitel 2 werden die Membranreaktormodelle, die in der Arbeit verwendet werden, vorgestellt und kurz diskutiert.

Die Identifikation eines Mehrschichtmembranmodells, die im Zentrum des ersten Teils der Arbeit steht, stellt ein schwieriges globales Optimierungsproblem dar. Kapitel 3 beschäftigt sich mit methodischen Ansätzen zur Lösung dieses Problems. Da die auftretenden Gütefunktionale nicht-konvex sind, ist ein traditionelles lokales und gradientenbasiertes Optimierungsverfahren nicht in der Lage, das Minimum des Gütefunktionals korrekt zu lokalisieren. Deshalb sollte ein globales Optimierungsverfahren verwendet werden. In dieser Arbeit wird zunächst ein genetischer Algorithmus aus der Literatur eingesetzt. Es zeigt sich

jedoch, dass dieser Algorithmus unbefriedigende Ergebnisse liefert, wenn die zu identifizierenden Parameter korreliert sind. Kapitel 3 diskutiert numerische Algorithmen zur Parameteridentifikation und Versuchsplanung und konzentriert sich dann auf die Verbesserung des genetischen Algorithmus, um die hier auftretenden Optimierungsprobleme zu lösen. Eine neue Variante des genetischen Algorithmus, die Koordinatentransformationen einsetzt, wird vorgestellt.

In Kapitel 4 wird das Dusty-Gas-Modell für den Gastransport durch eine keramische Einschichtmembran benutzt, um die Effizienz sechs verschiedener Identifikationsexperimente zu vergleichen. Ein dynamisches Experiment mit einem Gasgemisch liefert die besten Ergebnisse. Die Untersuchung wird dann auf die Identifikation einer Mehrschichtmembran ausgedehnt. Die Analyse eines idealisierten Zweischichtmembranmodells, die zuerst durchgeführt wird, zeigt, dass es möglich ist, die Parameter beider Schichten gleichzeitig zu identifizieren. Die Transportparameter einer metallischen Zweischichtmembran werden dann aus experimentellen Daten ermittelt. Das Zweischichtmodell der Membran zeigt dabei bessere Übereinstimmung mit dem Experiment als ein Einschichtmodell, das zu Vergleichszwecken eingesetzt wird.

Kapitel 5 konzentriert sich auf die nichtlineare Analyse eines Membranreaktors. Ein Membran-Rohrreaktor mit idealer Pfropfenströmung wird mit Hilfe numerischer Bifurkationsanalyse untersucht. Hopfbifurkationen und reelle Bifurkationen werden detektiert. Bei der Fortsetzung periodischer Lösungen wird eine Periodenverdopplungssequenz beobachtet, die zu einer chaotischen Lösung führt. Im zweiten Teil des Kapitels wird der Einfluss der axialen Wärmeleitfähigkeit diskutiert. Schließlich wird ein detaillierteres Membranreaktormodell betrachtet, das eine verfeinerte Reaktionskinetik und ein komplexeres Modell für den Stofftransport in der Membran enthält. Die Simulationsergebnisse mit diesem Modell deuten darauf hin, dass es möglich sein sollte, die simulierten räumlichen Muster auch in einem Labormembranreaktor zu beobachten.

Abstract

This work considers problems of model identification and model based analysis of membrane reactors. The parameter identification and optimal experimental design problems for gas transport through both single and multi-layer membranes have been investigated. A genetic algorithm has been improved to solve the corresponding global optimization problems. Nonlinear analysis has been performed for the steady state solution of membrane reactor models, and pattern formation has been studied.

In chapter 2, the membrane reactor models considered in this work are introduced and discussed briefly.

The identification of multi-layer membrane models, which is the focus of the first part of this work, is a difficult global optimization problem. Chapter 3 discusses methods for solving this problem. Since the objective function is non-convex, a traditional gradient based *hill climbing* algorithm is unable to locate the minima correctly. Therefore a global optimizer should be applied instead. However, the genetic algorithm that is used in this work becomes also inefficient in solving this problem because of the high correlation of the parameters. Chapter 3 first gives background of numerical algorithm for parameter identification and experimental design, and then is focused on improving the efficiency of genetic algorithm to solve the demanding global optimization problems. A new method with coordinate transformation is developed and applied successfully to the problems in chapter 4.

In chapter 4, the dusty gas model of gas transport through a homogeneous ceramic membrane is used to compare the efficiency of different experimental schemes. The proposed multi-component gas dynamic transport experiment gives the best result. The research is then extended to the identification of a multi-layer membrane. The analysis of an idealized two-layer membrane model, which is performed first, indicates that it is possible to identify the parameters of both layers simultaneously. The properties of a real metallic membrane are then identified from experimental data by using a two-layer membrane model. The two-layer model shows better agreement with experimental data than a single-layer model that is used for comparison.

Chapter 5 is focused on the nonlinear analysis of the membrane reactor. An ideal plug flow membrane reactor is investigated by numerical bifurcation analysis in DIVA. Hopf bifurcation as well as real bifurcation points are located. By continuation of periodic solutions, period doubling sequence is observed which leads to chaotic solution. The influence of the heat dispersion coefficient λ is also discussed. Finally a more detailed model of a fixed bed membrane including both detailed reaction kinetics and mass transfer model is considered. The simulation results show it's possible to observe the pattern formation under feasible operation conditions in a laboratory membrane reactor.

Acknowledgments

First and foremost, I wish to express my sincere gratitude to advisor Dr.-Ing. Michael Mangold who actually leads me into this research area and gives me enormous kind advice. His patient and tireless guidance makes the possibility for this paper to be finished. What I appreciate the most is his strict working attitude, which help me to correct even small grammar errors.

I also wish to express my appreciation and gratitude to Prof. Dr.-Ing Achim Kienle for giving me the opportunity to conduct research in this interesting research area and for providing me constructive suggestions and guidance during my work. His help and support was essential for the completion of this work.

I would also thank Prof. Dr.-Ing. E. Tsotsas for inspiring discussions, and his Ph.D. student Velislava Edreva, who was working on the experimental identification of membrane reactor and provided most of the experimental data in this work. I would also give special thanks to Michael Krasnyk, who helped me to solve the program problems in Diana system. Without their help, the corresponding parts of this work could never be finished.

I must also thank to some former colleagues: Dr. Arshad Hussain, Dr. Konstantin Teplinskiy, Dr. Martin Ginkel, Mr. Sergy gogolenko, and Mr. Imran Farooq, who have also helped me extensively on experiments and programming works. I am specially thankful to my office colleague Min Sheng and René Schenkendorf as well as Carolyn Mangold for their help and support in my life during my stay in Magdeburg.

I wish, furthermore to acknowledge the help received from all other colleagues in PSPD group and Max-Plank-Institute for their support and comprehensive discussions. my former office colleague

Last but not least, I am happy to express my thanks to my family and my girl friend, support and understanding from my far away homeland, which deserve to be mentioned specially.

List of Symbols

B_0	permeability constant in dusty gas model (m^2)
B_f	logarithm permeability constant
$C_{0,i}$	concentration of component i in annulus side of a membrane reactor ($mol.m^{-3}$)
$C_{0,i,in}$	input concentration of component i in annulus side of a membrane reactor ($mol.m^{-3}$)
C_i	concentration of component i ($mol.m^{-3}$)
$C_{i,in}$	input concentration of component i ($mol.m^{-3}$)
C_P	heat capacity ($J.Kg^{-1}.K^{-1}$)
D	diffusion coefficient ($m^2.s^{-1}$)
D_L	Lyapunov dimension
d_P	average pore diameter of a porous membrane(m)
dV	volume of a fluid element in fixed bed side of a membrane reactor (m^3)
dz	length of a fluid element in fixed bed side of a membrane reactor (m)
$f(H)$	the mean fitness of the chromosomes in H
$\bar{f}(t)$	the mean fitness of the whole population at generation t
F_0	ratio of effective to molecular diffusion coefficient
F_n	Fisher information matrix

h_i	molar enthalpy of component i ($J.mol^{-1}$)
$h_{i,ref}$	reference molar enthalpy of component i ($J.mol^{-1}$)
H	the given schema/hyperplane
$\Delta(H)$	the definition length of the schema
$\Delta_R H$	reaction heat ($J.mol^{-1}$)
$j_{D,i}$	dispersive mass flow of component i ($kg.s^{-1}.m^{-3}$)
J_i	molar flux density of component i through a membrane ($mol.s^{-1}.m^{-2}$)
k	reaction prefactor ($mol.Kg^{-1}.h^{-1}$)
K	constant in Langmuir Hinshelwood mechanism ($l.mol^{-1}$)
K_0	Knudsen coefficient in dusty gas model (m)
K_f	logarithm Knudsen coefficient
L	length of a reactor (m) / likelihood function
$m(H,t)$	the proportion of the population that is within hyperplane H at generation t
M_i	molar mass of component i ($Kg.mol^{-1}$)
M_{rot}	one step transfer matrix in GACT
M_{tol}	total transfer matrix in GACT
$\dot{N}_i$	molar flux ($mol.s^{-1}$)
$(\dot{N}_i)_{mem}$	molar flux through membrane in a membrane reactor ($mol.s^{-1}$)
$O(H)$	the order of the schema
P	pressure (Pa)
P_c	the crossover probability
P_m	the mutation probability
$\dot{q}_{in}$	molar flux in CSTR ($mol.s^{-1}$)

r	reaction rate ($mol.Kg^{-1}.h^{-1}$)
$r_{mem,in}$, r_{mi}	inner radius of a membrane (m)
$r_{mem,out}$, r_{mo}	outer radius of a membrane (m)
$r_{mem,wall}$	radius of the shell of a membrane (m)
$r_{m,k}$	radius of the k th layer of a multi-layer membrane (m)
R	correlation coefficient
s	score funciton
S	cross-section area of fixed bed side of a membrane reactor (m^2)
S_{mem}	exchange area of membrane (m^2)
t	time (s)
T	temperature (K)
T_0	temperature in annulus side of a membrane reactor (K)
$T_{0,in}$	input temperature in annulus side of a membrane reactor (K)
T_{in}	input temperature in fixed bed side of a membrane reactor (K)
T_{ref}	reference temperature (K)
T_{wall}	temperature of heating wall of a membrane reactor (K)
u	input signal of a model / flow velocity ($m.s^{-1}$)
u_0	flow velocity in annulus side of a membrane reactor ($m.s^{-1}$)
V	volume of a reactor (m^3)
w_{ik}	weighting factor
x_i	molar fraction of component i
y	measurement value of model output
y_m	model output

z	axial coordinate of membrane reactor
α	heat transfer coefficient ($W.m^{-2}.K^{-1}$)
α_{mem}	heat transfer coefficient of the membrane ($W.m^{-2}.K^{-1}$)
ϵ	porosity of a membrane/void-fraction of catalyst
η	dynamic viscosity ($N.s.m^{-1}$)
$\hat{\theta}$	identified parameter by GA
$\hat{\theta}^*$	identified parameter by ideal optimizer
λ	Lyapunov exponent
λ_{fl}	heat dispersion coefficient of fixed bed side ($W.m^{-1}.K^{-1}$)
λ_{sw}	heat dispersion coefficient of sweep gas side ($W.m^{-1}.K^{-1}$)
μ_{ij}	model output with real paramters
ν_{ij}	stoichiometric coefficient
ρ_f	density of fluid ($kg.m^{-3}$)
$(\rho C_p)_f$	heat capacity of fluid ($J.m^{-3}.K^{-1}$)
$(\rho C_p)_{tol}$	total heat capacity ($J.m^{-3}.K^{-1}$)
ρ_{cat}	density of catalyst ($kg.m^{-3}$)
σ_{ij}	standard deviation of output noise
Σ_v	diffusion volume
τ	tortuosity of membrane

Contents

Chapter 1

Introduction

1.1 Membranes

A membrane is a discrete, thin interface that moderates the permeation of chemical species in contact with it [1]. The interface could be homogeneous or heterogeneous, dense or porous, nevertheless the key feature of a membrane is the ability to control the permeation rate. The most common application of membranes are separation processes for liquids, including microfiltration, ultrafiltration and reverse osmosis. The concept for such processes is quite similar to that of the conventional filtration: particles larger than the pores in membrane are completely rejected, and particles smaller than the pores in membrane can pass through. Another membrane process for liquids is electrodialysis, in which charged membrane are used to separate ions from aqueous solutions driven by electrical potential difference. All the above membrane processes for liquids are well developed separation technologies and already have broad applications in industry. The membranes for such processes are mostly organic polymers, which are also the conventional materials for all commercial membranes.

Membrane processes for gas separation, which are the focus of this work, have developed very fast in recent years. Some companies provide membranes to separate nitrogen from air or carbon dioxide from methane. Most of the commercial membranes for such processes are also polymer membranes. However, in this work, the research is focused on the gas transport through inorganic membranes. The inorganic membranes are until now mainly studied in laboratories, but many advantages over traditional polymer membranes have been reported [2]. One important advantage of inorganic membranes is their thermal stability. The operable temperature limit of inorganic membrane is much higher than that of polymer membranes, which makes the inorganic membranes more suitable for constructing chemical reactors where exothermic reactions happen.

The inorganic membrane can be further divided into porous and dense, homogeneous or multi-layer, and catalytic or inert. In this work the research is restricted to the porous, inert inorganic membranes. Usually a composite membrane is designed to combine a *selective layer*, which is supposed to dominate the transport behavior, and a *support layer* which provides the physical strength to the membrane. Some intermediate layers may be introduced between the two layers to make the whole membrane coherent. Such membrane is also called *asymmetric* membrane, because it's been proved that the gas flow rates with different flow directions are asymmetric [3]. The asymmetric flow effect, although up to now just a byproduct of composite membranes, could become an important factor for design of membrane in the future, since both the selective product removal and distributed injection operation schemes for membrane reactor may require some membrane that prefer a certain mass flow direction.

It should be noted that the discrimination between support layer and selective layer of composite membrane is not absolute. The support layer, although much more porous than the selective layer, could also take important effect on transport phenomena, since it's also much thicker than the selective layers and the transport rate of species through a membrane

is proportional to the inverse of the membrane thickness. The multi-layer membrane will show more distinct characteristics compared to the homogeneous membrane only when each layer possess similar influence to the change of gas flow rate. The mass transfer coefficient for each layer of a composite membrane can be identified simultaneously only when the composite membranes show features that recognizably different from any homogeneous membrane.

1.2 Membrane reactors

The membrane reactors are multi-functional process units, which combine reaction and separation in one apparatus. The class of membrane reactors studied in this work is composed of a catalytic fixed bed, a porous membrane, and an annulus side outside the membrane, see figure 1.1. A membrane reactor may be superior to the conventional reactors by offering advantages with respect to yield, selectivity, and energy integration [4].

There are two principle operation schemes for membrane reactors. The first one is to selectively remove some reaction product of an equilibrium limited reaction, and thus force the reaction balance to move to the right-hand side as is shown in figure 1.1-a. The second one, on the contrary, is to feed the reactant through the membrane into the reactor as is shown in figure 1.1-b. The main advantage of supplying the reactants through the membrane rather than only with the feed is to keep the concentration of some reactant at the optimal value, so that both the conversion rate and selectivity could be maintained at high level [5, 6, 7, 8]. By changing the permeability of the membrane or the concentration of the reactants supplied through the membrane, one may be able to create an optimal concentration profile of reactants along the reactor coordinate and thus to maximize the yield of the reaction.

One important application of the second operation scheme is to improve the performance of partial oxidation reactions [9]. In this work, the oxidative dehydrogenation of ethane is

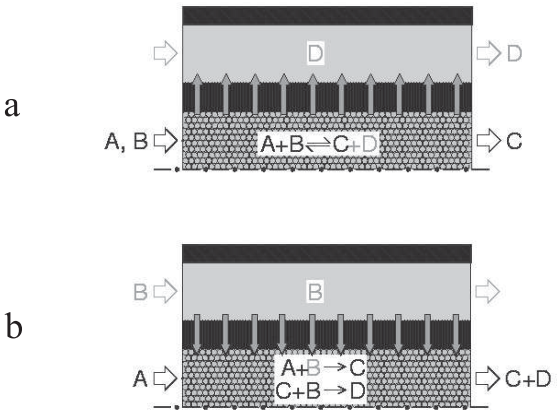

Figure 1.1: Two main operation schemes of the membrane reactor: a - selective removal of the reaction product; b - supplying reactants through the membrane

investigated. However, the purpose of studies in this work is not to improve the conversion-selectivity behavior, but to discuss the possibility of a special nonlinear behavior - the formation of stationary patterns along the membrane reactor.

1.3 Objectives

The modeling of membrane is a demanding but valuable task for understanding these complicated, highly integrated processes. Since the membrane reactor has a more complex structure than traditional reactors, one can expect to observe more complex and non-intuitive behaviors. The model of membrane reactor becomes also an essential tool for process control, process design and process analysis.

The task of model development can be divided into two parts:

1. Choice of a suitable model structure and suitable model equations

2. Determination of unknown model parameters

In this work, the task of model development is focused on the model of mass transfer through a porous membrane. Since the Dusty Gas Model(DGM) is already proven to be a successful model for describing the mass transfer phenomenon, the model identification problem is simplified to parameter identification problem.

The DGM equation uses some lumped parameters which could not be obtained by direct observation of the microscopical structure of the membrane. Therefore, some experiments such as the steady state gas permeation, isobaric diffusion or transient diffusion should be performed in order to identify the transport coefficients of the membrane experimentally. Identifications of single layer membranes have been investigated extensively [10, 11, 12]. Identifications of multi-layer membranes have also been studied [3, 13], but usually performed layer by layer.

The DGM for single gas transport through a single layer membrane leads to a linear model, therefore by using the least-square criteria the identification problem could be solved explicitly by linear regression. In this work we consider a more complex situation that transport coefficients for multi-layer membrane must be identified simultaneously. The parameter identification and experimental design problems are discussed in chapter 4. The most difficult part of this problem is the global optimization problem, since the parameters to be identified are highly correlated and the objective function is highly nonlinear and non-convex. The numerical details for solving such problem will be discussed in chapter 3

After the model identification step, the usefulness of the models is illustrated by studying the phenomenon of spatial pattern formation. It has been proved that even the simplest membrane reactor model with the simplest reaction kinetics could show complex spatiotemporal patterns, including standing or moving waves and aperiodic patterns [14, 15]. Even chaotic solution is found if two consecutive reactions are carried out in a membrane reactor [16]. The patterns may be induced by several different reasons:

1. The generation of Turing wave when the inhibitor diffuses sufficiently faster than the activator.

2. The pattern induced by the interaction of kinetics and convection.

3. The pattern emerge due to the interaction of enthalpy and mass balances.

The last term is also a common reason to cause nonlinear behavior in traditional CSTR reactors and has been studied thoroughly by Uppal [17, 18]. The similarity between the CSTR and membrane reactor will be explained in chapter 5. The periodic and aperiodic pattern formation has been investigated in the same chapter by using both a simple and a detailed membrane reactor model.

Chapter 2

Models for fixed bed membrane reactors with porous membrane

2.1 Definition of a parametric model

In daily language, *model* is an ambiguous word with many different meanings. But in this book, a model refers specifically to a *mathematical model*, which is an abstract model that uses mathematical language to describe a system. Furthermore, the model discussed in this work is *deterministic* and composed by a group of algebraic and/or differential equations. A deterministic model may compute an output vector y from an input vector u, see Figure 2.1. This model scheme is said to be *parallel* because the model and real system have the same input [19].

A model may be used e.g. for:

- Process simulation and process optimization
- Nonlinear behavior analysis

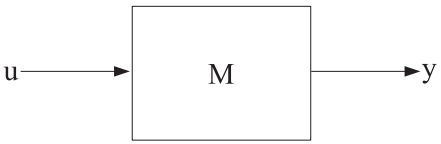

Figure 2.1: A *parallel* model structure

- Estimation of states and parameters for which no direct observation is available
- Model predictive control

In all, establishing a mathematical model is a practical way for better understanding or controlling a real process. The process of establishing a model is composed of two steps:

1. Selection of a suitable model structure, also called *characterization*.
2. Identification of the parameters for the given model structure.

For any unknown process, the model structure selection is the critical step in modeling. And the two modeling steps may have to be repeated many times for each model structure candidate. For some other chemical or physical process, where the model structure could be determined by prior knowledge or *first principle*, the task of model identification is simplified to the choice of parameters. Usually the parameters are chosen by optimization of some cost function, which is discussed in detail in section 3.1.1.

2.2 Models for fixed bed membrane reactors with porous membrane

2.2.1 Model structure

A model of a fixed bed membrane reactor is composed of three parts:

1. A model of the catalytic fixed bed inside a porous membrane
2. A model of heat and mass transport through the membrane
3. A model of the sweep gas side outside the membrane

The scheme of such a membrane reactor model is illustrated in figure 2.2. Considering different boundary conditions, the inlets and outlets of the reactor could be modeled separately as described in figure 5.12.

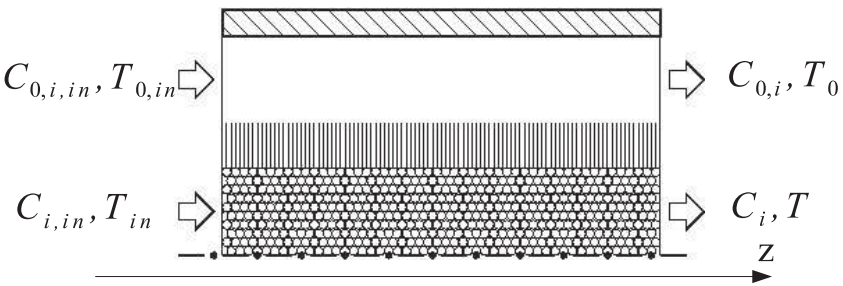

Figure 2.2: Scheme of fixed bed membrane reactor model

2.2.2 Model for the fixed bed

In this work, a pseudo-homogeneous fixed bed reactor model is considered. The model is the same as that of a normal tubular reactor except for an additional term of mass transfer through the membrane. Under the assumption of constant pressure and plug flow inside the reactor, the component mass balances in fixed bed side as shown in figure 2.3 is:

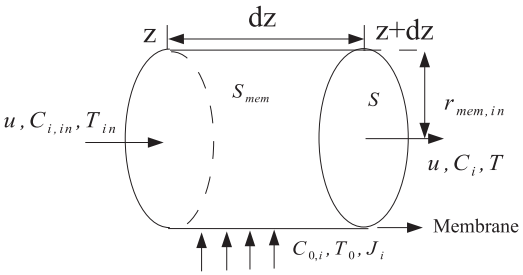

Figure 2.3: Fixed bed side of the membrane reactor

$$\frac{\partial(c_i dV)}{\partial t} = (\dot{N}_i)_z - (\dot{N}_i)_{z+dz} + (\dot{N}_i)_{mem} + \mathcal{R}_i dV \tag{2.1}$$

Radial concentration and temperature gradients as well as the change of the axial flow rate due to mass transport through the membrane are neglected. We expand the flux terms by flow velocity, cross-section area, flux density through membrane and reaction kinetics to obtain:

$$\frac{\partial(Sdzc_i)}{\partial t} = Suc_{i,z} - Suc_{i,z+dz} + S_{mem}J_i + \sum_{j=1}^{n} \nu_{ij} r_j \rho_{cat} Sdz \tag{2.2}$$

Suppose that $dz \to 0$, we have:

$$Suc_{i,z+dz} = Suc_{i,z} + Sudz\frac{\partial c_i}{\partial z}|_{z,t} \tag{2.3}$$

By replacing the second term of the right-hand side of equation 2.2 with equation 2.3, we obtain:

$$\frac{\partial(Sdzc_i)}{\partial t} = -Sudz\frac{\partial c_i}{\partial z}|_{z,t} + S_{mem}J_i + \sum_{j=1}^{n}\nu_{ij}r_j\rho_{cat}Sdz \tag{2.4}$$

The cross-section area for plug flow and membrane is $S = \pi r_{mem,in}^2$ and $S_{mem} = 2\pi r_{mem,in}dz$, therefore:

$$\frac{\partial(\pi r_{mem,in}^2 dzc_i)}{\partial t} = -\pi r_{mem,in}^2 udz\frac{\partial c_i}{\partial z}|_{z,t} + 2\pi r_{mem,in}dzJ_i + \sum_{j=1}^{n}\nu_{ij}r_j\rho_{cat}\pi r_{mem,in}^2 dz \tag{2.5}$$

Finally, we devide all the terms in above equation by $\pi r_{mem,in}^2 dz$ and the mass balance becomes:

$$\frac{\partial c_i}{\partial t} = -u\frac{\partial c_i}{\partial z} + \sum_{j=1}^{n}\nu_{ij}r_j\rho_{cat} + \frac{2}{r_{mem,in}}J_i, \quad i = 1,\ldots,n \tag{2.6}$$

The energy balance can be deduced in a similar way. Since the heat transfer model of membrane is simply $\dot{q} = \alpha_{mem}(T_0 - T)$ and can be incorperated into the energy balance equation of fixed bed, the final form of the energy balance equation is:

$$(\rho c_P)_{tot}\frac{\partial T}{\partial t} = -u\,(\rho c_P)_f\frac{\partial T}{\partial z} + \lambda_{fl}\frac{\partial^2 T}{\partial z^2} + \sum_{j=1}^{5}\nu_{ij}\,(-\Delta_R H)_j\,r_j\rho_{cat} + \frac{2}{r_{mem,in}}\alpha_{mem}\,(T_0 - T) \tag{2.7}$$

In the model, the heat of reaction varies with temperature; the partial molar enthalpy of

each component is computed by:

$$h_i = h_{i,ref} + c_{Pi} \times (T - T_{ref}) \tag{2.8}$$

The boundary conditions for equations 2.6 and 2.7 are:

$$z = 0 : c_i = c_{i,in},\ i = 1, \ldots, n, \lambda \frac{\partial T}{\partial z} = u \left(\rho c_P\right)_f (T - T_{in}) \tag{2.9}$$

$$z = L : \frac{\partial T}{\partial z} = 0 \tag{2.10}$$

2.2.3 Model for sweep-gas side

The model of sweep gas side is similar to that of the fixed bed side except for that the chemical reaction is ignored. Note that the cross-section area becomes $\pi(r_{wall}^2 - r_{mem,out}^2)$, see figure 2.4, and the mass balance is:

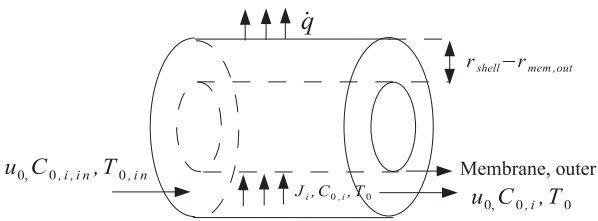

Figure 2.4: Sweep gas side of the membrane reactor

$$\frac{\partial c_{0,i}}{\partial t} = -u_0 \frac{\partial c_{0,i}}{\partial z} - \frac{2 r_{mem,out}}{r_{wall}^2 - r_{mem,out}^2} J_i, \quad i = 1, \ldots, n \tag{2.11}$$

The energy balance should also consider the heat transfer through the outer reactor wall, so the total energy balance equation is:

$$(\rho c_P)_{tot}\frac{\partial T_0}{\partial t} = -u_0\,(\rho c_P)_f\frac{\partial T_0}{\partial z} + \lambda_{sw}\frac{\partial^2 T_0}{\partial z^2} + \frac{2r_{mem,out}}{r_{wall}^2 - r_{mem,out}^2}\alpha_{mem}\,(T - T_0) + \frac{2r_{wall}}{r_{wall}^2 - r_{mem,out}^2}\alpha_{wall}\,(T_{wall} - T_0) \quad (2.12)$$

Similar boundary conditions as for the fixed bed side are applied.

2.2.4 Mass transfer model for the membrane

The model of mass transport through the membrane is an important part in the modeling of membrane reactor, because this mass transport distinguishes a membrane reactor from a traditional plug flow reactor. During the last decades, a complete theory of gas transport through porous media has been established, which is known as the *dusty-gas model* (DGM) [20]. The DGM theory assumes that gas transport through porous media is determined by three *independent* mechanisms as follow:

- Free-molecule or Knudsen flow, which is driven by the collisions of molecules with the walls of the porous medium.
- Viscous flow, also called convective or bulk flow, which is driven by the pressure gradient, or molecule-molecule collisions.
- Continuum diffusion, also called molecular diffusion, where different species of a mixture move relative to each other.

Considering all the above mechanisms, the gas transport phenomenon could be described by the following full equation:

$$-\frac{P}{RT}\nabla x_i - \frac{x_i}{RT}(1+\frac{B_0}{D_{K,i}\eta}p)\nabla P = \sum_{j=1,j\neq i}^{n}\frac{x_jJ_i - x_iJ_j}{D_{ij}^e} + \frac{J_i}{D_{K,i}} \tag{2.13}$$

where:

$$D_{K,i} = \frac{4}{3}K_0\sqrt{\frac{8RT}{\pi M_i}} \tag{2.14}$$

$$D_{ij}^e = F_0 D_{ij} \tag{2.15}$$

where D_{ij} is the gas diffusion coefficient which only depends on the composition of the gas phase and independent of the material of the membrane. In this work D_{ij} is calculated by Fuller's equation [21]:

$$D_{AB} = \frac{0.00143T_1.75}{PM_{AB}^{1/2}[(\Sigma_v)_A^{1/3} + (\Sigma_v)_B^{1/3}]} \tag{2.16}$$

Therefore, the influence of the porous media to the gas transport could be characterized by the three parameters: B_0, K_0 and F_0. Under some additional assumptions [20], the three parameters could be related to the structural parameters by the following equations:

$$B_0 = \frac{\varepsilon}{\tau}\frac{d_P^2}{32} \tag{2.17}$$

$$K_0 = \frac{\varepsilon}{\tau}\frac{d_P}{4} \tag{2.18}$$

$$F_0 = \frac{\varepsilon}{\tau} \tag{2.19}$$

where d_P is the diameter of assumed capillaries, and $\frac{\varepsilon}{\tau}$ is porosity divided by tortuosity of the membrane. Thus, the membrane could be described by any two of the above parameters. However, it should be stressed d_P and $\frac{\varepsilon}{\tau}$ are *not* really structural parameters, and could not

be derived by direct observation of the physical micro-structure of the membrane. These parameters can only be identified from experimental data of gas transport.

For a thin cylindrical homogeneous membrane, the equation 2.13 can be approximated to:

$$-\frac{2\pi L}{RT\ln\left(\frac{r_{mo}}{r_{mi}}\right)}[-\bar{P}\Delta x_i-(1+\frac{B_0}{D_{K,i}\eta}\bar{P})\bar{x}_i\Delta P]= \sum_{j=1,j\neq i}^{n}\frac{\bar{x}_j\dot{N}_i-\bar{x}_i\dot{N}_j}{D^e_{ij}}+\frac{\dot{N}_i}{D_{K,i}} \tag{2.20}$$

Note that here Δ stands for the differences between the two sides of membrane, $\bar{x}_i$ and $\bar{P}$ denote the average values inside the membrane, and $\dot{N}_i = 2\pi L r J_i$ is the total mass flux through the membrane. For a multi-layer membrane, the DGM equations should be applied to each layer, and the equation can be rewritten as:

$$-\frac{2\pi L}{RT\ln\left(\frac{r_{m,k+1}}{r_{m,k}}\right)}[-\bar{P}_k\Delta x_{i,k}-(1+\frac{B_{0,k}}{D_{K,i,k}\eta}\bar{P}_k)\bar{x}_{i,k}\Delta P_k]= \sum_{j=1,j\neq i}^{n}\frac{\bar{x}_{j,k}\dot{N}_{i,k}-\bar{x}_{i,k}\dot{N}_{j,k}}{D^e_{ij}}+\frac{\dot{N}_{i,k}}{D_{K,i,k}} \tag{2.21}$$

where:

$$\Delta P_k = P_{in,k} - P_{in,k+1} \tag{2.22}$$

$$\sum_{k=1}^{n} \Delta P_k = P_A - P_B \tag{2.23}$$

$$\overline{P_k} = \frac{P_{in,k} + P_{in,k+1}}{2} \tag{2.24}$$

$$\Delta x_{i,k} = x_{in,i,k} - x_{in,i,k+1} \tag{2.25}$$

$$\sum_{k=1}^{n} \Delta x_{i,k} = x_{i,A} - x_{i,B} \tag{2.26}$$

$$\overline{x_{i,k}} = \frac{x_{in,i,k} + x_{in,i,k+1}}{2} \tag{2.27}$$

for k=1,2,. . . ,n and:

$$P_{in,1} = P_A \tag{2.28}$$

$$P_{in,n+1} = P_B \tag{2.29}$$

$$x_{in,i,1} = x_{i,A} \tag{2.30}$$

$$x_{in,i,n+1} = x_{i,B} \tag{2.31}$$

Here $P_{in,k}$ and $x_{in,i,k}$ are the pressure and molar fraction between the membrane layers, P_A P_B $x_{i,A}$ $x_{i,B}$ are pressure and molar fraction on both sides of the membrane, Δ stands for the differences between membrane layers, $\bar{x}_{i,k}$ and $\bar{P}_k$ denote the average values inside the membrane layer, and $\dot{N}_i = 2\pi L r J_i$ is the total mass flux through the membrane.

2.3 Parameters to be identified in experiments

Most of the parameters of the membrane reactor are already known or can be found in literatures, such as the geometry of the membrane reactor, the properties of the gases, but still some parameters must be identified from experiments. The two main groups of parameters to be identified are:

1. The parameters describing the reaction kinetics. In this work the oxidative dehydrogenation of ethane catalyzed by $VO_x/\gamma - Al_2O_3$ is considered.

2. The parameters describing the mass transfer through the membrane. In DGM model the K_0 and B_0 for each layer of the membrane should be identified.

The parameters describing the reaction kinetics can be viewed as a property of the catalyst, while the parameters describing the mass transfer represent the property of the membrane, however both of the two groups of parameters can not be calculated directly from the microscopical structure or the chemical composition of the material but have to be fitted through corresponding experimental data. The numerical methods for parameter fitting and experimental design are discussed in chapter 3 and the application to identify mass transport parameters is presented in chapter 4. The parameter identification of reaction kinetics is already finished by Klose [22] and Joshi [23].

Chapter 3

Methods for model identification and experimental design

3.1 Introduction

3.1.1 Parameter identification problem

Usually only a part of the model states is measurable which is called *observation*. The parameter identification problem is to choose values of set of parameters which minimize the difference of model prediction and real observation, see Figure 3.1.

The most commonly used criteria for parameter identification are called *quadratic cost functions*. To minimize the quadratic error between measurements and model outputs, the cost function below can be applied:

$$J = \sum_{k} \sum_{i} w_{ik} (y_{k,t_{ik}} - y_{mk,t_{ik}})^2, \tag{3.1}$$

where $y_{k,t_{ik}}$ is the k-th measurement value taken at time t_{ik}, $y_{mk,t_{ik}}$ is the corresponding

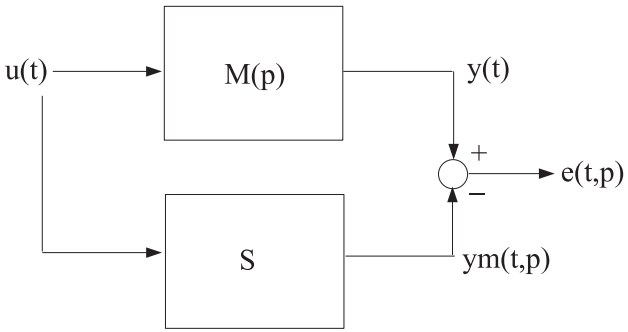

Figure 3.1: Identification of parametric model

simulated measurement value, and w_{ik} is a weighting factor. The statistical theoretical background of this identification criterion is discussed in Appendix A.1.

3.1.2 Estimation of confidence intervals

The parameter identification method described in section 3.1.1 is a *point estimate*, because it returns a single value for each parameter, but provides no information about how precise and how reliable the values are. In a realistic problem, the estimate of the parameter variance, which is called *confidence interval* may be a key point in the whole process of parameter identification and experimental design, see section 3.1.4. There are several different ways for estimation of confidence interval, the most common methods are:

- Cramér-Rao inequality, which gives a lower bound for the estimated variances (The

provement is given in [24]. It states that for an unbiased parameter estimator the variance σ_j^2 of a certain estimated parameter is at least as large as the corresponding element on the main diagonal of the inverse Fisher information matrix (FIM): $\sigma_j^2 \geq (\text{FIM}^{-1})_{jj}$.

- The bootstrap method [25]: first use a Monte-Carlo simulation to generate a large set of replicated *experimental data*, and then identify the parameters from each replication.

- The sigma point method [26, 27, 28]: a similar approach as bootstrap, but use far less *experiments* (usually totally $2D_y + 1$ points)

The calculated confidence interval (by bootstrap or sigma point method) could be used directly for experimental design and usually provide better performance than the traditional FIM method. However, for any big enough model or global optimization problem, the computation time is formidable.

3.1.3 Optimal experimental design

In order to get maximal information from a limited number of experiments or in a limited amount of time, usually some kind of optimal experimental design (OED) should be performed [29, 30]. The application of OED to linear steady state experiments has been developed for a long time [31], and recently there are also some papers on application of OED to nonlinear and dynamic processes [32]. The classical way of experimental design is to choose some input signal $\boldsymbol{u}(t)$ to minimize some criterion of the Fisher information matrix, which is in turn based on parameter sensitivities of an output $\boldsymbol{y}$ with respect to parameter $\boldsymbol{p}$, see figure 3.2

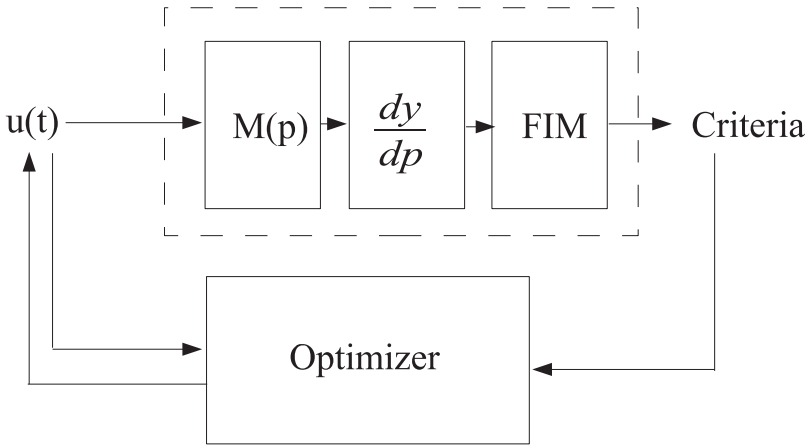

Figure 3.2: Scheme of experimental design

For a system with time discrete measurements at times $t_i, i = 1, \ldots, N$ and additive normal distributed measurement noise, the Fisher information matrix reads

$$\text{FIM} = \sum_{i=1}^{N} (\frac{\partial \boldsymbol{y}}{\partial \boldsymbol{p}})_i^T \boldsymbol{Q}^{-1} (\frac{\partial \boldsymbol{y}}{\partial \boldsymbol{p}})_i, \tag{3.2}$$

where $\boldsymbol{y}$ is the measurement vector, $\boldsymbol{p}$ is the parameter vector and $\boldsymbol{Q}$ is the covariance matrix of the measurement noise [29].

The inverse of the Fisher information matrix gives a lower bound for the estimated covariances of the parameters, which is called the Cramér-Rao bound [29].

$$\sigma_j^2 \geq (\text{FIM}^{-1})_{jj} \tag{3.3}$$

Figure 3.3 gives a geometric illustration of Cramér-Rao bound, where the shaded area represents the confidence region of the estimated parameters.

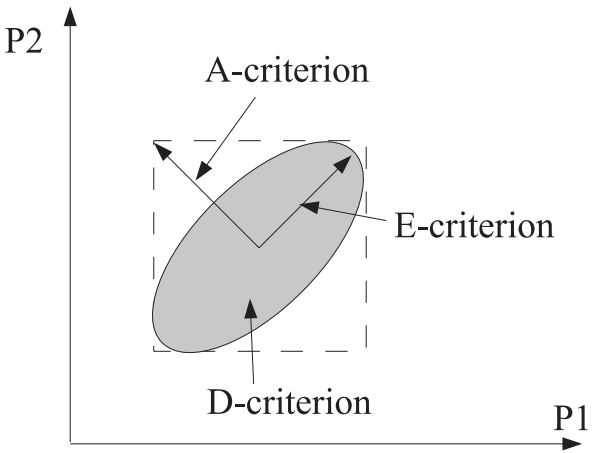

Figure 3.3: A geometric illustration of the Cramér-Rao bound and various OED criteria

The classical OED minimizes a scalar function of the FIM by changing some control parameters. Commonly used optimization criteria are listed below, and illustrated in figure 3.3.

1. D-Criterion $\rightarrow \arg\max(\det \text{FIM})$: minimize the volume of the joint confidence region.

2. E-Criterion $\rightarrow \arg\max(\lambda_{min}(\text{FIM}))$: minimize the size of the major axis of the joint confidence region.

3. A-Criterion $\rightarrow \arg\min \text{trace}(\text{FIM}^{-1})$: minimize the dimensions of the enclosing box around the joint confidence region.

4. ME-Criterion $\rightarrow \arg\min \frac{(\lambda_{max}(\text{FIM}))}{(\lambda_{min}(\text{FIM}))}$:minimize the proportion of the largest eigenvalue to the smallest eigenvalue of FIM, thus improve the shape of joint confidence region.

Where λ_{min} and λ_{max} are the smallest and biggest eigenvalue of FIM, respectively.
Although all of these criteria have been tested in the study, only the design results of e-criterion will be discussed, since in most cases the e-criterion provided the best performance results. The calculation of the Fisher information matrix requires information on the sensitivity. There are several different ways to calculate the sensitivity, in this work we use the "direct method" which means to incorporate equations of sensitivity into the original model, see the dashed box in figure 3.2. The details of this method are described in appendix A.3.

3.1.4 Standard algorithm for model identification

The full process of parameter identification and experimental design is shown in figure 3.4. In the first step, some preliminary experiments are performed. The conditions of experiments could be chosen by experience or simple experimental design such as *block experiment* or *factorial experiment* [33]. In the second step a model structure is designed either by prior knowledge or guess from the experimental data. Then, the parameters and

confidence intervals could be estimated from the data. Usually the confidence interval is very big in the first identification process, so either a new model structure should be tested or some new experiments should be designed in order to increase the precision of the parameters. This process is repeated until certain precision criterion is reached.

3.1.5 Global optimization problem

Both parameter identification problem and experimental design problem need to minimize some kind of cost function, therefore are both optimization problems. Most of the common optimizer are gradient based and can only locate a *local minimum*. They are so called *local deterministic optimizer* (LDM). A LDM can only be applied when the model is *convex*, or the initial guess of the parameters is close enough to the real values. In reality, however, the problem is usually highly non-convex and no prior knowledge of the parameters could be obtained. In this case a *global optimizer* should be used instead.

In this paper, we use a hybrid optimizer for optimal experimental design. The hybrid optimizer is a combination of a genetic optimizer by K. Teplinskiy [34, 35] and a local deterministic optimizer by C. Zhu [36]. Both optimizers are incorporated in the DIANA simulation environment [37]. The classical genetic algorithm is modified to increase efficiency. The details of the algorithm will be described in the next sections.

3.2 The traditional Genetic Algorithm

3.2.1 Genetic algorithm and global optimization

The simplest method of global optimization is to perform a thorough grid search, which needs to evaluate the objective function at each grid point of the entire feasible parameter region. The minimum value found in this way is guaranteed to be the global optimum at

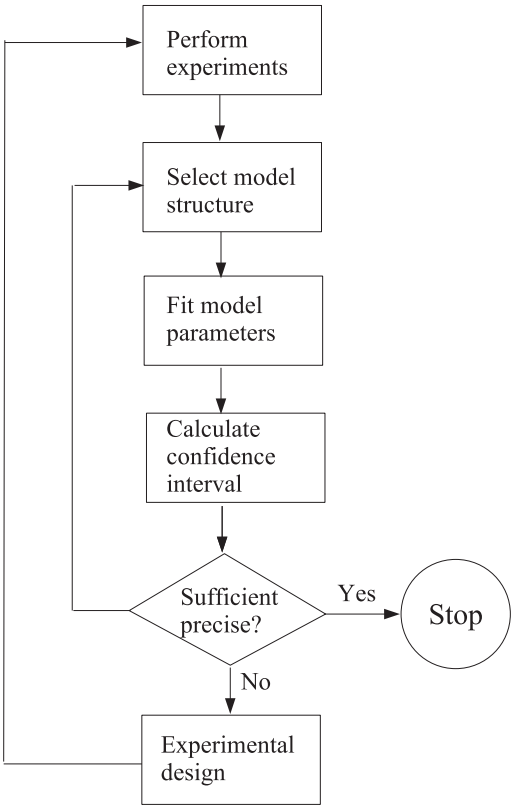

Figure 3.4: Standard algorithm for model identification

certain precision. And this is also (up to now) the only way to guarantee to find the global optimum of a non-convex objective function. However, in such a way the computation time grows exponentially with the increase of number of parameters to be optimized, which

means for most of the practical problems it's impossible for such technique to be applied.

To increase the search efficiency, most of the practical global optimizer perform a heuristic search or a random search, or a combination of both. The most popular optimizer using such technique include simulation annealing and evolutionary algorithms. The genetic algorithm, which is applied through this work, is one of the most recognized forms of evolutionary algorithms. However, it should be noted that heuristic search techniques also increase the risk for the optimiation result to be trapped in wrong local minima, since the heuristic approach may be misguided by some *cheating information* from the objective function. And the random search of course, unavoidably brings some uncertainties into the optimization results which makes it difficult to evaluate the performance of an optimizer.

In theoretical research, the global optimization problem has proved to be a NP-complete problem [38]. According to the theorem presented by Hart and Belew [39], there exists no algorithm which is able to approach the global optimum of arbitrary functions to a certain accuracy in a polynomial time. Therefore, one cannot just focus on parameter identification or experimental design tasks and treat the optimizer simply as a *black box*. The optimizer should also be studied and *optimized* to be adapted to special practical problems.

Except for the noise of observation, the randomness of the genetic optimizer introduces another uncertainty to the parameters. Therefore, when calculating the confidence interval the variance caused by the genetic optimizer should also be considered as an additional source of *noise*. Since GA is a heuristic algorithm, the optimization precision increases proportionally to the number of function evaluations. It's sometimes a difficult choice to compromise between optimization time and precision. The solutions for different problems are discussed in the according sections.

3.2.2 Genetic algorithm

The genetic algorithm (GA) was first suggested by John Holland in 1975 [40]. GA works as an imitation of a biological system - by "selection of the fittest", the "good genes" are preserved and reproduced, and therefore more competitive offspring will be generated.
The basic idea of GA is to use chromosomes, which in fact is a long line of bit strings composed of 0 and 1, to represent the parameters to be optimized. The chromosomes can be recombined in a crossover way to simulate the sexual reproduction of organisms, and can also mutate to simulate the mutation of organism by simple bit flips. Afterwards, the "offspring" are compared and selected according to the relative "fitness" value, which is usually a scaling scalar function of the objective value. With a small enough mutation rate, after several generations the chromosomes in the population will tend to be homogeneous and thus usually a "good enough" global optimization result is found.
The classical GA is composed of the following steps:

1. Representation and Initialization

   In this step, the parameters to be optimized are translated to a long line of bit-string. The bit-string represents a *Chromosome*, and each bit of it represents a *gene*. The length of the bit-string is decided by the Upper, Lower-boundary and precision of the parameter to be optimized: $L = \log_2 \frac{Upper-Lower}{precison}$. The parameter can be first converted to a positive integer as $\frac{P-Lower}{precision}$, and then converted from decimal numeral expression to a binary numeral expression. Although there are different kinds of encoding system, the simplest way is a direct conversion such as: $1 \rightarrow 00001, 31 \rightarrow 11111$. In the evaluation step the bit-string can be converted back to recover the parameter value, based on the same rule.

   During the initialization process, a group of chromosomes are initialized randomly. The group of chromosomes is called a *population*. The number of chromosomes in

the group is called the size of the population. In the next steps, the chromosomes in population are recombined and mutated to form new chromosomes, and after selection to form a new population. The process of going from one population to the next population is called a *generation*. Usually the number of chromosomes in population will keep constant during generation, which means the number of chromosomes eliminated is the same as the number of newly created chromosomes.

2. Crossover

   The crossover operator is the most distinguished feature of GA. The most common form of crossover is one-point crossover, which means to recombine two chromosomes at a single randomly chosen crossover point, as described below.

   $$\begin{array}{l|l} 0000 & 00 \\ 1111 & 11 \end{array} \rightarrow \begin{array}{l|l} 0000 & 11 \\ 1111 & 00 \end{array}$$

   Since each bit represents a *gene*, such kind of operation is assumed to be able to combine the *good gene* and form some offspring with higher fitness.

3. Mutation

   Although the crossover operator can recombine and preserve good gene, it cannot create new gene which is not initialized in the original population. Therefore the *mutation* operator is introduced to increase the possibility of finding the global optimum which is not covered by the initial population of chromosomes. The mutation operator randomly flips a bit of the chromosome with a constant probability P_m, as follows:

parent	000**0**00
child	000**1**00

   Typically the probability of mutation should be less than 1%, otherwise it would be difficult for the GA optimizer to converge.

4. Evaluation and selection

   In this step, the parameter values are restored from the bit-string expression and the corresponding objective function is calculated. The objective value is used to calculate the *fitness* of the chromosomes. Then the chromosomes are selected according to their fitness. The chromosomes with higher fitness value will have higher *selection probability* (or *survival probability*). The selection mechanism developed by Holland is called the *proportional selection method* as it defines the survival probability proportional to the relative fitness of the chromosomes.

5. Termination

   There are many possible stopping criteria for GA, such as the homogeneity of the population, the given maximal generation or maximal number of function evaluation reached, or the given percentage of schemata completed. The GA will stop when it meets any of the above stop criteria and return the best objective value of the population.

The original GA optimizer in this work is developed by Teplinskiy [34, 35], in a ProMot/Diana simulation environment [37]. The program and modifications in the following sections are all written in GNU C++/python interface. The total process of GA is illustrated in figure 3.5.

3.2.3 Schemata theory

Schemata and hyperplane

A *schema* is a string composed of 0, 1 and *, where * is a wildcard to represent both 0 and 1. For any population of chromosomes, a schema can be easily constructed by replacing the different bits with *, as described in tabular 3.1.

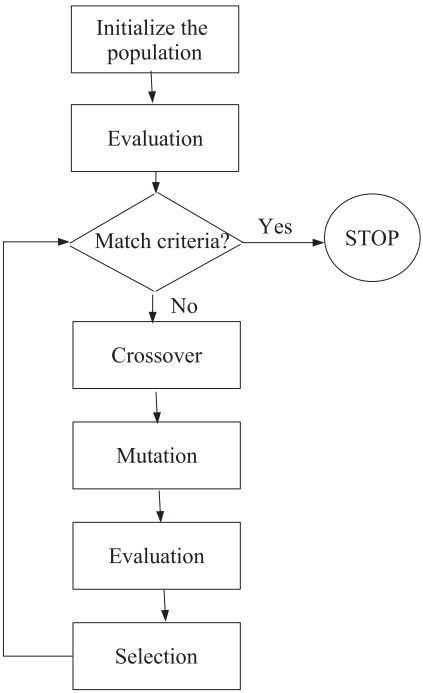

Figure 3.5: Outline of a Genetic Algorithm

Therefore, a schema can represent a group of possible bit-strings. For example, schema like 1****** represents all the bit-strings that begin with 1 and thus defines a sub-set which contains half of the possible chromosomes. The sub-set is also called a *hyperplane* of the

Table 3.1: Definition of a schema

000000 **0**11111	→	**0*******
1**0**000**1** 0**0**111**1**	→	***0*******1**

search space, and the number of 0 or 1 in the string of schema is called the *order* of the hyperplane. The situation of 1-dimensional hyperplane is illustrated in figure 3.6.

Holland suggests that the chromosomes in the population format different order of schemata, and the schemata represent different levels of hyperplane. The lower the order of the schema, the more chromosomes will sample it. Therefore the evolution of the population is not only competition between chromosomes and chromosomes but also competition between schema and schema, or hyperplane and hyperplane. The schema with low order and high average fitness will tend to survive and produce more offspring, and thus makes the GA optimization a heuristic search process. Furthermore, Holland estimates that for a population composed of n chromosomes, there are $O(n^3)$ schemata processed in each generation. So the GA is also called an *implicit parallel process*, and expected to be more efficient than other evolutionary algorithms.

Schema theorem

Holland deduced an equation to describe the growth rate of a schema/hyperplane:

$$E[m(H,t+1)] \geq m(H,t)\frac{f(H,t)}{\bar{f}(t)}[1-P_c\frac{\Delta(H)}{L-1}(1-m(H,t)\frac{f(H,t)}{\bar{f}(t)}\times(1-P_m)^{O(H)} \quad (3.4)$$

where

- H is the given schema/hyperplane.

- $m(H,t)$ is the proportion of the population that is within hyperplane H at generation t.
- $f(H)$ is the mean fitness of the chromosomes in H.
- $\bar{f}(t)$ is the mean fitness of the whole population at generation t.
- $O(H)$ is the order of the schema.
- $\Delta(H)$ is the definition length of the schema.
- P_c is the crossover probability.
- P_m is the mutation probability.

Unfortunately, the equation can only predict the lower boundary of the relative frequency of a schema for one step, and cannot provide any information about the growth rate of the schema in the future steps or how to choose the mutation rate or crossover rate to increase the converging rate to the global optimum.
The equation can only be explained qualitatively, that a schema with short definition length and high fitness, which is also called a *building block* will grow very fast, as we have already mentioned before. There's also an argument that the building blocks will receive exponentially increasing trails in future generations. But such argument is very dubious since the equation 3.4 in fact only gives a prediction for one step, both the fitness of H and the average fitness could change rapidly during optimization process.

Criticism of schema theorem

In practical study, however, many deficiencies of the schema theory have been raised [41]. Some of them are listed as below:

1. The schemata may be not sampled

   The possible number of schemata is far more than the number of bit strings, therefore schemata with high order have very few samples. A big population size is important to prevent GA from missing important schemata, but there's not general guideline about how to choose the population size.

2. The schemata may be inconsistent

   For schemata as ***11* and ****00 can both have above average fitness, but are conflicting in the fixed bits. Apparently they can both increase fast after some time, and they cannot be recombined to form a better chromosome.

3. The schemata could be cheating

   Occasionally the global optimum is not located in the hyperplane with high average fitness, see figure 3.7. In such case no efficient way could be found to reach the global optimum, but GA may have worse performance than a pure random search strategy since the heuristic search process is misguided.

4. Schemata could be easily destroyed

   Schemata could be easily destroyed when the mutation rate or crossover rate are too high as described in equation 3.4, therefore the mutation rate is usually limited below 0.01.

Besides all of the above already known problems with schema theory and GA optimization, in this research, linear correlation of the parameters is found to be another factor to cause problem for GA optimization tasks. The main purpose of the next sections of this chapter, is to study the impact of linear correlation of parameters to the GA, and present a possible solution to such problems. The newly developed method was applied to solve the optimization problems in chapter 4 and proved successful.

3.3 Genetic algorithm with linear correlation in parameters

To study the GA with linearly correlated parameters, we need to look into some optimization problems with at least two parameters. Consider four benchmark problems as follow:

$$z = x + y \tag{3.5}$$

$$z = (x-5)^2 + (y-5)^2 \tag{3.6}$$

$$z = 10000((x-7)^2) + (y-5)^2 \tag{3.7}$$

$$z = 10000(((x-y)-2)^2) + (x+y-12)^2 \tag{3.8}$$

For an intuitive view, the surface plot of the objective function are plotted in figure 3.8.
The above four functions are tested for optimization with GA. The boundary is set to $x \in [0\ 10]$ and $y \in [0\ 10]$, while the precision is set to 0.1. The genetic optimization is performed with initial population size=100. In most cases, the optimization and the precision of function 1,2 or 3 will converge in about 20 generations. But for function 4, the GA optimizer normally runs over 50 generations and still can't find a good enough solution, see figure 3.9. After 10 generations the population converge to the valley of optima, but such a *pattern* is not sustainable. The pattern is destroyed and reformed repeatedly, and the convergence rate is very slowly. After 50 generations, the best solution found has only objective at the order of 10^1.
To explain the results, firstly consider the possible schemata of the optimization problems in figure 3.10. The objective surface of function 4 cannot be described with a order 1 schema, although there is obvious pattern of the optima of objective. Of-course the schema theorem cannot be applied here since there's not even a schema that can be defined. Consider the

first two bit of the schemata of function four (the other part is abbreviated for simplicity). Now we have four conflicting schemata:

$$\begin{pmatrix} 0 & 0 & * & ... & 0 & 0 & * & ... \\ 0 & 1 & * & ... & 0 & 1 & * & ... \\ 1 & 0 & * & ... & 1 & 0 & * & ... \\ 1 & 1 & * & ... & 1 & 1 & * & ... \end{pmatrix}$$

For any 3 of the schemata no low order schemata exist, but for some pair of schemata it's possible to summerize some low-order schemata:

$$\begin{pmatrix} 0 & * & * & ... & 0 & * & * & ... \\ 1 & * & * & ... & 1 & * & * & ... \\ * & 0 & * & ... & * & 0 & * & ... \\ * & 1 & * & ... & * & 1 & * & ... \end{pmatrix}$$

It looks like GA could combine such low order schemata to form the above high order schemata. For example to combine 0*...0*... and *0...*0... to 00...00... However, for the one point crossover operator, 0*...0*... and *0...*0... must first form schemata like 00...0*..., 00...*0..., 0*...00... or *0...00..., and these schemata have no higher fitness comparing to 0*...0*... and *0...*0..., therefore the formation of such schemata has quite low probability.

Secondly, consider the operator of GA. See figure 3.11, the solid line represents the valley of the objective function where the optima exist. Chromosome 1 and chromosome 2 are two possible chromosomes in the population, the arrows indicate the direction of possible offspring for one step crossover or mutation. The production of new chromosomes almost always move in the direction parallel to the axis instead of along the valley. The new

offspring outside the valley is easily eliminated in the selection step because of the low fitness and thus has little chance in ”jumping back” to the valley, therefore the evolution process becomes quite inefficient. There are still small possibilities for the GA optimizer to find the global optimum by luck, for example by combination of crossover and mutation or by multi-mutation the chromosomes could happen to locate on the valley, and there are also small possibilities for some chromosomes outside the valley to survive and generate the their offspring which could also happen to arrive the valley (especially for a not very sharp valley). However, apparently these processes are quite inefficient and show more stochastic character. The better way should be, like the other gradient based optimizer, to let the optimizer recognize the valley of optima and move along the valley to reach the optimum.
One can immediately think of two possible solutions to this problem:

1. To define some new crossover and mutation operator considering the correlation of the chromosomes in the population.

2. To make a coordinate transformation to automatically de-correlate the parameters.

In this work only the second method is tested because it’s intuitively straightforward and still stay in the basic theory framework of GA. In the following part, this new genetic algorithm is denoted as GACT (Genetic Algorithm with Coordinate Transformation).

3.4 GACT for 2-dimensional optimization problem

For a two parameter optimization, the GACT works in the following way:

1. After several generations when the pattern of population is expected to be established, the correlation coefficient of the two parameters of the current population is

calculated and compared with a limit value. If the absolute value of the correlation coefficient is less than a limit value, continue to the next generation.

2. If the correlation coefficient exceeds the limit: $|Corr(P1, P2)| > corrlim$, the valley of the optima is assumed to have the form $P2 = a \times P1 + b$, a linear regression is applied to calculate the parameter a and b.

3. When the slope of the line a is known, a rotation matrix could be formulated by choosing the first column vector parallel to the fitted line and the second one orthogonal to it:

$$M_{rot} = \begin{pmatrix} \frac{1}{\sqrt{a^2+1}} & \frac{-a}{\sqrt{a^2+1}} \\ \frac{a}{\sqrt{a^2+1}} & \frac{1}{\sqrt{a^2+1}} \end{pmatrix}$$

This matrix represents the transformation from the new coordinate back to current coordinate. To transform from current coordinate system to the new coordinate system the following equation is applied:

$$\begin{pmatrix} x'_1 & x'_2 & x'_3 & \dots & x'_n \\ y'_1 & y'_2 & y'_3 & \dots & y'_n \end{pmatrix} = M_{rot}^{-1} \times \begin{pmatrix} x_1 & x_2 & x_3 & \dots & x_n \\ y_1 & y_3 & y_3 & \dots & y_n \end{pmatrix}$$

4. A new boundary is set for the new representation of each parameter and the optimization task is redefined. In this section we simply set the new boundary as $x \in [min(x')\ max(x')]$ and $y \in [min(y')\ max(y')]$

5. Update the total rotation matrix to restore the original parameter values. Since the coordinate transformation could be performed several times, a total rotation matrix should be recorded in order to retrieve the original parameter later, thus:

$$M_{tol} = M_{tol} \times M_{rot} \tag{3.9}$$

In the first step, M_{tol} is set to be an identity matrix.

6. The GA is applied to the new defined optimization problem, then return to step 1.

The algorithm is first tested with the simple optimization problem as described in equation 3.8. All the settings of GA and optimization task are the same as before. The limit of correlation coefficient is set to 0.8. In generation 11, the calculated correlation coefficient matrix becomes:

$$M_{cor} = \begin{pmatrix} 1.0 & 0.81 \\ 0.81 & 1.0 \end{pmatrix}$$

The correlation of two parameters of the population exceeds the limit, so a linear regression is performed and a one step rotation matrix is obtained: :

$$M_{rot} = \begin{pmatrix} 0.758624 & 0.651529 \\ -0.651529 & 0.758624 \end{pmatrix}$$

In this section the new boundary is just set to the maximal and minimal value of current population in new coordinate system. After coordinate transformation the boundary of the new coordinate is : $x \in [2.54\ 12.92]$ and $y \in [-3.89\ 1.88]$. In Figure 3.12, the boundary of the new coordinate system is denoted with the rectangular box. It could be seen that after coordinate transformation the population converge to the optimum very fast. In generation 15, the optimal solution is found with a order at 10^{-3}. The same optimization process is repeated for several times, and the GACT at most time performs better than original GA.

3.5 Realistic parameter identification problems

The simple model used in last section is only used to illustrate the process of coordinate transformation in GACT. Since the simple model is in fact convex, it could be solved by

a local gradient based method such as Newton's method with more efficiency and more preciseness. However, in some realistic models where both linear correlation and multiple local optima exist, the GACT will show it's advantage. Next we consider a most common kind of optimization problem - the parameter identification problem as described in section 3.1.1.

3.5.1 Parameter identification for single gas dynamic transport model

As an example, we consider the identification of a porous membrane from a single gas dynamic transport experiment. Details will be given in section 4.1.5. To illustrate GACT it is enough to know that K_0 and B_0 are two unknown membrane parameters to be identified. For convenience, we reparametrized K_0 and B_0 to be: $K_f = ln(K_0 \times 10^8)$ and $B_f = ln(B_0 \times 10^{14})$ Then the optimum value becomes: $K_f = 2.099$ and $B_f = 1.085$. We set up an optimization problem with: $K_f \in [0.0, 2.3]$ $B_f \in [0.0, 2.3]$ and precision=0.0001. Correlation limit is still set to 0.8. Figure 3.13 is the surface plot and contour plot of the objective function. The long valley of the objective function indicates the high correlation of the parameters. The multiple minima along the valley also indicate it's a non-convex problem and should be solved with a global optimizer.

Figure 3.14 shows the results of one optimization process. From generation 11, the correlation coefficient of the population is calculated, see Table 3.2. In generation 11 the first coordinate rotation is performed with rotation matrix:

$$M_{rot} = \begin{pmatrix} 0.991967 & -0.126496 \\ 0.126496 & 0.991967 \end{pmatrix}$$

So in the next generation the correlation coefficient is greatly decreased and the converging rate is obviously increased. However, in this model the valley of the objective function

is not an exact straight line, so after the first rotation, the correlation coefficient grows up again slowly. In generation 19 a second rotation is performed with rotation matrix:

$$M_{rot} = \begin{pmatrix} 0.974874 & -0.222756 \\ 0.222756 & 0.974874 \end{pmatrix},$$

and the solution converges to the global optimum in the next few steps. The correlation coefficient decreases again after generation 25, and there's no need to perform a third rotation.

Table 3.2: Correlation coefficient in each generation

Generation	11	12	13	14	15	16	17
Corr(P1,P2)	-0.8033	-0.2880	-0.4854	-0.6978	-0.6671	-0.6526	-0.7666
Generation	18	19	20	21	22	23	24
Corr(P1,P2)	-0.7357	-0.8091	-0.1171	-0.2908	-0.2421	-0.2892	-0.2933

3.5.2 Parameter identification of multi component gas dynamic transport model

Now the problem of identifying K_0 and B_0 in a multi-component gas experiment is considered. Details will be given in section 4.1.7. K_0 and B_0 are reparametrized as section 3.5.1. Also all the optimization setup are same as section 3.5.1 expect for that the correlation limit is reduced to 0.5, because the contour of objective function is not such a regular straight line, see Figure 3.15. Although the population is not very highly correlated, and therefore the coordinate transformation becomes a little stochastic, the convergence rate of GACT is still greatly increased comparing to the GA. Coordinate rotation is performed for 3 times

at generation 23,24 and 30 with the rotation matrix:

$$M_{rot1} = \begin{pmatrix} 0.719973 & 0.694002 \\ -0.694002 & 0.719973 \end{pmatrix}$$

$$M_{rot2} = \begin{pmatrix} 0.428411 & 0.903584 \\ -0.903584 & 0.428411 \end{pmatrix}$$

$$M_{rot3} = \begin{pmatrix} 0.305896 & 0.952065 \\ -0.952065 & 0.305896 \end{pmatrix},$$

see Figure 3.16. The optimum solution is reached at about generation 40.

3.5.3 Boundary set-up after coordinate transformation

As we discussed before, after the coordinate transformation a new boundary is set for the new coordinate system. In this section the boundary is just set to the maximal and minimal value of current population in new coordinate system. This is the simplest method, but could cause two negative consequence:

1. If the new search area is smaller than the original one, then the coordinate transformation has an effect of search refinement. Theoretically, it is possible for GA optimizer to miss some global optimum outside of the new search area, because the new boundary is forcing the optimizer to converge faster. Although, in our examples this phenomenon did not occur.

2. The new search area could also exceed the original one, see Figure 3.17. This will again cause three problems:

(a) For the optimization problems with active parameter range, this may cause the GACT to converge to a out-of-range (non-existent) optimum.

(b) For some optimization problem, the objective function is not calculable. The optimizer could generate large amount of invalid chromosomes.

(c) The search area of parameters could grow with each time of coordinate transformation and therefore the search area becomes more and more diverse.

One possible solution to the problems is to check the original boundary after each crossover and mutation operation, and remove the invalid chromosomes before evaluation. The method is similar to the way how GA handle the inequality constants.This algorithm is realized in the next section. In this section, we just avoid the invalid chromosomes (such as a negative parameter) by reparametrization of the parameters.

3.6 Generalization to multi-dimensional optimization problem

The GACT is naturally generalized to solve multi-dimensional optimization problems. The basic concept is the same as described for 2-dimensional case and the detailed algorithm is described below.

3.6.1 Calculation of multiple correlations

For the n-dimensional optimization problem, there could be correlations between any two of the parameters, or there could be multiple correlations among any 3,4,...,n parameters. The total process of decorrelation should start from checking the multiple correlation for all parameters, and then proceed to n-1,n-2, .. until finally two parameters.

Before the step of decorrelation, the maximal correlation value for the parameters should be calculated, the coordinate transformation will be carried out if the maximal correlation value exceed some limit. The calculation of multiple- correlation value is described below as in reference [42].

Suppose there are n parameters to be optimized, the correlation between any two of these parameters form a $n \times n$ correlation matrix. The multiple correlation value between parameter i and the other parameters could be *estimated* by the square root of the sum of the square correlation between parameter i and the other parameters, as below:

$$R_{M,i} = \sqrt{\sum_{j=1, j\neq i}^{j=n} R_{i,j}^2} \tag{3.10}$$

Such estimation is usually not precisely the exact multiple correlation value, since it does not consider the correlation among the parameters other than i. However, this value is used to choose the *maximal correlated parameter*, and use the parameter as criterion variable for later linear regression.

If we define the criterion variable - parameter i as Y and the other parameters as a vector X, then the real correlation between Y and X is given by:

$$R = \sqrt{R_{xy} R_{xx}^{-1} R_{yx}} \tag{3.11}$$

as is illustrated in figure 3.18.

3.6.2 The Generation of rotation matrix

If the multiple correlation value for the maximal correlated parameter i is greater than some limit(for example 0.8), one step of coordinate transformation is performed. Firstly a liner regression is applied with:

$$P_i = \sum_{j=1, j\neq i}^{j=n} a_j P_j + b \tag{3.12}$$

Secondly a basis for the new coordinate system should be calculated. The above equation defines a hyperplane for the correlated parameters. For the purpose of decorrelation, one axis of the new coordinate must be chosen orthogonal to this surface, and the other axis must lie in the hyperplane and orthogonal to each other. To find such a group of vectors, firstly form a matrix composed of one orthogonal vector and n-1 linearly independent vectors in the hyperplane, as in table 3.3.

Table 3.3: Linearly independent vectors for coordinate transformation

Num.	V_1	V_2	V_3	V_4	...	V_n
1	a_1	1	0	0	...	0
2	a_2	0	1	0	...	0
3	a_3	0	0	1	...	0
...	...	...	...	...	...	...
i	-1	a_1	a_2	a_3	...	a_n
...	...	...	...	...	...	...
n	a_n	0	0	0	...	1

Secondly QR factorization is applied to the matrix, and an orthogonal basis for the new coordinate system is obtained. The matrix of orthogonal base is used as one step rotation matrix M_{rot}, and coordinate transformation is performed to each vector of parameters: $V_{newp} = M_{rot}^{-1} \times V_{oldp}$.

The new parameter orthogonal to the hyperplane of the old coordinate is then removed from the vector of parameters and the same decorrelation process is repeated for the subset of the parameters until there's no further correlation between the rest parameters or there is only one parameter left. Of course, the total rotation matrix should be updated for each

level of decorrelation, as equation 3.9.

3.6.3 The boundary set-up

The GACT works like an *automatic reparametrization* process. After each step of reparametrization, the new boundary of the parameters should be recalculated. In this section, the method of new boundary calculation is different to that of section 3.5.3 in that, in order to avoid a premature convergence of the population the boundary is not calculated from maximal or minimal possible values of the current population but always from the original parameter limits. For optimization problem, each parameter to be optimized is limited between two boundary values, and the total possible parameter area form a n-dimensional *hypercube* in the current coordinate system. Since the coordination rotation is a linear transformation, the maximal or minimal possible values of parameters must lie on some vertices of the original hypercube. For optimization problems of n parameters there are in total 2^n vertices. In this section the maximal and minimal values are calculated by simply comparing the values of all 2^n vertices in new coordinate system. For even more parameters to optimize, it's also possible to use a simplex optimization algorithm to search for the maximal and minimal values, or more simply, use the extreme values in population as boundaries, as described in section 3.5.3.

The new boundary is only a necessary but not sufficient condition for the newly generated chromosomes to lie in the original parameter area. After each step of crossover and mutation, before evaluation, the parameters are transferred back to the original coordinate system to check for the original boundary and invalid chromosomes outside of the original parameter limit are eliminated. The total process of GACT is depicted in figure 3.19.

3.6.4 Comparison with the traditional GA

The discussed GACT is in fact applied thoroughly in all of the parameter identification problems described in section 4.2 to increase the convergence speed of optimization. To illustrate the advantage of GACT, the parameter identification problem described in section 4.2.1 is tested for both GA and GACT. The parameter settings for both algorithm are the same: $P_{mutation} = 0.01$, $P_{crossover} = 0.1$, and the actual stop criterion is always set to be maximal step=50. The initial population size is set to be 100 and 1000 for both algorithms and the final results of the objective function are listed in table 3.4. It's obvious that the GACT has better performance, since GACT has much lower average objective value comparing to GA with same population size. It could also be noticed that the optimization results of GACT is approximately close to that of GA with 10 times more population.

Table 3.4: Comparison between GACT and GA

Test Number	GA(P=100)	GA(P=1000)	GACT(P=100)	GACT(P=1000)
1	-7.24	-9.09	-9.73	-10.43
2	-7.61	-10.11	-10.39	-11.17
3	-9.40	-8.96	-11.67	-10.26
4	-9.38	-10.28	-10.79	-11.32
5	-6.25	-8.13	-7.31	-9.86
6	-7.42	-11.61	-8.53	-10.69
7	-5.53	-10.57	-9.75	-10.34
8	-7.21	-9.72	-7.44	-10.39
9	-7.13	-9.66	-8.62	-8.92
10	-7.91	-8.76	-8.67	-11.43
Mean	-7.51	-9.69	-9.29	-10.48

3.7 Conclusion and discussion: what is the nature of GA

Let's return to the mechanism of original biological system where the GA is inspired. The basic advantage of sexual reproduction is that the "good gene" could be preserved and reproduced, and the good genes together could be combined to form a better chromosome or organism. However there's an intrinsic assumption here which is not yet proven, that any good gene affects the performance of chromosomes independently, without any correlation with the other genes. Although it's still an open question in biology, there's no doubt that in many optimization problems some parameters are highly correlated. Therefore, it's difficult to claim how a single parameter will influence the objective function. From some optimization problems of GA, there could be no apparent distinction between "good gene" or "bad gene", but the way of their how they are combined defines the fitness of the whole chromosome or the organism. In such case, in order to form a good chromosome offspring, it's not enough to simply search for the good gene, instead one should analyze the relations of the different genes and mechanism how they work together to take effect on fitness.

As we mentioned before, GA uses a *heuristic* search strategy. In fact, the traditional *hill climbing* algorithm can also be defined as a kind of *heuristic* method. The common character of any heuristic optimizer is that it assumes there exists some pattern in the surface of objective function, and the optimizer can find this pattern and use it to guide the search process. For example, all of the gradient based optimizer assumes the objective function is continuous and at least locally convex, therefore the optimizer could take use of the gradient information of the objective function to search for the optimum. The Newton's method is usually faster than steepest descent method because in addition to gradient it takes use of the curvature information of the objective function. The GA optimizer, as discussed before, can take use of any pattern that could be described by schemata. However, although the schemata can describe the most common patterns, such as the adjacency or the frequency of

the optimal objective values, it cannot describe the correlation among parameters. Therefore, the purpose of this work is the improve the efficency of GA by recognizing and taking use of the correlation information among the parameters and accelerate the search process. The GACT optimizer is then applied to solve the practical problems in chapter 4 and has proved successful.

Since linear correlation of parameters is also a widely existent phenomenon in optimization problems, the GACT could be also extended to solve some other optimization problems. Also, further improvement of this algorithm is possible based on the same assumption.

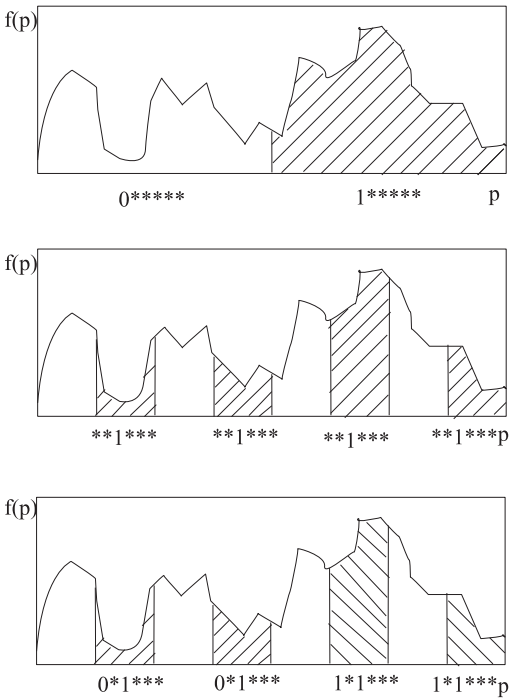

Figure 3.6: Hyperplane for 1-dimensional GA optimization, the shaded area in first and second graph represent order 1 schemata 1***** and **1*** respectively, the shaded area in bottom graph represent two different order 2 schemata which can be obtained by combination of the above two order 1 schemata.

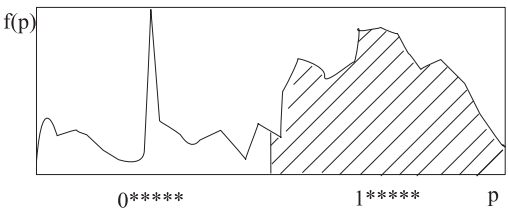

Figure 3.7: An example of global optimum located in hyperplane with low average fitness

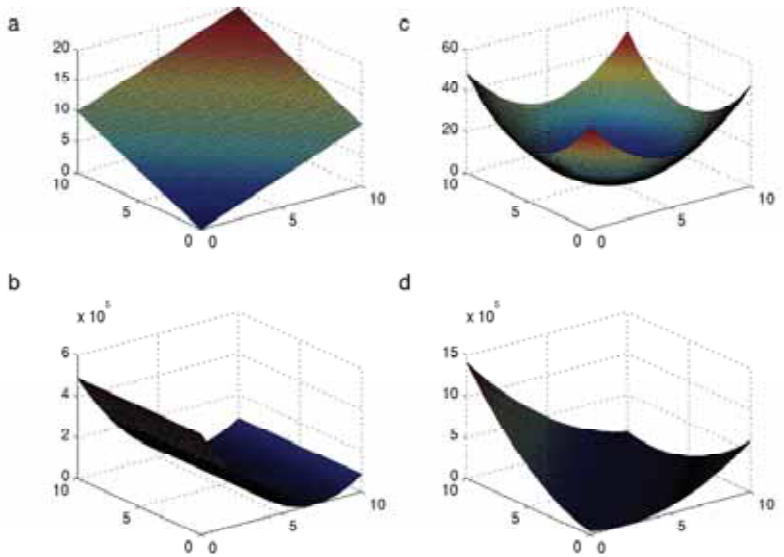

Figure 3.8: Objective functions: $(a) z = x + y$;
(b)$z = (x-5)^2 + (y-5)^2$;
(c)$z = 10000((x-7)^2) + (y-5)^2$; (d)
$z = 10000(((x-y)-2)^2) + (x+y-12)^2$;

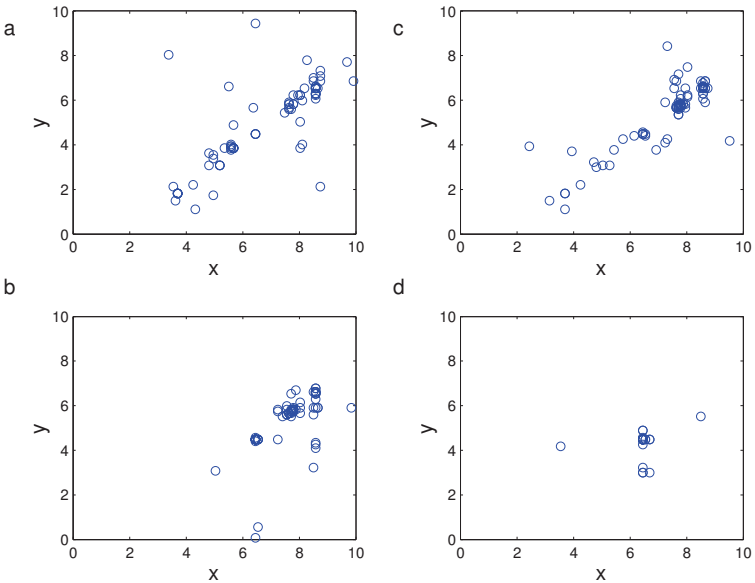

Figure 3.9: Population during optimization of function 4 with traditional GA, at generations a=10, b=15, c=20, d=40

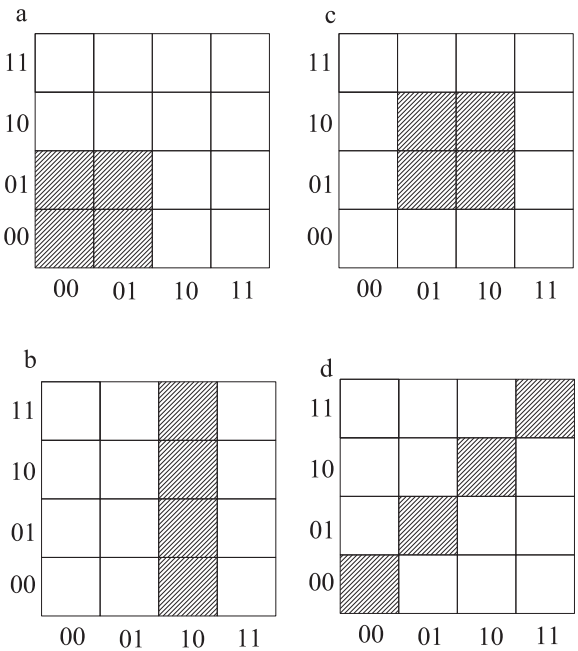

Figure 3.10: Optima area for the functions in figure 3.8

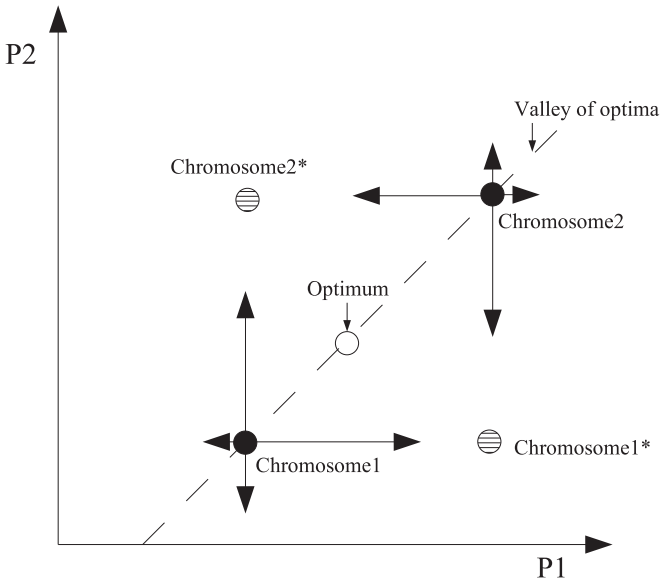

Figure 3.11: Crossover operator in a linearly correlated population.Chromosome1 and chromosome2 are the parents, and chromosome1* and chromosome2* are the offspring when the crossover points lie exactly between the parameters. The arrows indicate the possible possible direction of offspring, which can also describe the mutation operator. The dashed line shows the valley of optima, which could be calculated by linear regression.

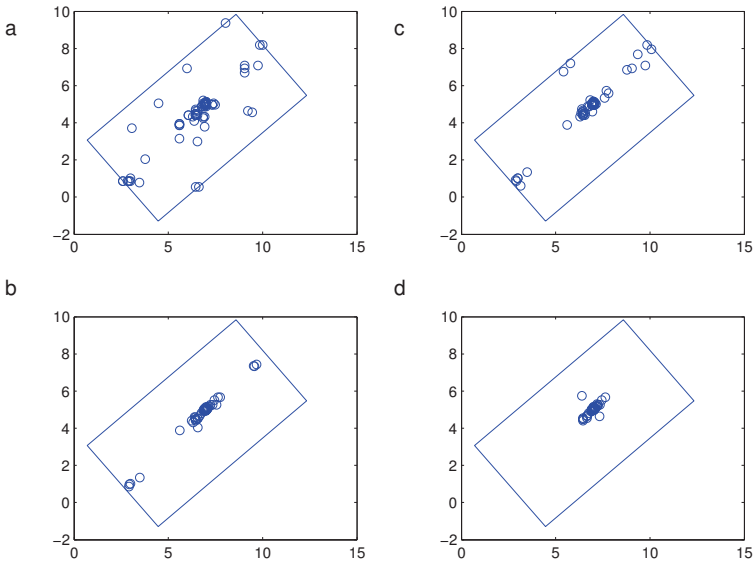

Figure 3.12: Population during optimization of function 4 with coordinate transformation (rectangular box represents the new boundary) , for generations a=11, b=13, c=15, d=17

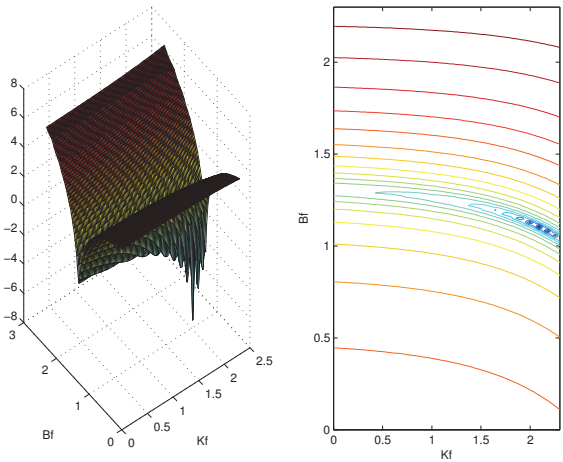

Figure 3.13: Objective function for identification of membrane parameter by single gas dynamic permeation experiment;

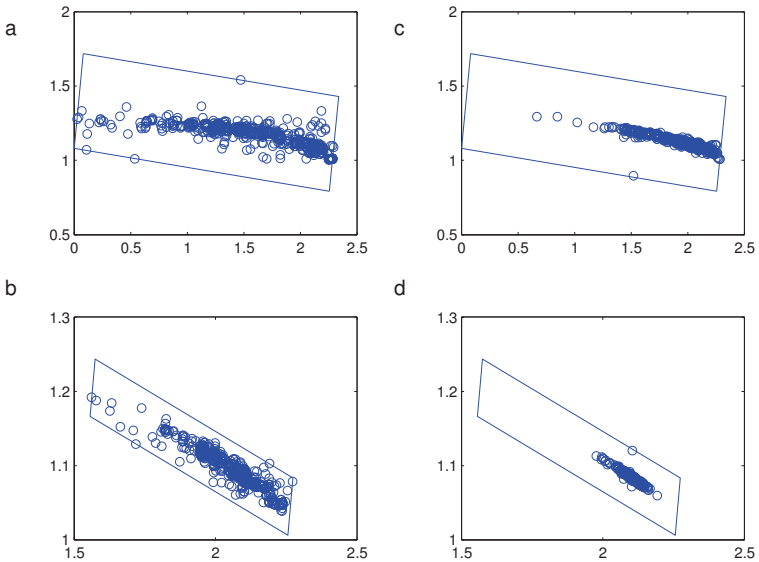

Figure 3.14: Population during parameter identification of single gas dynamic permeation model, for generation: a=11, b=15, c=19, d=25;

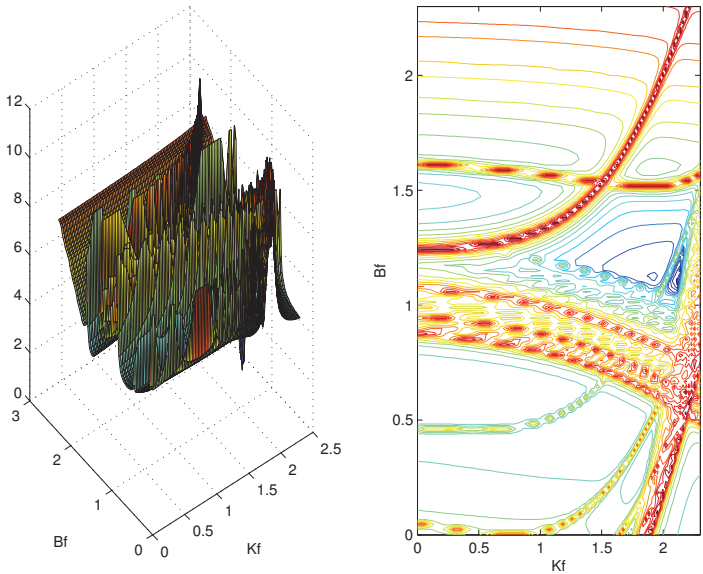

Figure 3.15: Objective function for identification of membrane parameter by multi gas dynamic permeation experiment;

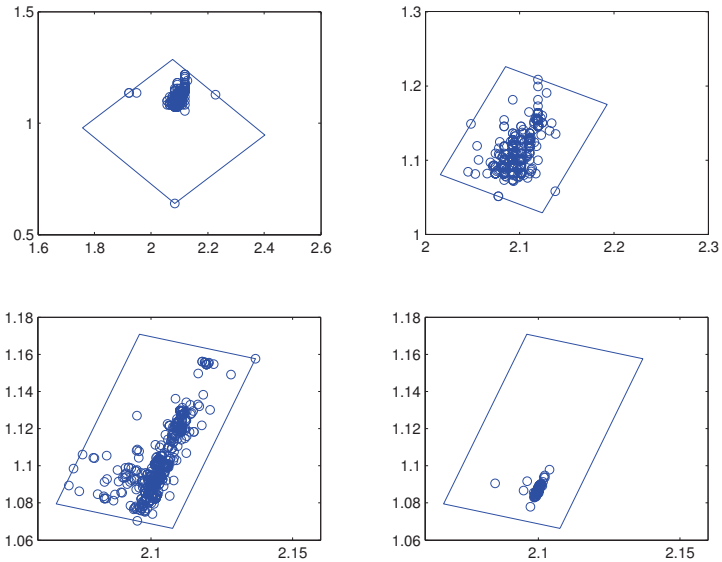

Figure 3.16: Population during parameter identification of multi gas dynamic permeation model, for generation: a=23, b=24, c=30, d=40;

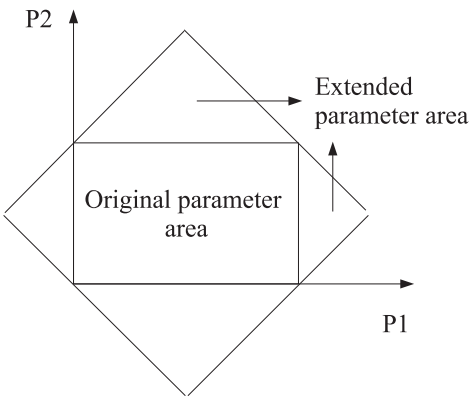

Figure 3.17: Enlargement of parameter area after coordinate rotation

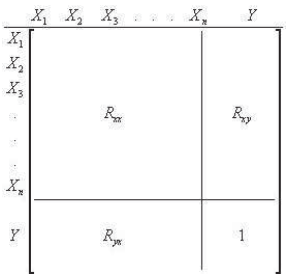

Figure 3.18: Calculation of multiple correlation

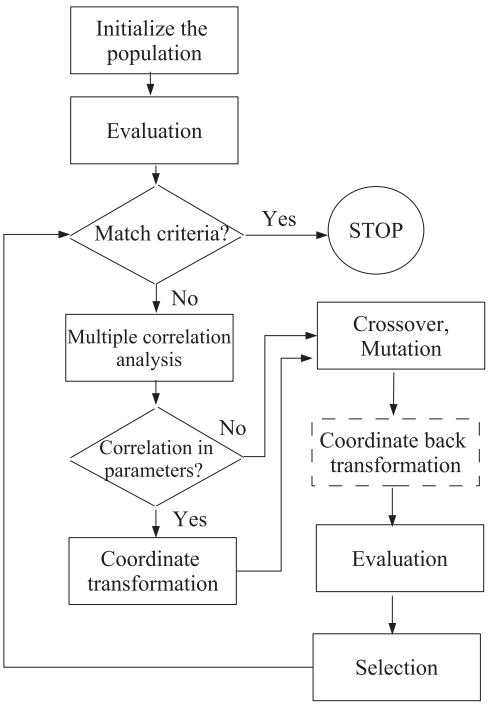

Figure 3.19: Outline of a Genetic Algorithm with Coordinate transformation

Chapter 4

Experimental design for identification of membrane parameters

4.1 Mass transport through single-layer membrane

4.1.1 Set-up for different experimental schemes

Traditionally, three main types of gas transport experiments are performed for identification or validation of mass transport coefficients [10, 13, 43]:

- Steady gas permeation experiment.
- Isobaric diffusion experiment.
- Transient diffusion experiment.

In this section we consider two additional *Gedankenexperiment*, and the single gas permeation experiments are separated into two different kinds of experiments: experiments with only one kind of gas or with several different kinds of gas. So the six experimental schemes considered here are:

- Single gas steady state permeation experiment.
- Single gas dynamic permeation experiment
- Multi-component single-gas steady state permeation experiments
- Multi-component gas dynamic transport experiment
- Isobaric diffusion experiment.
- Transient diffusion experiment.

In this simulation we use a model of a tubular ceramic membrane reactor as described in section 2.2.4 and [13], but the membrane is considered to be composed of the support layer only, which equals to a homogeneous membrane. All the parameter values were already identified in [13] and are given in table 4.1. The reactor set-up is described in figure 4.1. The tubular membrane separates the reactor into two chambers, the tube side (defined as chamber A) and the annulus side (defined as chamber B). Automatically controlled mass flows can be provided on both sides, while the outlets of both sides can be controlled by valves. When the valve is open the pressure of the corresponding chamber is considered to be the same as the environmental pressure. The outlet flow rate and the concentrations and pressures in both chambers are supposed to be measured by some instrument instantly.

Table 4.1: Physical parameters of the tubular membrane

composition	thickness [m]	length [m]	inner radius [m]	outer radius [m]	K_0 [m]	B_0 $[m^2]$
$\alpha - Al_2O_3$	5.5e-3	0.12	10.5e-3	16e-3	8.16e-8	2.96e-14

(a)

(b)

(c)

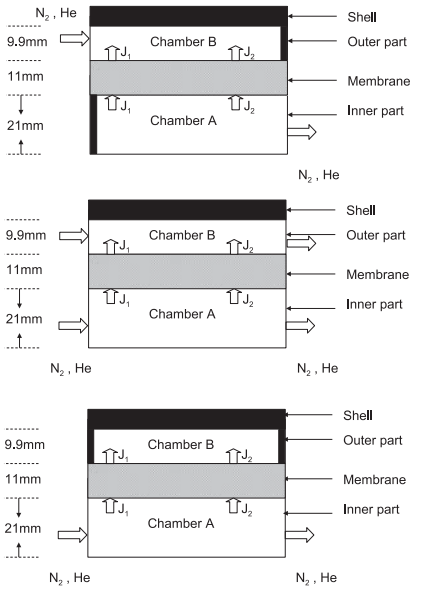

Figure 4.1: Schemes for different identification experiments: (a) permeation experiments; (b) isobaric diffusion experiments; (c) transient diffusion experiments

Three different reactor schemes in figure 4.1 summarize the set-up of six different experiments. Figure 4.1 (a) stands for the different permeation experiments, figure 4.1 (b) and figure 4.1 (c) describe the isobaric and transient diffusion experiments.

4.1.2 Conditions for experimental design

The purpose of this section is to theoretically study the efficiency of each experiment scheme for parameter identification. Since the experimental conditions have important effect on parameter identification, the experiment schemes should be compared under their

corresponding optimal experimental conditions. Therefore, OED is applied for each experiment scheme in order to find the optimal condition. And since it's only a theoretical comparison of different experimental scheme, and not experimental design for real parameter identification task, for simplicity the inlet gas flow rate is considered as the only control parameter. In the following sections more realistic experimental conditions will be considered. The task of experimental design is to find the appropriate operation conditions that get the most information on the unknown parameters out of a limited number of experiments or a limited total experimental time. Here for simplicity we assume that all the states in the system (the concentrations in both chambers, pressures in both chambers, outlet flow rates) can be observed directly, and all observations have one percent relative standard deviation. The control parameters are the inlet flow rates of the gases. The total inlet flow rate for all gases is limited within 0-20 ml/min. For dynamic experiments the feeding profiles are set piecewise-constant, with a constant interval of one second, and a total experimental time of ten seconds. Except for the isobaric diffusion experiment the pressure of chamber A is always set to 1 bar, identical to the normal environmental pressure. The commonly used nitrogen and helium are selected as gases for multi-component gas experiments and only nitrogen is used for single-gas experiments. The other specific conditions will be explained in the following corresponding sections. For all of the OED, the e-criterion is used as the default design criterion.

4.1.3 Complete model of the membrane reactor

For a two component mixture, the mass balances in the two chambers A and B of the membrane reactor are:

$$\frac{dC_{2B}}{dt} = \frac{1}{V_B}(\frac{F_{in,2B} \times P_B}{RT_B} - F_{out,B}C_{2B} + \dot{N}_2) \tag{4.1}$$

$$\frac{dC_{1B}}{dt} = \frac{1}{V_B}(\frac{F_{in,1B} \times P_B}{RT_B} - F_{out,B}C_{1B} + \dot{N}_1) \tag{4.2}$$

$$\frac{dC_{2A}}{dt} = \frac{1}{V_A}(\frac{F_{in,2A} \times P_A}{RT_A} - F_{out,B}C_{2A} - \dot{N}_2) \tag{4.3}$$

$$\frac{dC_{1A}}{dt} = \frac{1}{V_A}(\frac{F_{in,1A} \times P_A}{RT_A} - F_{out,B}C_{1A} - \dot{N}_1) \tag{4.4}$$

$$\tag{4.5}$$

For simplicity here the temperature gradient is not considered, so we assume $T_B = T_A = T_{mem}$. Further, the hold-up of the membrane is neglected. The ideal gas law is applied to calculate the pressure in two chambers.

For model of homogeneous cylindrical membrane, equation (2.20) can be rewritten as:

$$-\frac{2\pi L}{RT\ln\left(\frac{r_{mo}}{r_{mi}}\right)}[-\frac{P_A+P_B}{2}(x_{i,A}-x_{i,B})- \quad (1+\frac{B_0}{D_{K,i}\eta}\frac{P_A+P_B}{2})\frac{x_{i,A}+x_{i,B}}{2}(P_A-P_B)]$$
$$= \sum_{j=1,j\neq i}^{n} \frac{\frac{x_{j,A}+x_{j,B}}{2}\dot{N}_i - \frac{x_{i,A}+x_{i,B}}{2}\dot{N}_j}{D^e_{ij}} + \frac{\dot{N}_i}{D_{K,i}} \tag{4.6}$$

For single gas permeation experiments, the above equation can be further simplified to:

$$\frac{\dot{N}}{(P_A-P_B)} = -\frac{2\pi L}{RTln\left(\frac{r_{mo}}{r_{mi}}\right)}\left(\frac{4}{3}K_0\sqrt{\frac{8RT}{\pi M}} + \frac{B_0}{\eta}\frac{P_A+P_B}{2}\right) \tag{4.7}$$

The dynamic viscosity of the gas mixture is calculated by Wilke's law [44]. Note that the parameter $\frac{\varepsilon}{\tau}$ be expressed by B_0 and K_0:

$$\frac{\varepsilon}{\tau} = \frac{K_0^2}{2B_0} \tag{4.8}$$

so there remain only two parameters to be identified. The diffusion coefficient is calculated by Fuller's method as in equation 2.16.

4.1.4 Experimental design for single gas steady permeation experiment

Single gas permeation experiments are widely used for the identification of mass transport parameters. The experimental scheme is sketched in figure 4.1-a. To identify the two structural parameters, at least two experiments should be performed. It is intuitively clear that one should perform some high flow rate experiments, where bulk flow has an important effect, and some low flow rate experiments, where Knudsen diffusion dominates. To find the optimal experimental conditions, experimental design has been done using the e-criterion for optimization. Experiments with between two and six different steady state conditions are considered. The resulting optimized inlet flow rates are listed in table 4.2, the corresponding design criteria and predicted standard deviations are listed in table 4.3. As we can see from table 4.2 the experiments are basically performed in 2 different flow rates: While one or two experiments are performed at maximum flow rate, more experiments are repeated in low flow rate condition. The reason is that, based on the assumption of Gaussian distributed noise with zero mean, repeated experiments are able to reduce the influence of measurement noise. The repetition of low flow rate experiments indicates Knudsen diffusion is relatively less important for mass transport in this case and thus K_0 is relatively

difficult to be identified.

From table 4.3 it's easy to see that the estimated variance of K_0 is much larger than B_0, which confirms that the Knudsen coefficient cannot be predicted well in this experiment. The reason for this problem is that the effect of bulk flow is much bigger than the Knudsen diffusion for nitrogen. So a possible solution might be to change to some gas with smaller molecular weight, such as helium. The experiments with different kinds of gas are discussed in section 4.1.6

Table 4.2: Designed inlet flow rate for single gas steady state experiments (Num Exp = number of experiments)

Num Exp	F_{in1}	F_{in2}	F_{in3}	F_{in4}	F_{in5}	F_{in6}
2	2.00e+01	8.39e+00				
3	2.00e+01	7.83e+00	7.83e+00			
4	2.00e+01	7.42e+00	7.42e+00	7.42e+00		
5	2.00e+01	2.00e+01	8.08e+00	8.08e+00	8.08e+00	
6	2.00e+01	6.85e+00	6.85e+00	6.85e+00	6.85e+00	6.85e+00

Table 4.3: E-criterion and estimated standard deviation for single gas steady state experiments

Num Exp	E-obj	Std. $K_0/10^{-8}$	Std. $B_0/10^{-14}$
2	-8.98e-02	3.33	2.39e-01
3	-1.54e-01	2.54	1.90e-01
4	-2.03e-01	2.21	1.70e-01
5	-2.48e-01	2.00	1.47e-01
6	-2.79e-01	1.89	1.50e-01

It is also obvious that the variances reduce as the number of experiments increases. Without any further experimental design, the variances can be reduced proportionally to the number

of experiments just by repeating the same experiments many times for any group of results in table 4.2.

4.1.5 Experimental design for single gas dynamic permeation experiment

In this model the membrane is assumed to possess negligible hold-up, so the term *dynamic* experiments only refers to the dynamics inside the tubular and annulus chambers. If the pressures in both chambers are controlled directly, the experiments can be regarded to be composed of a series of steady state experiments. The benefit of dynamic experiments is to improve of efficiency of experiments and save experimental time. Again nitrogen is used as the process gas, and the the piece-wise constant feeding profile of inlet flow rate is optimized. The resulting feeding profile is shown in figure 4.2. In analogy to the steady state case, the experiment starts from a high flow rate followed by a low flow rate and the stop of the feeding for a moment. Then the same process is repeated. For dynamic experiments, the value of FIM depends on the frequency of sampling. The variances reduce proportionally to the increase of sampling points. Here we consider a constant sampling interval of 1 second, and hence 10 total measurements (for both pressure in chamber B and outlet flow rate in chamber A). The optimization criterion and variance predicted by FIM are listed in table 4.4. The estimated precision is about one order of magnitude higher than for the steady state experiments considered in 4.1.4.

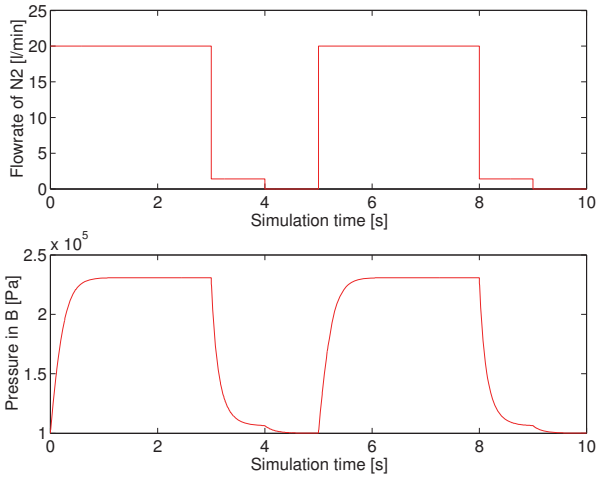

Figure 4.2: Designed feeding profile for single gas dynamic experiment

Table 4.4: E-criterion and estimated standard deviation for single gas dynamic experiment

Exp Time	E-obj	Std. $K_0/10^{-8}$	Std. $B_0/10^{-14}$
10s	-6.74+00	3.83-01	3.72e-02

4.1.6 Experimental design for multi-component single-gas steady state permeation experiment

For multi single-gas steady permeation experiments, nitrogen and helium are supposed to be supplied to the reactor at the same time(although the design result shows it's more efficient to feed nitrogen and helium separately). The total inlet flow rate and the molar

fraction of helium are used as control parameters. Since the concentrations of nitrogen and helium are assumed to be measurable in both chambers, one experiment is enough for the identification of the two parameters. The experimental design results are listed in table 4.5 and table 4.6 for the case of one to six steady state conditions per experiment. The corresponding design criteria and predicted standard deviations are given in table 4.7. For groups of two and more experiments the estimated standard deviation is close to single gas dynamic experiments and much superior to the single gas steady state experiments, which shows the advantage of multi-component gas experiments: the parameters can be estimated more precisely with much less experiments. In reality, however, the measurement of concentrations of gases would be much more difficult than simple pressure measurements, and the variance of the measurement noise might be much bigger (here we assume one percent standard deviation for all measurements).

Table 4.5: Designed inlet flow rate for multi single-gas steady state experiments.

Num Exp	F_{in1}	F_{in2}	F_{in3}	F_{in4}	F_{in5}	F_{in6}
1	7.09e+00					
2	2.00e+01	1.85e+01				
3	2.00e+01	1.63e+01	1.63e+01			
4	1.51e+01	1.51e+01	1.51e+01	2.00e+01		
5	1.42e+01	2.00e+01	1.42e+01	1.42e+01	1.42e+01	
6	1.63e+01	2.00e+01	1.63e+01	2.00e+01	1.63e+01	1.63e+01

Table 4.6: Designed inlet molar fraction for multi sinlge-gas steady state experiments.

Num Exp	X_{in1}	X_{in2}	X_{in3}	X_{in4}	X_{in5}	X_{in6}
1	1.84e-04					
2	0	1				
3	0	1	1			
4	1	1	1	0		
5	1	0	1	1	1	
6	1	0	1	0	1	1

Table 4.7: E-criterion and estimated standard deviation for multi single-gas steady state experiments.

Num Exp	E-obj	Std. $K_0/10^{-8}$	Std. $B_0/10^{-14}$
1	-2.82e-01	1.87e+00	2.31e-01
2	-8.42e+00	3.42e-01	5.12e-02
3	-1.22e+01	2.83e-01	4.89e-02
4	-1.46e+01	2.58e-01	4.79e-02
5	-1.64e+01	2.43e-01	4.73e-02
6	-2.44e+01	2.00e-01	3.46e-02

4.1.7 Experimental design for multi-component gas dynamic transport experiment

In the multi-component gas dynamic experiments both nitrogen and helium are supplied continuously into chamber B, see figure 4.1-a. This method allows to change the pressure and the molar fraction in chamber B continuously and consequently provides the maximal information of the system since all the three transport mechanisms are taking effect. For the corresponding OED problem we set a limitation of the total inlet flow rate to 0-20l/min, and postulate piecewise constant feeding profiles for both gases. The optimized feeding profile

is shown in figure 4.3, the pressure of chamber B is shown in figure 4.4. The e-criterion and the predicted variances are given in table 4.8. As expected the precision of parameters is greatly improved in this experiment.

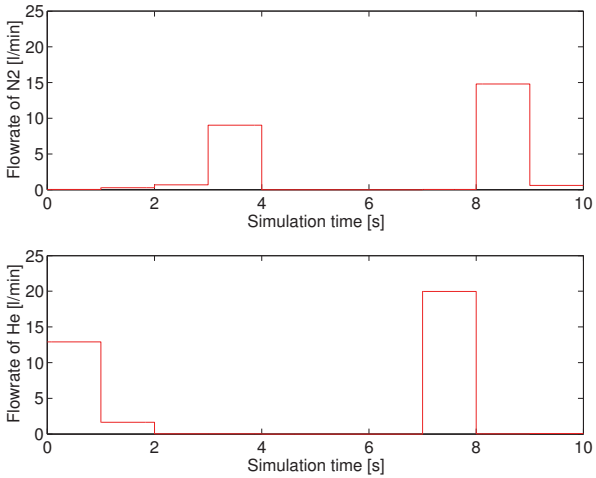

Figure 4.3: Feeding profile of multi-component gas dynamic experiment

Table 4.8: E-criterion and estimated standard deviation for multi-component gas dynamic experiment

Exp Time	E-obj	Std. $K_0/10^{-8}$	Std. $B_0/10^{-14}$
10s	-2.36e+07	1.75e-04	1.31e-04

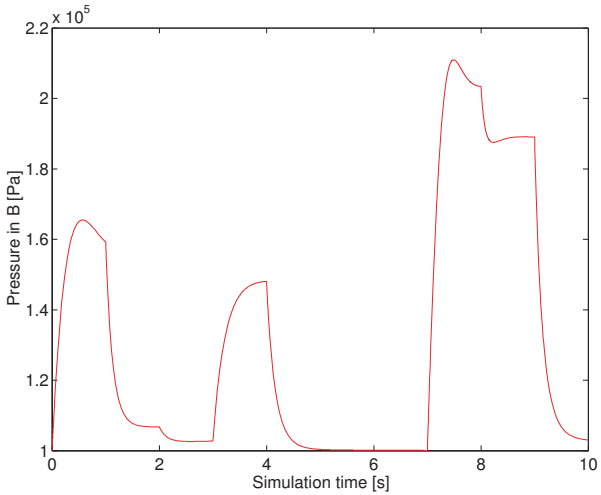

Figure 4.4: Pressure change in chamber B during multi-component gas dynamic experiment

4.1.8 Experimental design for isobaric diffusion

For isobaric diffusion experiments, nitrogen is supplied to chamber A and helium is supplied to chamber B. The pressures of both chamber are kept constant at 1 bar. The inlet flow rates of both chambers are used as control parameters. All the concentrations and outlet flow rates are measured. For isobaric diffusion, the DGM (2.20) can be simplified to :

$$\frac{2\pi L\bar{P}\Delta x_i}{RTln\left(\frac{r_{mo}}{r_{mi}}\right)} = \sum_{j=1,j\neq i}^{n} \frac{\bar{x}_j\dot{N}_i - \bar{x}_i\dot{N}_j}{D^e_{ij}} + \frac{\dot{N}_i}{D^e_{K,i}} \tag{4.9}$$

Now we have only Knudsen diffusion and molecular diffusion. As these are only secondary

effects for the transport of nitrogen and helium, this experiment seems to be a bad choice for parameter identification. (but if $\frac{\varepsilon}{\tau}$ is known, it is possible to identify K_0 directly, because the mass transport is independent of B_0 as follows from (4.9)). This is confirmed by the results listed in table 4.9, 4.10 and 4.11. Notice that in table 4.10 the value of B_0 is calculated from K_0 and $\frac{\varepsilon}{\tau}$ in order to compare the results with other experimental schemes.

Table 4.9: Designed inlet flow rate in chamber A for isobaric diffusion experiments.

Num Exp	F_{in1}	F_{in2}	F_{in3}	F_{in4}	F_{in5}	F_{in6}
2	1.90e-04	2.00e+01				
3	7.27e+00	1.80e-04	6.07e+00			
4	1.61e+01	1.82e-04	7.87e+00	1.26e+01		
5	1.57e+01	1.91e+01	5.28e+00	1.85e-04	1.15e+01	
6	1.82e-04	1.84e+01	1.14e+01	7.70e+00	1.23e+01	1.48e+01

Table 4.10: Designed inlet flow rate in chamber B for isobaric diffusion experiments.

Num Exp	F_{in1}	F_{in2}	F_{in3}	F_{in4}	F_{in5}	F_{in6}
2	2.00e+01	1.11e+00				
3	1.29e+01	1.18e+01	7.34e-01			
4	5.07e-01	1.41e+01	3.76e+00	4.13e-01		
5	1.39e+01	6.01e-01	1.05e+01	2.00e+01	1.91e+00	
6	1.13e+01	6.47e+00	9.40e+00	1.05e+01	4.96e-01	4.49e-01

Table 4.11: E-criterion and estimated standard deviation for isobaric diffusion experiments.

Num Exp	E-obj	Std. $K_0/10^{-8}$	Std. $B_0/10^{-14}$
2	-3.65e-02	4.19e+00	3.14e+00
3	-4.16e-02	3.92e+00	2.95e+00
4	-6.79e-02	3.07e+00	2.31e+00
5	-6.46e-02	3.14e+00	2.37e+00
6	-7.18e-02	2.98e+00	2.25e+00

4.1.9 Evaluation of the transient diffusion experiment

For the transient diffusion experiment, the reactor is first filled with nitrogen in both chambers, then helium is fed into chamber A with a constant flow rate of 2 l/min, as shown in figure 4.1-c. While the pressure of chamber A is kept constant, the pressure of chamber B will increase for a short time because the diffusion of helium if faster than that of nitrogen, then drop to the same value as in chamber A, see figure 4.5. The e-criterion of the Fisher information matrix and the predicted variances are listed in table 4.12. While the E-criterion is on the same level as for single gas dynamic experiments and multi-component gas steady experiments, the obvious benefit is that the predicted standard deviations for the two parameters are very close, which means we have similar precision for both parameters. Another advantage of this experimental scheme is that less control parameter are required compared to the dynamic experiments, therefore the possibility of variances caused by the stochastic change of inlet is reduced.

4.1.10 Analysis of the experimental design results

In the previous part of this work, the lower bound of variances of the parameters has been estimated by the Cramér-Rao inequality: $\sigma_j^2 \geq (\text{FIM}^{-1})_{jj}$, where the identity is valid for

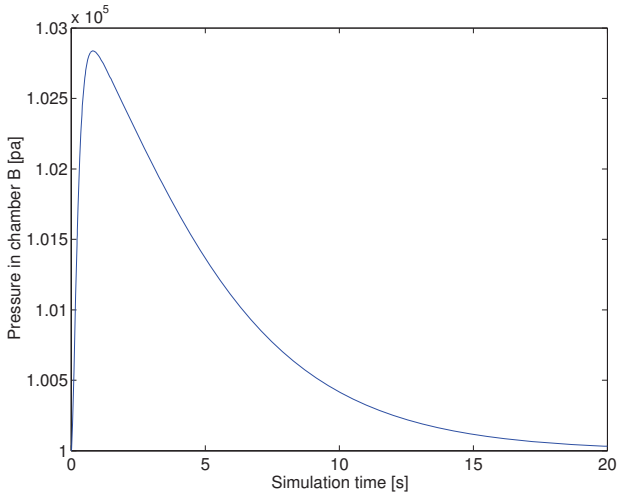

Figure 4.5: Pressure change in chamber B during transient diffusion

Table 4.12: E-criterion and estimated standard deviation for the transient diffusion experiment

Exp Time	E-obj	Std. $K_0/10^{-8}$	Std. $B_0/10^{-14}$
20s	-5.51e+00	1.60e-01	4.26e-01

models that are linear in their parameters, and for normally distributed measurement noise. However for nonlinear models, the parameter identification results may be different from the prediction of Cramér-Rao bound because:

1. The confidence interval itself for the nonlinear model may be much bigger than the Cramér-Rao bound prediction.

2. The confidence interval by Cramér-Rao prediction is always a symmetric Gaussian shape curve around the reference value, while in reality asymmetries may appear.

3. Since the cost function is non-convex, for a LDM method, the optimization results strongly depend on the initial guess of the parameters, and may converge to some wrong local minimum.

4. For a global optimizer, the results of the parameter identification strongly depend on the quality of the optimizer. The stochastic nature of a genetic optimizer will incorporate new uncertainties into the identification results.

In this work, we use the bootstrap method [25] to compare the prediction of confidence interval by Cramér-Rao bound,LDM optimizer, and hybrid optimizer. For simplicity, only the results of the dynamic multi-component gas experiment are presented, since it has the best performance in the FIM based OED part.

Contour of cost functions

The contour plot of the cost function in equation (3.1) gives a straight forward illustration for the parameter identification problem. Figure 4.6 shows contour plots of the cost function of the dynamic multi-component gas experiment. Obviously, multiple local minima exist in the whole range of parameter sets. Note that the global minimum is always located at the center of the graphs. It is easy to see that the size of the attraction region of the global minimum is smaller than the attraction regions of a nearby local minima, and thus causes problems for both GA and LDM optimizers. For a local optimizer, a very small deviation of initial values will cause the convergence to wrong local minima. For genetic optimizer, as a heuristic optimizer, it is also very difficult to converge to a small attraction region (It's like "look for a needle in the sea"). One basic problem of traditional OED is

that, for a nonlinear model, it only improves the ”sharpness” (gradient) of the attractive region around the global optimum, but cannot improve the total size of attractive region. And not yet any effective solution has been found. In this case, the attraction region of the global minimum is approximately smaller than 1 percent of parameter deviation, and very difficult to be found.

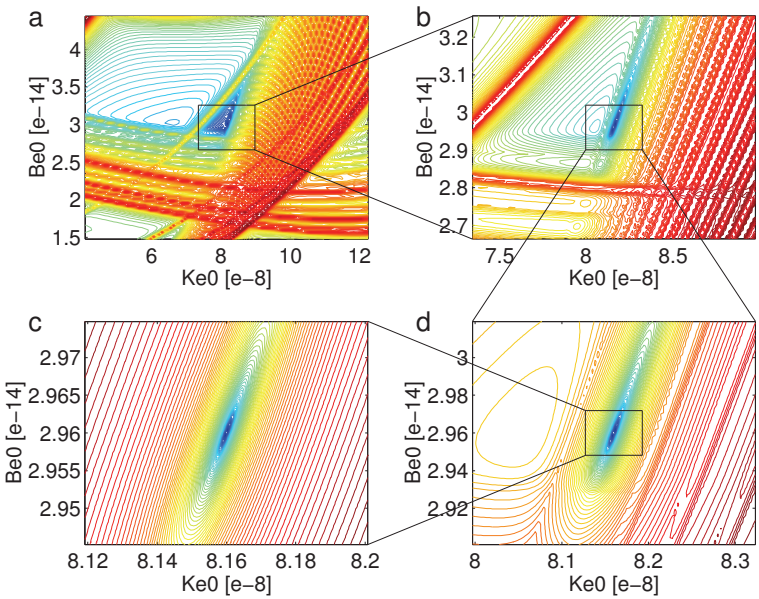

Figure 4.6: Contour of cost functions for designed dynamic multi-component gas experiment: a b c d with 50%, 10%, 2%, 0.4% deviation of parameters, respectively

One merit of this experimental scheme is that it is robust against the influence of noise.

Figure 4.7 shows the contour of the cost function calculated for one sample of measurement values with 10 percent standard deviation noise. The position of the optimum is almost not changing. Figure 4.8 contains the the corresponding contour plot for a dynamic single gas experiment with the same noise level. The shift of the global optimum is much stronger which makes the advantage of the multi-component gas experiment obvious.

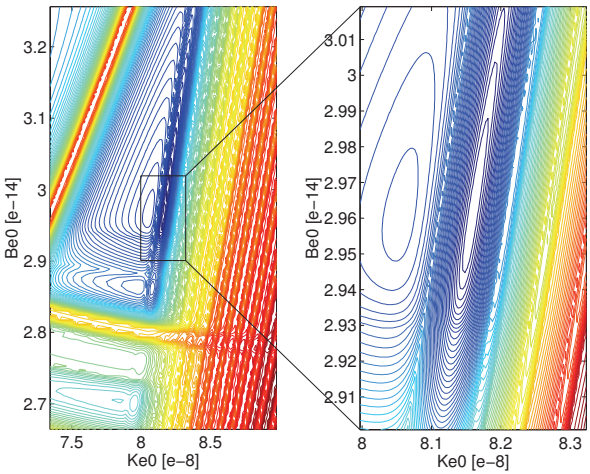

Figure 4.7: Contour of cost functions for the designed dynamic multi-component gas experiment with 10% noise: left part with 10% deviation for parameters, right part with 2% deviation

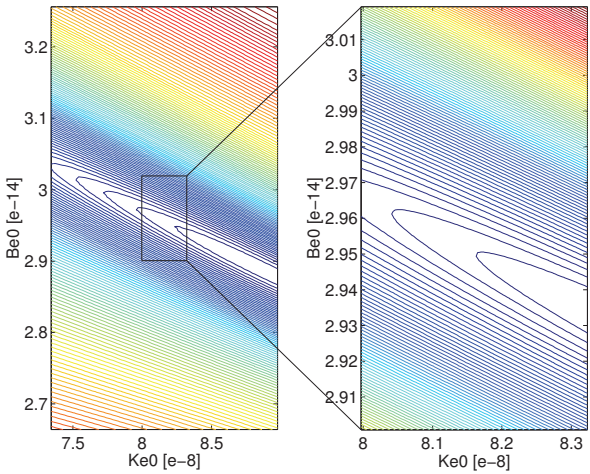

Figure 4.8: Contour of cost functions for the designed dynamic single-gas experiment with 10% noise: left part with 10% deviation for parameters, right part with 2% deviation

Bootstrap analysis

Again, only the dynamic multi-component gas experiments are analyzed by bootstrap method. By applying the feeding profile of figure 4.3 and adding 10 percent additional noise to the measurements, a replication of B=100 samples is generated for both optimizers. The comparison of both methods and the prediction by the Cramér-Rao bound are depicted in table 4.13. The real variances of the identified parameters are much bigger than the FIM based prediction, which implies high nonlinearity of this multi-component gas dynamic transport model. The results are visualized in figure 4.9, which illustrates that most of the estimated parameters lie out of the ellipse, which is a 99.9% CI prediction by FIM. It

is also interesting to compare the estimates by different optimizers. As expected, the LDM optimizer seems to perform better than the hybrid optimizer in variance of estimates but only because the initial values of the parameters are exactly *real* values. Instead of finding the real global optimum the ld optimizer tends to be caught in a local minimum close to the initial values, and thus has a smaller covariance matrix. On the other hand, it also happens that the LDM optimizer ignores a the nearby optimum and converges to some distant local minimum. Considering the number of extreme results of estimates, the performances of the LDM optimizer are even worse than that of the hybrid optimizer. This phenomenon is more obvious in figure 4.10 that contains the bootstrap results for 50% noise, where many results of LDM optimization should be excluded by some outlier analysis. And when starting from *far away* initial values, the results of LDM optimizer apparently have no chance to reach the real values, just as we expected, see figure 4.11. In summary, the hybrid optimizer should be a more appropriate method for bootstrap analysis. However, the LDM optimizer is definitely superior to the hybrid optimizer in terms of time consumption. The ld optimizer in combination with the bootstrap analysis is much better than the FIM method in terms of estimates analysis and CI prediction. So it may be a good compromise between accuracy and computational costs.

Table 4.13: Bootstrap analysis of mean and standard deviation of parameters

Parameter	Mean/ Std. of FIM	Mean/ Std. of LDM opt	Mean / Std. of hybrid opt
$K_0/10^{-8}$	8.16 / 5.53e-4	8.1582 /3.7e-3	8.1586 / 4.4e-3
$B_0/10^{-14}$	2.96 / 4.14e-4	2.9587 /4.2e-3	2.9588 / 5.2e-3

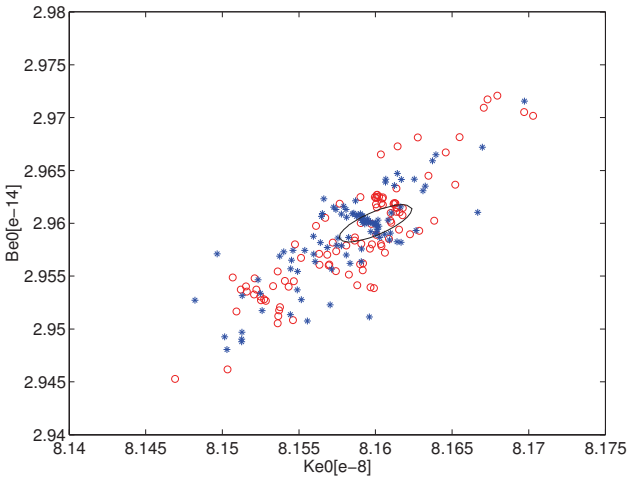

Figure 4.9: Bootstrap estimates for the designed dynamic multi-component gas experiment with 10% noise: red O are the results of the LDM optimizer while blue * are the results of the hybrid optimizer, the green ellipse shows the 99.9% CI by FIM

4.1.11 Conclusion and discussion

In this section we considered the parameter identification problem for a homogeneous ceramic porous membrane. Several different experimental schemes are compared and discussed on the basis of a realistic membrane reactor model. Optimal experimental designs are carried out for the different schemes.

The performances of the experimental schemes are then compared at their corresponding optimal experimental conditions. The Cramér-Rao inequality is used as the basic criterion

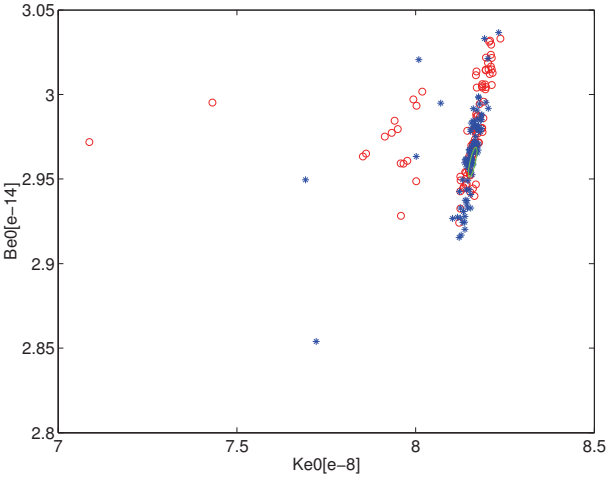

Figure 4.10: Bootstrap estimates for the designed dynamic multi-component gas experiment with 50% noise: red O are the results of LDM optimizer while blue * are the results of the hybrid optimizer, the green ellipse shows the 99.9% CI by FIM

for this comparison. The results show that the *efficiency* of the tested experimental schemes has approximately the following order: multi-component gas dynamic>multi-component gas steady≈ single-gas dynamic>transient diffusion > single-gas steady > isobaric diffusion.

However, the Cramér-Rao bound only gives us the lower boundary of the variances of parameters for linear systems. For nonlinear systems the variances of the estimated parameters may be much bigger than prediction of Cramér-Rao bound. In the second part of this section, a bootstrap analysis is applied to get the *real* probability distributions of

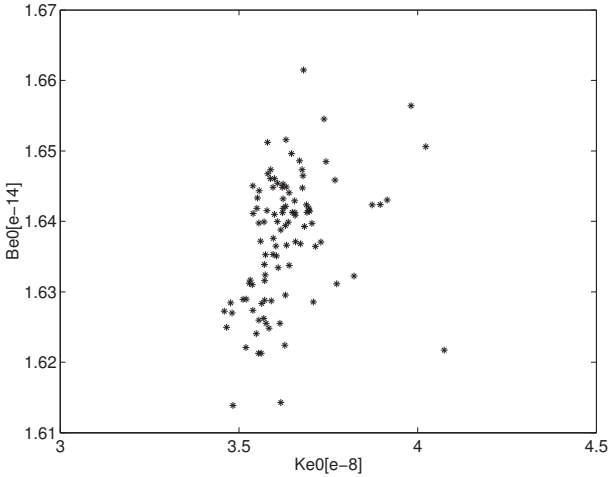

Figure 4.11: Bootstrap estimates for the designed dynamic multi-component gas experiment with 10% noise: the LDM optimizer starting with 50% deviation in the parameter values

the estimated parameters for dynamic multi-component gas experiments. Bootstrap results show much bigger real variances for the estimated parameters. However, the effectiveness of the bootstrap method is strongly depending on the character of the optimizer. Since there is not yet an efficient deterministic global optimizer available, some stochastic, local, or hybrid (stochastic local) methods must be used instead. The consequence is, that new uncertainties from the optimizer also get into the variances of estimated parameters. In this case as we discussed, the standard deviation of parameters predicted by both optimizers are close to each other but far from the Cramér-Rao prediction, which may imply the results of bootstrap method are more close to the *real* standard deviation.

Intuitively, one would expect that the CI of hybrid optimizer is broader than the CI of the LDM optimizer, since a ”local” optimizer is more easily caught by some local minimum and stays close to the initial values. This assumption coincides with the comparison of optimization results. However, from figure 4.10 one also notices that the appearance of extreme values of the ld optimizer are more frequent than for the hybrid optimizer. A possible explanation is that the LDM optimizer sometimes accidentally falls into some other attractive region (because of the noise changing the shape of the cost function) and thus converges to some *far away* local minimum. In this model, these two effects seem to compensate for each other, so one by luck gets an ”approximately correct” CI from the LDM optimizer (although with wrong probability distribution). As discussed before, the LDM optimizer is superior to the hybrid optimizer in terms of computation time, therefore the ld optimizer could be a substitute for the hybrid optimizer when working with a approximately linear model and computation time becomes an important factor (e.g. when solving a partial differential model with finite-element-method, or when an analysis with large number of bootstrap samples is necessary).

In this section, the experimental design is still based on the traditional way - minimization of e-criteria of FIM. The direct application of bootstrap CI to design new experiments is still time forbidden, even with the relative faster ld optimizer. Firstly, to get a ”stable” CI, a big number of bootstrap replication is necessary, secondly, the time consuming hybrid optimizer is also necessary for the optimization of control parameters. Since for a dynamic system, the control parameters of piece-wise constant feeding profile are usually highly correlated and highly non-linear, it’s not beneficial to use the LDM optimizer also in the experimental design part. It could be possible to test the ”bootstrap OED” in some small benchmark models, but that’s beyond the focus of this work.

4.2 Mass transport through multi-layer membrane

In section 4.1, we discussed different reaction schemes for the identification of a homogeneous membrane. In reality, many porous membranes are composed of several layers. The most common reason is that the *selective layer* of the membrane is not physically strong enough and must adhere to a thick "support layer" [45]. Furthermore some recent research shows that a composite membrane may have some other potential advantage comparing to homogeneous membrane, such as to influence the gas transport direction [3], or to choose permeability for different gases. The best way to identify a multi-layer membrane is to perform identification layer by layer, so that K_0 and B_0 could be precisely identified for each layer. However, this method is feasible only when all the precursors of the membrane are available [13]. When the precursors are not available, or even when one has no idea about whether the membrane in hand is homogeneous or composite, an alternative way must be performed to identify transport coefficients for all layers simultaneously. Two questions naturally arise:

1. Is the multi-layer membrane model structurally identifiable?
2. Is it possible to get the parameters within a certain precision, under the noisy measurement condition?

As a matter of fact, these questions should be answered before estimations of parameters of a real membrane. In this work, instead of a thorough mathematical analysis of the global identifiability of multi-layer membranes, we first study an example of an ideal membrane reactor with the same structure as a real metallic membrane. If the Fisher information matrix of the model is non-zero, the model should have at least local identifiability, and if the estimated parameters of a global optimization converge to a set of single point, one can assume the model is globally identifiable. It's reasonable to generalize this conclusion

to other membrane with the same model structure and similar transport parameters. The identification results and problems of a real metallic membrane is presented in section 4.2.2, and possible experimental design is advised.

4.2.1 Identification of an ideal two-layer membrane

In this section an *ideal* two-layer membrane model is investigated to discuss the identifiability of multi-layer membrane model. The selection of *ideal* two-layer membrane is based on the following intuitive assumptions:

1. The total permeability of each layer of the membrane should be similar.
2. The bulk diffusion and Knudsen diffusion effects for the same layer should also be similar.
3. The Knudsen diffusion and bulk diffusion effects for different layers should vary as much as possible.
4. Both bulk diffusion and Knudsen diffusion coefficients should be within physical realistic range.

All the above criteria in mind, we set a group of parameters for the ideal two-layer membrane as in table 4.14.

Table 4.14: Parameters set of an ideal two-layer membrane

Parameter	$\ln K_{01}$	$\ln B_{01}$	$\ln K_{02}$	$\ln B_{02}$
Value	-15	-32	-16	-31

Notice that the above parameters are reparametrized to be logarithmic value of the respective original viscous flow and Knudsen flow coefficients, and all the other physical

parameters of the membrane are set to be the same as the real metallic membrane in section 4.2.2.

In the following sections we discuss two experimental schemes and corresponding experimental design and parameter identification problems. The first scheme is the steady state multi single-gas permeation experiment, since it's the most commonly used method for transport coefficient identification. The second is a dynamic gas transport experiment because it has the best performance in all the experimental schemes we discussed in section 4.1.

Model for multi single-gas permeation through multi-layer membrane

When modeling the single gas permeation through a multi-layer membrane, the equation 2.21 can be further simplified as follow:

$$\frac{\dot{N}_j}{\Delta P_i} = -\frac{2\pi L}{\tilde{R}T \ln\left(\frac{r_{m,i+1}}{r_{m,i}}\right)} \left(\frac{4}{3} K_{0,i} \sqrt{\frac{8\tilde{R}T}{\pi \tilde{M}_j}} + \frac{B_{0,i}}{\eta_j} \overline{P_i}\right) \tag{4.10}$$

where:

$$\sum_{i=1}^{n} \Delta P_i = P_A - P_B \tag{4.11}$$

$$\overline{P_i} = \frac{P_{in,i} + P_{in,i+1}}{2} \tag{4.12}$$

for i=1,2,. . . ,n

and:

$$P_{in,1} = P_A \tag{4.13}$$

$$P_{in,n+1} = P_B \tag{4.14}$$

Here, n stands for the total number of layers, and $P_{in,i}$ represents the pressure inside membrane layers. The situation for a two-layers membrane is described in Figure 4.12. For each set of P_A and P_B a mass flow rate $\dot{N}_j$ will be calculated by solving a group of nonlinear equations. Obviously the identification of the multi-layer membrane is a much more difficult problem, since the number of observation is still the same but the number of parameters to be identified increases to n times the value before. Furthermore, the parameters of the model are highly linearly correlated and the optimization problem is highly non-convex. Therefore the selection of the optimizer becomes the most difficult problem in the identification task. Definitely a local deterministic optimizer is not applicable because of the existence of local minima. Also a traditional genetic algorithm becomes very slow because of the high linear correlation of the parameters. The genetic algorithm has to be modified to increase the efficiency of the optimizer. In chapter 3 a modified genetic algorithm is discussed. However, even with the improved GA, still much computation time is required for identification problems, especially when the bootstrap method is performed to calculate the confidence interval of the estimated parameters.

Steady state single gas permeation experiment

The only difference of this experimental scheme of this section in comparison to section 4.1 is that the pressure on both sides of the membrane is assumed to be controlled directly and precisely. In addition the temperature of the membrane is used as another controlled experimental condition, while the temperature of both chambers and gas are assumed to be

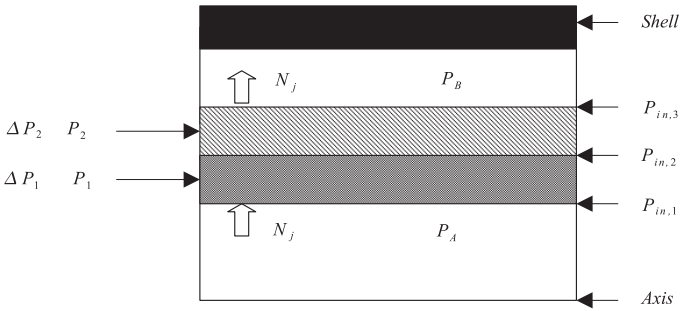

Figure 4.12: Sectional view for model of double layer membrane reactor

the same as membrane. The kind of gas is used as the third condition for OED of steady gas permeation experiments.

As described in section 4.1, firstly an optimal experimental design should be performed to locate the optimal experimental conditions.

During the experimental design, the pressure for both sides of the membrane is limited between 1.5 bar and 3 bar, with 0.1 bar interval. The temperature is limited between 100 and 500 centigrade with 100 centigrade interval. And the gas is chosen from nitrogen, helium and argon (although the OED result shows only helium and argon is necessary). Therefore, the total possible combination of experimental condition is $u_{total} = 16 \times 16 \times 5 \times 3 = 3840$.

A factorial experimental design will compose all of the above possible conditions, but by optimal experimental design it's possible to perform much less experiments. For OED of n experiments there are possible combination of u_{total}^{n}. The calculation of sensitivities and Fisher information matrix was described in section 3.1.3, and the e-criterion is again used as objective. The results of OED for 10 and 20 experiments are listed in table 4.15 and 4.16, where the corresponding e-criteria are -22.3580 and -45.0967(for 1% noise). Apparently when the number of experiments goes beyond 10 the e-criteria of the FIM (and the standard deviation of the estimated parameters) increases almost linearly, which could also be achieved by simply repeating the same group of experiments. Furthermore, it's easy to see that most of the experiments in table 4.16 already appeared in table 4.15. Therefore in the following part we choose only the OED results of 10 experiments for identification. The full Fisher information matrix (FIM) of the OED result is listed in table 4.17, while the inverse of FIM as the Cramér-Rao boundary is listed in table 4.18.

Table 4.15: Results of optimal experimental design for 10 experiments

Exp. Number	P_A [bar]	P_B[bar]	Gas	Temperature[^{o} C]
1	1.5	3.0	He	300
2	3.0	1.5	He	500
3	1.5	3.0	He	300
4	3.0	1.5	Ar	100
5	1.5	3.0	Ar	200
6	1.5	3.0	Ar	200
7	1.5	3.0	He	300
8	3.0	1.5	Ar	100
9	3.0	1.5	He	500
10	1.5	3.0	Ar	200

The nonsingular FIM proves the local identifiability of the model, but is not sufficient to prove global identifiability. Furthermore the estimation of the confidence interval of the

Table 4.16: Results of optimal experimental design for 20 experiments

Exp. Number	P_A [bar]	P_B[bar]	Gas	Temperature[^{o} C]
1	3.0	1.5	He	500
2	1.5	3.0	He	300
3	1.5	3.0	Ar	200
4	1.5	3.0	Ar	200
5	3.0	1.5	Ar	100
6	1.5	3.0	Ar	200
7	3.0	1.5	He	500
8	1.5	3.0	He	300
9	1.5	3.0	He	300
10	1.5	3.0	He	300
11	3.0	1.5	He	500
12	1.5	3.0	Ar	200
13	1.5	3.0	Ar	200
14	3.0	1.5	He	500
15	3.0	1.5	Ar	100
16	1.5	3.0	He	300
17	1.5	3.0	He	300
18	3.0	1.5	Ar	100
19	1.5	3.0	Ar	200
20	1.5	3.0	He	300

Table 4.17: FIM of designed 10 experiments

FIM	K_{01}	B_{01}	K_{02}	B_{02}
K_{01}	12772.21765	5497.66348	5872.83972	11367.57387
B_{01}	5497.66348	4178.81099	1432.80404	5400.26835
K_{02}	5872.83972	1432.80404	3909.46671	4842.78813
B_{02}	11367.57387	5400.26835	4842.78813	10311.49492

parameters by FIM is sometimes not accurate, as we discussed in section 4.1. The more realistic but also more time-consuming way is to perform a bootstrap identification and

Table 4.18: Estimated covariance (by FIM) of designed 10 experiments

Covariance	K_{01}	B_{01}	K_{02}	B_{02}
K_{01}	0.01961	0.00308	-0.00433	-0.02121
B_{01}	0.00308	0.00214	0.00043	-0.00472
K_{02}	-0.00433	0.00043	0.00232	0.00345
B_{02}	-0.02121	-0.00472	0.00345	0.02433

calculate the confidence interval from the statistics of estimated parameters. However, the optimization task becomes more difficult and requires much more computation time now since the number of parameters to be identified increases to four. The traditional genetic algorithm is modified to increase the efficiency and precision of the optimization, see chapter 3. However even with improved GA, a single identification task may take from several hours to several days, depending on the initial population size of the optimizer. And still the variance caused by the stochastic nature of the optimizer cannot be totally avoided.

To calculate the real parameter variance caused by measurement noise, one possible way is to simply exclude the variance caused by the optimizer.

Suppose there exists a *ideal* global optimizer that can always locate the minimum of the objective function and there exists only one global optimum of the objective function, then the parameter estimated by this optimizer for a single sample of the bootstrap analysis can be expressed as $\hat{\theta}_s^*$. The parameter estimated by GA $\hat{\theta}_s$ is stochastic, and therefore by itself a random variable (notice that $\hat{\theta}_s^*$ is a single constant value). Suppose the GA estimator is unbiased, i.e. $E(\hat{\theta}_s) = \hat{\theta}_s^*$, then the difference of optimization results between GA and *perfect* global optimizer is $d_{GA,s} = \hat{\theta}_s^* - \hat{\theta}_s$. If d_{GA_s} is constant for all bootstrap samples, i.e. $d_{GA} = d_{GA,s}$ then the estimated parameters for each bootstrap sample can be expressed as: $\hat{\theta} = \hat{\theta}^* + d_{GA}$. When there's no correlation between $\hat{\theta}^*$ and d_{GA}, the variance of estimations is: $V(\hat{\theta}) = V(\hat{\theta}^*) + V(d_{GA}) = V(\hat{\theta}^*) + V(\hat{\theta}_s)$. Then the *true* variance caused by the

measurement noise can be calculated by: $V(\hat{\theta}^*) = V(\hat{\theta}) - V(\hat{\theta}_s)$. For multiple parameter estimation problems, it could also be proved that: $Cov(\hat{\theta}^*) = Cov(\hat{\theta}) - Cov(\hat{\theta}_s)$. Note that here $\hat{\theta}$ is the vector of estimated parameters.
The procedure for confidence interval estimation is summarized as below:

1. Perform bootstrap identification with zero noise, and calculate the covariance matrix $Cov(\hat{\theta}_s)$ from the samples of identified parameters.

2. Apply an additional Gaussian distributed white noise and perform bootstrap identification again with the *noisy measurements*. the covariance matrix $Cov(\hat{\theta})$ is calculated from samples of estimated parameters.

3. The estimation of *real* covariance of the parameters is calculated by: $Cov(\hat{\theta}) - Cov(\hat{\theta}_s)$

The procedure is based on the following assumptions:

1. The covariance of optimization results for each bootstrap sample point is the same.

2. There exists no correlation between $\hat{\theta}^*$ and $\hat{\theta}_s$.

3. The estimator $\hat{\theta}$ has no bias, and is distributed around $\hat{\theta}^*$.

4. There's only one global optimum for $\hat{\theta}^*$.

The performance of GA is strongly dependent on the size of initial population and maximal evolution steps [34], as the size and steps increase $\hat{\theta}_s \rightarrow \hat{\theta}_s^*$ and $d_{GA,s} \rightarrow 0$. Too small initial population size makes the optimizer easy to converge to some local minimum far away from the local minimum and thus makes the CI analysis meaningless, while too big population size apparently makes the bootstrap analysis too time consuming. The compromise between preciseness and efficiency is made totally based on experiences. In this work we

choose initial population size of 1000 and step limit of 50. The GA with coordinate transform is used as described in chapter 3, where also other parameter settings of GA can be found. Bootstrap identification are performed with noise level at zero and 1%, with B=50, note that the objective function used here is:

$$J = \ln[\sum_i \frac{(\dot{N}_i - \dot{N}_{i,m})^2}{\dot{N}_{i,m}^2} + 10^{-6}], \tag{4.15}$$

(A small constant is used to prevent zero in logarithmic function) The calculated covariance of the parameters with zero and one percent noise of measurements are listed in table 4.20 and 4.19 respectively.

Table 4.19: Bootstrap covariance matrix without noise

Covariance	K_{01}	B_{01}	K_{02}	B_{02}
K_{01}	2.50e-03	4.37e-04	-4.92e-04	-2.74e-03
B_{01}	4.37e-04	1.32e-04	-5.20e-05	-5.27e-04
K_{02}	-4.92e-04	-5.20e-05	1.38e-04	5.05e-04
B_{02}	-2.74e-03	-5.27e-04	5.05e-04	3.07e-03

Table 4.20: Bootstrap covariance matrix with 1% noise

Covariance	K_{01}	B_{01}	K_{02}	B_{02}
K_{01}	2.25e-02	3.09e-03	-6.15e-03	-2.54e-02
B_{01}	3.09e-03	2.56e-03	3.62e-04	-5.14e-03
K_{02}	-6.15e-03	3.62e-04	3.03e-03	5.82e-03
B_{02}	-2.54e-02	-5.14e-03	5.82e-03	3.07e-02

The *real* covariance matrix, which is the difference of the above two covariance matrix, is

in table 4.21. It could be seen that for this small noise level, it's very close to the prediction of FIM. The confidence interval analysis also proves the existence of a unique global optimum, part of the identification results can be seen in table 4.22.

Table 4.21: Covariance matrix of an ideal global optimizer

Covariance	K_{01}	B_{01}	K_{02}	B_{02}
K_{01}	2.00e-02	2.66e-03	-5.66e-03	-2.27e-02
B_{01}	2.66e-03	2.43e-03	4.14e-04	-4.61e-03
K_{02}	-5.66e-03	4.14e-04	2.89e-03	5.31e-03
B_{02}	-2.27e-02	-4.61e-03	5.31e-03	2.76e-02

Table 4.22: Bootstrap identification results of an ideal global optimizer

K_{01}	B_{01}	K_{02}	B_{02}	Obj
-1.51e+01	-3.21e+01	-1.61e+01	-3.09e+01	-8.19e+00
-1.49e+01	-3.19e+01	-1.60e+01	-3.12e+01	-7.71e+00
-1.54e+01	-3.21e+01	-1.59e+01	-3.04e+01	-6.76e+00
-1.49e+01	-3.20e+01	-1.60e+01	-3.11e+01	-7.49e+00
-1.51e+01	-3.21e+01	-1.60e+01	-3.09e+01	-6.82e+00
-1.51e+01	-3.20e+01	-1.60e+01	-3.09e+01	-6.84e+00
-1.53e+01	-3.20e+01	-1.59e+01	-3.06e+01	-7.60e+00
-1.50e+01	-3.21e+01	-1.60e+01	-3.10e+01	-7.46e+00
-1.51e+01	-3.21e+01	-1.61e+01	-3.08e+01	-8.21e+00
-1.50e+01	-3.20e+01	-1.60e+01	-3.10e+01	-7.25e+00
...				

Dynamic gas transport experiment

The dynamic gas transport experiments are performed as described in section 4.1.7, where also all the settings and condition limits can be found. The model for gas transport is given

in section 2.2.4. After the routine experimental design step, the optimal feeding profile is obtained as in figure 4.13. In the next step, the bootstrap method is applied to get the covariance matrix of estimated parameters. The results of bootstrap is given in tabular 4.23. As expected, the dynamic gas transport experiments enable much more precise parameter estimations. Furthermore, this kind of experimental scheme also make the GA optimizer converge faster during parameter identification process.

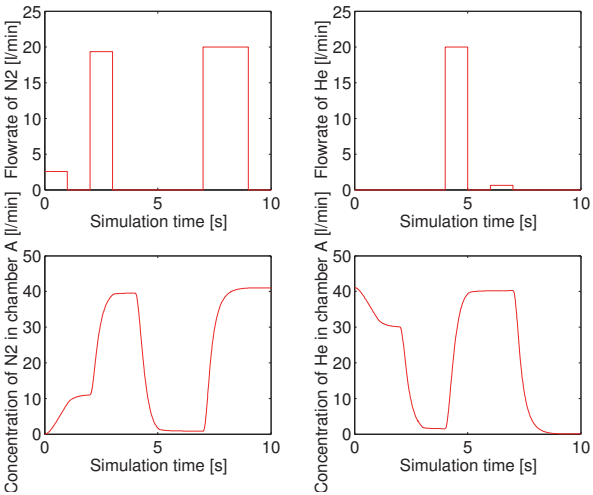

Figure 4.13: Designed feeding profile and corresponding concentration for both gas in chamber A

However, it should be noted that the model of dynamic gas transport experiment only considers the ideal case with a lot of simplifications. The two chambers of the membrane

Table 4.23: Bootstrap identification results with 1% noise

Covariance	K_{01}	B_{01}	K_{02}	B_{02}
K_{01}	1.42e-03	1.12e-03	-6.69e-04	-1.59e-03
B_{01}	1.12e-03	1.26e-03	-6.30e-04	-1.30e-03
K_{02}	-6.69e-04	-6.30e-04	3.51e-04	7.65e-04
B_{02}	-1.59e-03	-1.30e-03	7.65e-04	1.80e-03

reactor are considered to be homogeneous, but in reality there will be axial and radius concentration gradients. For more detailed model of dynamic gas transport experiment, the gradients of concentration and the dispersion effects must also be described in the model, therefore the model may become too big and time demanding for parameter identification. Another problem is that the inlet flow rate of the gas cannot be controlled precisely in reality, and may introduce more uncertainties in parameter estimation. The advantage of dynamic gas transport experiment still needs to be proved by real experiments.

4.2.2 Case study: identification of two-layer metallic membrane

The problem of this section is to identify the gas transport parameters of a real metallic membrane. The geometry of the membrane is summarized in table 4.24. From the observation of a broken metallic membrane, it appears to be composed of two layers with similar thickness, see figure 4.14. But without producer information, this assumption has to be verified by gas transport experiments.

Table 4.24: Physical scale of the metallic membrane reactor

Total length[mm]	Effective length[mm]	Inner radius[mm]	Outer radius [mm]
250	120	10.55	12.8

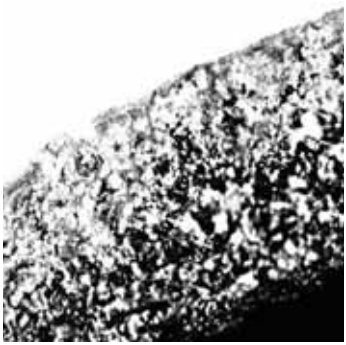

Figure 4.14: Sectional graph of the broken metallic membrane

Steady gas permeation experiments are carried out by V. Edreva and E. Tsotsas with the experimental setup described in reference [13]. Since the prior information of the gas transport parameters is not available, a complete factorial experiment is performed with two different kinds of gas, two different flow directions (with a constant flow rate), five different temperatures and five different pressures. Therefore totally 100 experiments are performed. Firstly the membrane is assumed to be homogeneous, and the Knudsen diffusion coefficient and bulk flow coefficient are easily calculated as in table 4.25. The relative standard deviation of the measurements is calculated by:

$$\sigma_r = \sqrt{\frac{\sum_i \frac{(\dot{N}_i - \dot{N}_{i,m})^2}{\dot{N}_{i,m}^2}}{m-k}} \tag{4.16}$$

Where k is the number of model parameters [46].

Table 4.25: Identification result for homogeneous model

$\ln K_0$	K_0	$\ln B_0$	B_0	Objective	σ_r
-15.737	1.464e-7	-31.105	3.099e-14	-2.741	2.57%

Note that the actually identified parameters are in fact logarithms of the real transport coefficients, and the cost function is:

$$J = \ln \sum_i (\frac{\dot{N}_i - \dot{N}_{i,m}}{\dot{N}_i})^2, \tag{4.17}$$

In the next step, the same set of experimental data is used to identify a two-layer model. It's reasonable to assume that the two layers have relatively similar structure and transport coefficients (otherwise it's difficult to adhere to each other), and the coefficients for both layer should be around the identified parameters of the homogeneous model. Therefore, the search region for K_0 and B_0 for each layer are limited to $K_0 \in [-33 - 28]$ and $B_0 \in [-17 - 15]$. To minimize the stochastic uncertainty of GA, the same identification process is repeated for 100 times and the optimum solution is found as in table 4.26

As expected, the two layer model shows a better fit for the experimental data. However, due to the stochastic nature of GA, the identified parameters show big variances for each identification process, part of the identification results can be seen in table 4.27. The experimental data and parameters of GA are the same for all the identification processes, and therefore the variances are totally caused by GA.

Table 4.26: Identification result for two-layer model

$\ln K_{01}$	$\ln B_{01}$	$\ln K_{02}$	$\ln B_{02}$	Objective	σ_r
-15.97	-30.04	-15.83	-31.75	-3.332	1.93%

Table 4.27: Identification results of two-layer membrane

$\ln K_{01}$	$\ln B_{01}$	$\ln K_{02}$	$\ln B_{02}$	Objective
-1.6022e+01	-2.9453e+01	-1.6029e+01	-3.1811e+01	-3.3242e+00
-1.6081e+01	-3.0586e+01	-1.5485e+01	-3.1625e+01	-3.3239e+00
-1.5955e+01	-2.9448e+01	-1.6041e+01	-3.1802e+01	-3.3255e+00
-1.5487e+01	-3.1578e+01	-1.6151e+01	-3.0546e+01	-3.3212e+00
-1.6089e+01	-3.1747e+01	-1.7100e+01	-2.8838e+01	-3.3047e+00
-1.5999e+01	-2.9002e+01	-1.6156e+01	-3.1816e+01	-3.2983e+00
-1.7991e+01	-2.8379e+01	-1.6250e+01	-3.1830e+01	-3.2613e+00
-1.6145e+01	-3.0738e+01	-1.5323e+01	-3.1589e+01	-3.3212e+00
-1.5961e+01	-2.9995e+01	-1.5845e+01	-3.1753e+01	-3.3321e+00
-1.5949e+01	-2.9745e+01	-1.5944e+01	-3.1782e+01	-3.3308e+00
-1.5890e+01	-3.1700e+01	-1.6031e+01	-2.9734e+01	-3.3292e+00
-1.5942e+01	-3.1716e+01	-1.6083e+01	-2.9548e+01	-3.3274e+00
...				

The histogram for each parameter is plotted in figure 4.15. While the histograms of Ke01 and Ke02 are almost around some certain value, the histograms of Be01 and Be02 are distributed in two separate groups. It's more clear to see the plot of Ke01 vs Ke02 in figure 4.16, apparently the optima are composed of two disconnected regions. The reason for this behaviour may be that it is possible to identify the properties of the two layers from the given experimental data, but not their sequence. In such situation, neither FIM or bootstrap method can be applied to calculate the confidence interval of the identified parameters correctly, and some further experiments should be designed and performed to

find the real parameter region. However, it's possible to prove all of the results in table 4.27 are valid possible values of parameters. Suppose the noise level for each measurement is independent and constant with a relative standard deviation of 1.93%, as is calculated in table 4.26, then:

$$\sum_i \frac{(N_i - N_{i,m})^2}{(N_{i,m}\sigma_r)^2} \sim \chi^2_{dm-dp} \tag{4.18}$$

It can be calculated that each identification result with objective below -3.1078 is within the 95% confidence interval. Therefore all the identification results for two-layer model lie in the confidence interval, and the single-layer model can be excluded(see table 4.25).

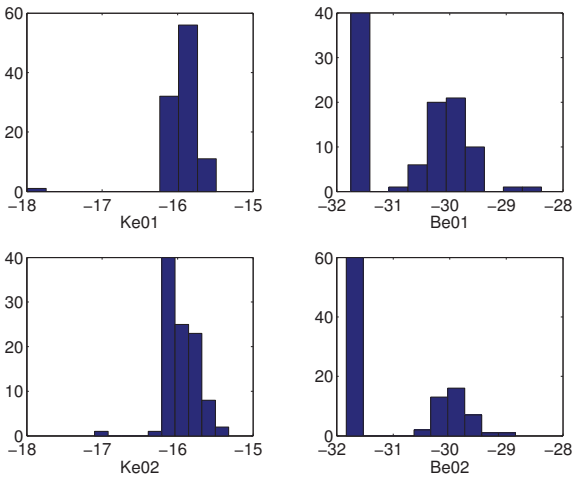

Figure 4.15: Histogram for the identified parameters of the two-layer model

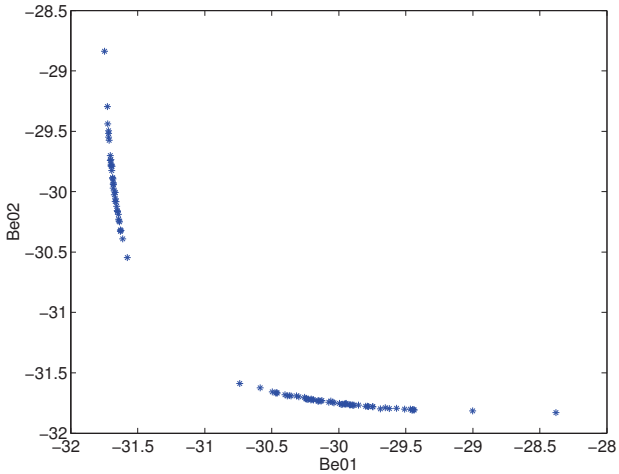

Figure 4.16: Identification results of B01 and Be02 of two-layer model

In this example, experimental design has two different considerations:

1. To increase the global identifiability by distinguishing between the two disconnected optimal regions (i.e. the correct sequence of the two layers).

2. To increase the local identifiability for each possible set of parameters.

For the first consideration, two representative sets of parameters are chosen from the two separate optimal regions, see table 4.28, and the *distance* between the corresponding observations is maximized.

$$J1 = \sum_i \frac{(N_{i,1} - N_{i,2})^2}{(N_{i,1}\sigma_r)^2} \tag{4.19}$$

In equation 4.19 $N_{i,1}$ denotes the fluxes for the first set of parameters in the first line of table 4.28, and $N_{i,2}$ denotes the fluxes for the second set of parameters.

During the preliminary factorial experiments, the pressure difference between the two chambers of membrane reactor is always limited below 0.1 bar. However, by experimental design, it is found that the increase of pressure difference (and also the flow rate) can greatly increase the identifiability of the two-layer model. In table 4.29, the limit of maximal pressure difference increases from 0.1 bar to 0.5 bar linearly. The design results show that the optimal experimental conditions always have maximal pressure difference, and when the noise is Gaussian distributed at least 0.5 bar pressure difference is needed to distinguish the two groups of parameters with 95% confidence level by a single experiment.

Table 4.28: Representative parameters for two optimal region

$\ln K_{01}$	$\ln B_{01}$	$\ln K_{02}$	$\ln B_{02}$
-15.97	-30.04	-15.83	-31.75
-15.84	-31.69	-16.04	-29.88

Another approach is to calculate FIM for all possible set of parameters, and minimize the sum of some criteria. Thus the *global* local identifiability of the model is increased. The identified parameters in table 4.27 are good representative for all possible combinations of parameters within confidence interval. But for efficiency consideration still only the two representation sets of parameters in table 4.28 are used for experimental design. The OED is performed to minimize the sum of e-criteria of the FIM of two group of parameters, and OED results of 10 experiments is in table 4.30.

Table 4.29: Experimental design results

Exp.	P_A [bar]	P_B[bar]	Gas	Temperature[^{o} C]	Objective $J1$
1	1.5	1.6	He	500	0.5025
2	1.5	1.3	He	500	1.795
3	1.5	1.2	He	500	4.535
4	1.5	1.1	He	300	8.9307
5	1.5	1.0	He	300	15.5428

Table 4.30: Experimental design results

Exp.	P_A [bar]	P_B[bar]	Gas	Temperature[^{o} C]
0	1.6	1.1	Ar	200
1	2.0	1.5	He	300
2	1.5	2.0	Ar	200
3	1.5	1.0	He	500
4	1.6	2.1	He	100
5	1.5	2.0	Ar	300
6	1.6	1.1	Ar	200
7	2.4	2.9	Ar	100
8	1.5	1.0	Ar	100
9	1.8	1.4	He	300

4.2.3 Thickness of the membrane layers

Except for the gas transport coefficients, one may also want to identify the thickness of each membrane layer simultaneously. However, generally such approach is not going to succeed. Consider equation 4.10 again, the radius of each layer is fully correlated with the gas transport coefficients K_{0i} and B_{0i}, and therefore cannot be identified separately. The effect of increasing or decreasing the thickness of the layers can be compensated by increasing or decreasing the transport coefficients proportionally.

The thickness of the membrane is only identifiable when it has other effects on the membrane behavior except for the transport phenomenon. For example, when the membrane process a non-negligible hold-up or dynamic adsorption effects have to be taken into account, the volume of the membrane will influence the dynamic behavior of gas transport. One model considering the hold-up effect of the membrane is implemented as depicted in figure 4.17. The simulation results of the metallic membrane are compared with the original model, but no apparent difference is observed. The metallic membrane is too thin (2.45mm) to show any apparent hold-up effects, therefore the identification problem is not considered.

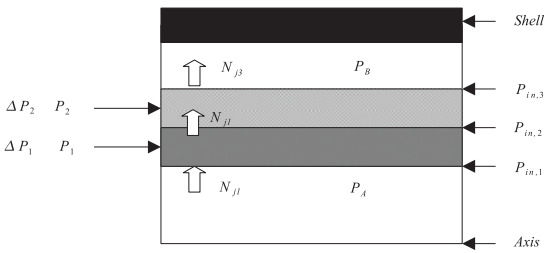

Figure 4.17: Model of the multilayer membrane with hold-up, each layer is considered to be a small chamber, and dusty gas model is applied to describe the gas transport between adjacent chambers. Note that the gas flow rate N_j now is different for each layer.

4.2.4 Conclusion and discussion

In this section we discussed the possibility of identification of multi-layer membranes. Firstly the steady gas permeation experiments are discussed. After a successful OED, the existence of a non-singular FIM proves the local identifiability of the model. In the next step, a bootstrap method is performed, and proves the global identifiability. Since the randomness can not be totally eliminated, a method for estimation of the *real* bootstrap confidence interval is advised. However, the method is still limited and cannot be applied to optimization problems with disconnect optimal regions, such as the practical case study in section 4.2.2.

The dynamic multi-component gas transport experimental scheme is also examined for identification of the two-layer membrane model. As discussed in section 4.1, this experimental scheme shows much higher efficiency and much narrower confidence interval of estimated parameters. Although the control and measure of dynamic experiments could also be more difficult, it may still be a competitive experimental scheme and should be investigated when conditions permit.

In the practical study of identification a metallic membrane, more realistic problems are discussed. Although the identification results for two-layer model are superior to the results of the homogeneous model, the confidence interval it is too broad to determine the precise values of the transport coefficients for both layers. The identification results also show that there exists two disconnected optimal regions. Therefore, the experimental design is performed in two different approaches: firstly some experiments are designed to distinguish between the two optimal regions, and secondly some OED are performed to increase the local identifiability. For both approaches, only two representative parameter sets, which are the optimal results for the corresponding optimal regions, are used in order to save the computation time.

During the OED process, it's found that the pressure difference has an important effect in identification of the two-layer membrane model. In all discussed experimental designs the highest pressure difference is always selected. In the identification of a real metallic membrane, the existence of two disconnected optimal region is also possibly a consequence of insufficient pressure difference. In fact, by observation of the two representative parameter sets, it's easy to notice that they are almost the same by exchanging the turn of two layers. For steady gas permeation experiments, without big enough pressure gradients inside the membrane, it's difficult to determine the order of the different layers of the membrane.

Chapter 5

Spatiotemporal patterns in membrane reactors

5.1 Introduction

After the model selection and the parameter fitting step, the identified model can be used for process simulation, process analysis and finally process optimization and model predictive control. This chapter is focused on the process simulation and analysis of a special kind of nonlinear phenomena - the formation of spatiotemporal patterns, especially the stationary spatially patterns within a membrane reactor. The simulation starts firstly with a simple membrane reactor model, then the results are extended to and verified by a detailed model reactor model where both the experimentally identified reaction kinetics and mass transfer coefficients are incorporated. The final results show that it's possible to observe the pattern in a laboratory reactor under feasible operation conditions.

The nonlinear dynamics of CSTR system have been investigated extensively for a long time [47, 48, 17]. The instability may be caused by either interaction of reaction kinetics or by

interaction of mass and enthalpy balance. Sheintuch first pointed out the analogy between the membrane reactor and the CSTR [14, 16], see figure 5.1. Unter certain circumstances, the temporal behavior of a CSTR could be used to describe and classify the stationary spacial behavior of a membrane reactor.

The analogy can be simply explained by considering single exothermic reaction: $A \rightarrow B$. The mass balance and energy balance for such a reaction in a CSTR can be described as follows:

$$\frac{dc}{dt} = -r + \frac{\dot{q}_{in}}{V}(c_0 - c) \tag{5.1}$$

$$\rho C_p \frac{dT}{dt} = -\Delta H r + \frac{\dot{q}_{in}}{V}\rho C_P(T_{in} - T) + \frac{\alpha A}{V}(T_0 - T) \tag{5.2}$$

Where c and c_0 are the concentration of A in the CSTR and the feeding concentration of A, T , T_{in} and T_0 are the temperature of CSTR, feeding and reactor wall, $\dot{q}_{in}$ and V represent the feeding flow rate and volume of the reactor. Under the assumption that the temperature of the feeding and the reactor wall are the same, the equations could be simplified as follows:

$$\frac{dc}{dt} = -r + \beta(c_0 - c) \tag{5.3}$$

$$\rho C_p \frac{dT}{dt} = -\Delta H r + \alpha^*(T_0 - T) \tag{5.4}$$

where $\beta = \frac{\dot{q}_{in}}{V}$ and $\alpha^* = \frac{\dot{q}_{in}}{V}\rho C_P + \frac{\alpha A}{V}$

It's well known that in certain parameter space such a system shows various bifurcations and nonlinear behavior [17, 18]. Now suppose the same reaction is carried out in a tubular fixed bed membrane reactor. By assuming a constant annulus side and using a simplified membrane model, the mass balance and energy balance of the fixed side as described in

equation 2.6 and 2.7 should be rewritten as:

$$\frac{\partial c}{\partial t} + u\frac{\partial c}{\partial z} = r + \beta^*(c_0 - c) \tag{5.5}$$

$$(\rho C_p)_{tot}\frac{\partial T}{\partial t} + u(\rho C_p)_f\frac{\partial T}{\partial z} = -\Delta H r + \lambda\frac{\partial^2 T}{\partial z^2} + \alpha^*(T_0 - T) \tag{5.6}$$

Here $\beta^* = \frac{2}{r_{mem,in}}\beta$, $\alpha^* = \frac{2}{r_{mem,in}}\alpha_{mem}$, see figure 5.1-b. It's easy to notice that if the heat dispersion term in equation 5.6 is very small and could be ignored, and the concentration and temperature in the membrane reactor reaches steady state, then the spatial pattern of the membrane reactor is identical to the temporal dynamics of the CSTR. Therefore the solution of the CSTR could be used as the basis to study the steady state solution of membrane reactor, and the influence of heat dispersion coefficient could be considered afterwards. It is well known that the dynamic behavior of exothermic CSTR may be very complex and show periodic and aperiodic solutions [17]. Due to the analogy between membrane reactor and CSTR, a spatial pattern formation can be expected in membrane reactors.

Figure 5.2 gives a more intuitive physical explanation for the formation of stationary pattern within a membrane reactor. The fluid flowing through the fixed bed possesses a storage capacity for material of reactants and for heat. A spatial pattern is caused by the alternate charging and discharging of the material storage and the heat storage resulting from the chemical reaction. In sections of high conversion, the material storage is discharged, and the reaction heat released charges the energy storage. In sections of low conversion, the material storage is reloaded by mass transfer from the sweep gas side through the membrane, while heat losses reduce the temperature of the fixed bed and hence discharge the energy storage.

In the next step, first the simple membrane reactor model as described in figure 5.1-b is used for bifurcation analysis. The analysis results are then applied to a more detailed membrane reactors as described in figure 2.2. The detailed membrane reactor model consists of three

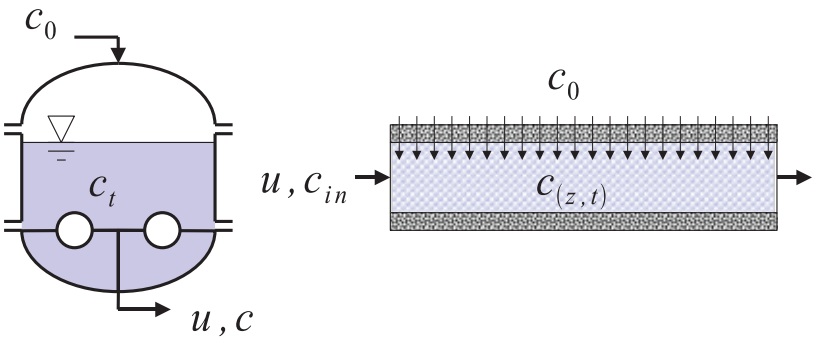

Figure 5.1: Comparison of membrane reactor and CSTR

parts: a porous tubular membrane, a catalytic fixed bed inside the tube and an empty shell side. Reactants are fed simultaneously to the fixed bed and the shell side, and could also exchange through the porous membrane. It's easy to notice two main difference between the two models:

1. The sweep gas side is also modeled, therefore the feeding concentration through membrane can not be kept constant.

2. The membrane can not be heated directly, and instead the shell of the entire membrane reactor is heated.

Besides these apparent difference, there are also some more details such as the mass transfer model incorporated the complex model, which will be explained in section 5.5.

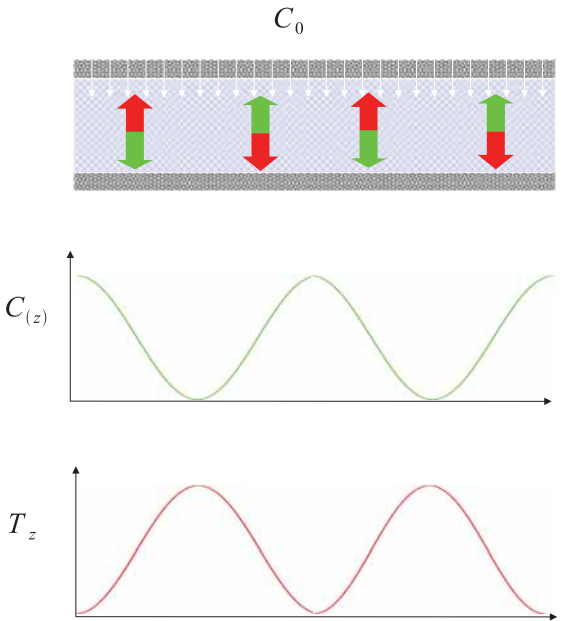

Figure 5.2: Physical interpretation of stationary pattern formation in a fixed bed membrane reactor; meaning of filled arrows: ⇑ = charging of energy storage by chemical reaction; ⇓ = discharging of energy storage by heat losses; meaning of open arrows: ⇑ = charging of mass storage by mass supply through membrane; ⇓ = discharging of mass storage by chemical reaction.

5.2 The simple membrane reactor model

One of the most important application of membrane reactor is to improve the selectivity in partial-oxidation reactions, since a proper reactant concentration is required to maintain a high conversion rate as well as high selectivity. One good example is the oxidative dehydrogenation of ethane catalyzed by $VO_x/\gamma - Al_2O_3$. The reaction was investigated by

Klose [22], and a detailed reaction kinetics with five step reaction network is identified from the experiments. The reaction network is presented in figure 5.3, and the corresponding reaction kinetics and kinetic parameters are listed in table 5.1 and 5.2. It should be noted that only reaction 1 is described by a Mars van Krevelen mechanism while the rest of reactions use a Langmuir Hinshelwood approach.

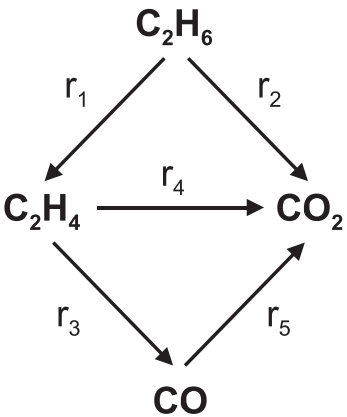

Figure 5.3: Five step reaction network of ethane partial oxidation

The reactions are supposed to be carried out in the fixed bed membrane reactor as shown in figure 2.2. In the first step, a one-dimensional pseudo-homogeneous model of the membrane reactor is studied, where the concentration and the temperature on the annulus side of the membrane reactor are assumed to be constant and identical to the (annulus) inlet conditions. The mass transfer model is also simplified to: $J_i = \beta(c_{0i} - c_i)$. By combination of fixed bed model and mass transfer model, the mass balance model for fixed bed side can be rewritten to be:

Reaction	Equation
1	$r_1 = [\frac{k_{red} c_{C2H6} k_{ox} c_{O2}^{0.5}}{k_{red} c_{C2H6} + k_{ox} c_{O2}}]$
2	$r_2 = k_2[\frac{K_{C2H6} c_{C2H6}}{1+K_{C2H6} c_{C2H6} + K_{CO2} c_{CO2}} \times \frac{K_{O2}^{0.5} c_{O2}^{0.5}}{1+K_{O2}^{0.5} c_{O2}^{0.5}}]$
3	$r_3 = k_3[\frac{K_{C2H4} c_{C2H4}}{1+K_{C2H4} c_{C2H4} + K_{CO} c_{CO}} \times \frac{K_{O2}^{0.5} c_{O2}^{0.5}}{1+K_{O2}^{0.5} c_{O2}^{0.5}}]$
4	$r_4 = k_4[\frac{K_{C2H4} c_{C2H4}}{1+K_{C2H4} c_{C2H4} + K_{CO2} c_{CO2}} \times \frac{K_{O2}^{0.5} c_{O2}^{0.5}}{1+K_{O2}^{0.5} c_{O2}^{0.5}}]$
5	$r_5 = k_5 \frac{K_{CO} c_{CO} K_{O2}^{0.5} c_{O2}^{0.5}}{[1+K_{CO} c_{CO} + K_{O2}^{0.5} c_{O2}^{0.5} + K_{CO2} c_{CO2}]^2}$

Table 5.1: Reaction kinetics for the reaction network in Figure 5.3; an Arrhenius approach is used for the rate factors, i.e. $k_i = k_{0i} \exp(E_i/R/T), \quad i = red, ox, 1, 2, \ldots, 5$. c_i represent the molar concentration of component i in mol/l at 298 K and 1 atm.

$k_{0,red} = 4.3 \times 10^9$l / kg / h	$E_1 = 94$kJ / mol
$k_{0,ox} = 1.1 \times 10^8mol^{0.5}l^{0.5}$/kg/h	$E_2 = 114$kJ / mol
$k_{02} = 1.6 \times 10^7$mol / kg / h	$E_3 = 51$kJ / mol
$k_{03} = 2.0 \times 10^4$mol / kg / h	$E_4 = 51$kJ / mol
$k_{04} = 1.0 \times 10^3$mol / kg / h	$E_5 = 118$kJ / mol
$k_{05} = 1.1 \times 10^7$mol / kg / h	
$K_{C2H6} = 4769.76$l/mol	
$K_{O2} = 1002.58$l/mol	
$K_{C2H4} = 3025.57$l/mol	
$K_{CO2} = 3455.82$l/mol	
$K_{CO} = 3233.91$l/mol	

Table 5.2: Kinetic parameters for the reaction network in Figure 5.3

$$\frac{\partial c_i}{\partial t} = -u\frac{\partial c_i}{\partial z} + \sum_{j=1}^{5} \nu_{ij} r_j \rho_{cat} + \frac{2}{r}\beta(c_{0i} - c_i), \quad i = 1, \ldots, 5 \tag{5.7}$$

An the energy balance equation becomes:

$$(\rho c_P)_{tot} \frac{\partial T}{\partial t} = -u (\rho c_P)_f \frac{\partial T}{\partial z} + \lambda \frac{\partial^2 T}{\partial z^2} + \sum_{j=1}^{5} \nu_{ij} (-\Delta_R H)_j r_j \rho_{cat} + \frac{2}{r} \alpha (T_0 - T) \quad (5.8)$$

$X_{0,C2H6}$= 0.02	$h_{C2H6,ref}$ = -84.67 J/mol
$X_{0,C2H4}$= 0.0001	$h_{C2H4,ref}$= 52.56 J/mol
$X_{0,CO}$= 0.0001	$h_{CO,ref}$ =29.14 J/mol
$X_{0,CO2}$= 0.0001	$h_{CO2,ref}$ =37.11 J/mol
$X_{0,O2}$= 0.2	$h_{O2,ref}$ =0 J/mol
$c_{P,C2H6}$ = 81.67 J / mol / K	L= 0.95 m
$c_{P,C2H4}$ = 43.56 J / mol / K	r_{out} = 0.016 m
$c_{P,CO}$ = 29.14 J / mol / K	T_0 = 848 K
$c_{P,CO2}$ = 37.11 J / mol / K	T_{ref} = 298 K
$c_{P,O2}$ = 29.355 J / mol / K	u_{in} = 0.32 m / s
α= 128 W / m^2/ K	$(\rho c_P)_{tot} = 43622$g /m^3 / K
β = 0.0934 m / s	$\rho_{Cat} = 585$kg/m^3

Table 5.3: Parameters used in the simulations with the simple membrane reactor model, if not given differently in the text.

Naturally, the same boundary conditions as in equation 2.10 and 2.10 as well as the partial molar enthalpy relations described in equation 2.8 are also applied.

In the above equations, t and z are the time and the space coordinate, respectively; u is the flow velocity of the gas; c_1 to c_5 stand for the molar concentrations of the components ethane, ethene, carbon monoxide, carbon dioxide and oxygen, respectively; ν_{ij} are the stoichiometric coefficients; r is the inner radius of the membrane; β is a mass transfer coefficient; $(\rho c_P)_{tot}$ and $(\rho c_P)_f$are the thermal capacities of the fixed bed and the gas, respectively; λ is the axial heat conductivity of the bed; α is a heat transfer coefficient. All model parameters used in the simulations are given in table 5.3.

5.3 Bifurcation analysis without heat dispersion

In this section, the simple membrane reactor model described in section 5.2 is further simplified by neglecting the heat dispersion term in equation 5.8. Obviously, the boundary condition in equation 2.10 and 2.10 can also be neglected, and the steady state mass balance and energy balance equations become:

$$u\frac{\partial c_i}{\partial z} = \sum_{j=1}^{5} \nu_{ij} r_j + \frac{2}{r}\beta\left(c_{0i} - c_i\right), c_i(0) = c_{i,in},\ i = 1, \ldots, 5 \tag{5.9}$$

$$u\left(\rho c_P\right)_f \frac{\partial T}{\partial z} = \sum_{j=1}^{5} \nu_{ij}\left(-\Delta_R H\right)_j r_j + \frac{2}{r}\alpha\left(T_0 - T\right), T(0) = T_{in} \tag{5.10}$$

The partial differential equations are converted to ordinary differential equations. As explained before, the equations describe the stationary solution of an ideal plug flow membrane reactor, which is analogous to the dynamic behavior of CSTR. The nonlinear dynamic of CSTR has been studied in detail and different kinds of behavior are classified [18]. Therefore, the next step is to look for the bifurcation points for the nonlinear behaviors in the corresponding CSTR.

5.3.1 Hopf bifurcation point

A Hopf bifurcation point appears when a fixed point of a dynamical system loses stability as a pair of complex conjugate eigenvalues of the linearization around the fixed point cross the imaginary axis of the complex plane. If the hopf bifurcation is supercritical, a small amplitude limit cycle will be formed circling the fixed point and oscillatory behavior will be observed.

The hopf bifurcation points are obtained by using one-parameter continuation method in

DIVA [49]. When the temperature of shell side is fixed to 848K, two hopf bifurcation points appear in figure 5.4 when changing the shell side concentration of ethane. The corresponding oscillatory solutions are also calculated and plotted in figure 5.4. It's obvious that the limit cycles are stable or attractive, since after the first several periods, both the amplitude and the frequency of the oscillation tends to be constant.

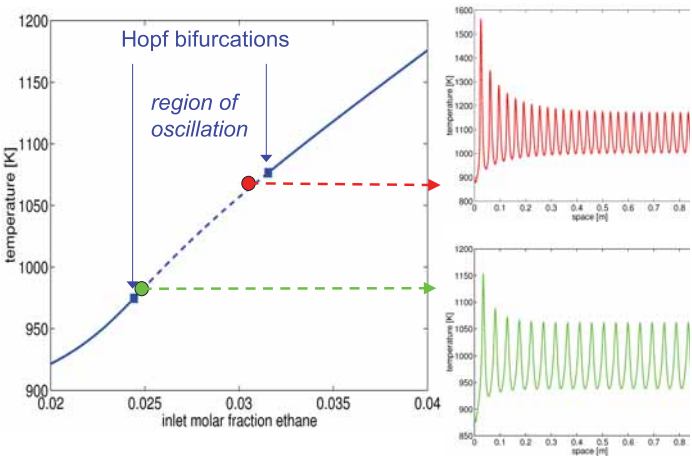

Figure 5.4: One parameter continuation of steady state membrane reactor, with all the conditions as in table 5.3 except for the shell side molar fraction of ethane. solid lines denote stable solutions, dashed lines denote unstable solutions, squares denote Hopf bifurcation points. The right-hand side graphs are the corresponding stationary pattern solution

5.3.2 Bifurcation diagram

The two-parameter continuation method in DIVA [49] is used to locate all the hopf bifurcation points according to the shell side concentrations c_{0i} and the shell side temperature T_0. The results are given in figure 5.5.

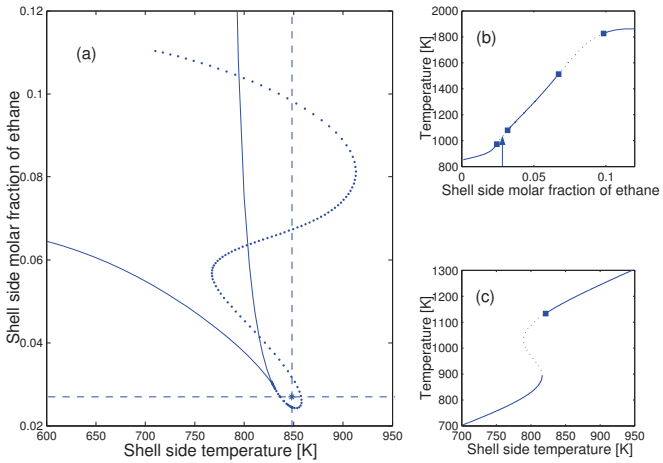

Figure 5.5: Analysis of spatially homogeneous solutions of the ideal plug flow membrane reactor; (a) saddle node bifurcations (solid lines) and Hopf bifurcations (dotted lines); (b) one parameter continuation with the shell side molar fraction of ethane as continuation parameter and a constant shell side temperature T_0 = 848 K (c) one parameter continuation with the shell side temperature as continuation parameter and a constant shell side molar fraction of ethane $x_{0,C2H6}$ = 0.04; The asterisk in (a) and the arrow in (b) indicate the simulation condition of Figure 5.8

Saddle node bifurcations are also found when the temperature and the concentration on the shell side are varied. The curve of saddle node bifurcations in figure 5.5 borders a region of multiple spatially homogeneous solutions, i.e. inside this region there are three different sets of reactor inlet conditions T_{in}, $c_{i,in}$ resulting in three different spatially homogeneous solutions for given shell side conditions. Figure 5.5 also contains information on the stability of the steady state solutions of equation 5.9 and 5.10 when moving along the space coordinate z. Stability means in this case that, as z is increased, the composition and temperature in the fixed bed approach asymptotically the homogeneous solution, i.e. the steady state solution of equation 5.7 and 5.8, if T_{in} and $c_{i,in}$ are close to but not identical to the homogeneous solution. Obviously, this notion of stability has to be distinguished from the dynamic stability of the homogeneous solutions of equation 5.7 and 5.8.

5.3.3 More complex solutions

Some more complex behavior is observed when ethene is also added into the feed. In addition to normal period-1 solutions, period-2 and period-4 solutions are also found, see figure 5.6.

Figure 5.6 even shows an aperiodic solution. The Lyapunov exponents are calculated for the solution in figure 5.6-d according to the method by Wolf et al [50], Benettin et al. [51] and Shimada [52], assuming the membrane reactor has infinite length. The three leading Lyapunov exponents found are $\lambda_1 = 0.1765$, $\lambda_2 = 0.0$, and $\lambda_3 = -3.649$, respectively. The positive Lyapunov exponent λ_1 is an indicator of deterministic chaos. The Lyapunov dimension D_L of the aperiodic attractor is calculated according to the Kaplan- Yorke conjecture [13] from:

$$D_L = 2 + \frac{\lambda_1 + \lambda_2}{|\lambda_3|} \tag{5.11}$$

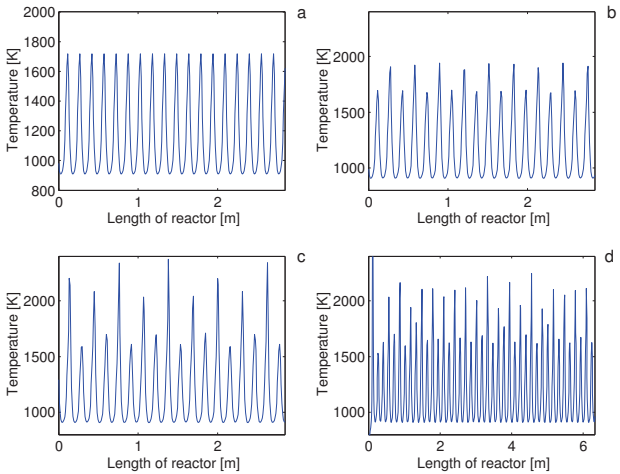

Figure 5.6: Examples of pattern solutions of the ideal plug flow membrane reactor; (a) period-1 oscillation with shell side temperature T_0 = 820 K, shell side molar fractions $X_{0,C2H6}$ = 0.02, $X_{0,C2H4}$ = 0.0313, other conditions as in Figure 5.5 (a); (b) period-2 oscillation with $X_{0,C2H4}$ = 0.0315, other conditions as (a); (c) period-4 oscillation with $X_{0,C2H4}$ = 0.0317; other condition as (a); (d) aperiodic solution with T_0 = 820.8 K, $X_{0,C2H4}$ = 0.0318, other conditions as (a).

The resulting value of D_L= 2.048 is slightly above the lower limit of 2 for chaotic attractors.

By continuation of the spatially periodic solutions, a bifurcation diagram is obtained as figure 5.7. It could be noticed that the Supercritical Flip Bifurcation (Period Doubling Bifurcation) are repeated until the chaotic solution is reached.

In conclusion, the model of steady state membrane model can show complex stationary patterns. Most of the pattern solutions are found to be beyond the realistic limit of temperature. Nevertheless, the solutions show the possibility of obtaining complex nonlinear

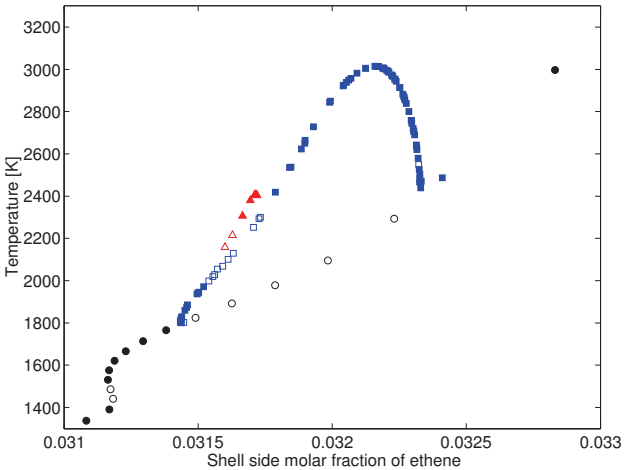

Figure 5.7: Continuation of periodic solutions of the ideal plug flow membrane reactor model; circles indicate period-1 solutions, squares indicate period-2 solutions, triangles indicate period-4 solutions; filled symbols denote stable solutions, open symbols denote unstable solutions; operation conditions on shell side: shell side temperature T_0 =820 K, shell side molar fraction of ethane $X_{0,C2H6} = 0.02$, other conditions as in Figure 5.5.

behavior in the more detailed models. As more details are included into the model, more realistic solutions could be found or verified by real experiments. In the next section, the influence of axial dispersion of heat as well as the boundary condition are taken into account and more complex behaviors are observed.

5.4 Influence of heat dispersion

In section 5.3, the special case of the membrane reactor model with stationary state and vanishing heat dispersion is investigated. In this section the full model as described by equation 5.7 and 5.8 is considered. To solve the partial differential equations, the method of lines is applied to the model equations with 4000 finite volumes, which means 20000 ordinary differential equations are to be solved simultaneously. The steady state solutions are solved by the damped Newton method NLEQ1S [53], and the dynamic behavior s are solved by the integrator DDASAC [54].

Firstly the period-1 pattern with the conditions marked at figure 5.5 is studied again. For a small enough heat dispersion coefficient λ the stationary patterns should agree with the model in section 5.3, as is proved by the simulation results in figure 5.8. The similarity of the first two graphs in figure 5.8 indicates the reasonable accuracy of the discretized model. With the increase of λ, the stationary pattern becomes more and more *smooth*, until the λ reaches a critical point where the stationary pattern can not be sustained. The critical point could be determined analytically by linearization of the original problem [16].

Secondly the influence of λ on the more complex bifurcations is investigated. In figure 5.9, the condition for a period-2 solution of CSTR is applied in membrane reactor with different λ value. It seems that λ also works like some kind of bifurcation parameter. When the value of the heat conductivity goes below some limit, the pattern solution seems to undergo bifurcations: The period of the pattern doubles suddenly for a value of λ between 0.0201 and 0.0202 W/m/K(see Figure 5.9). As the applied continuation algorithm fails for this model, the bifurcation point is located approximately by solving the steady state solution for different λ value repeatedly.

Finally the transient behavior of the membrane reactor model is also studied and some interesting solutions are found. The dynamic behavior of the system is shown in Figure 5.10

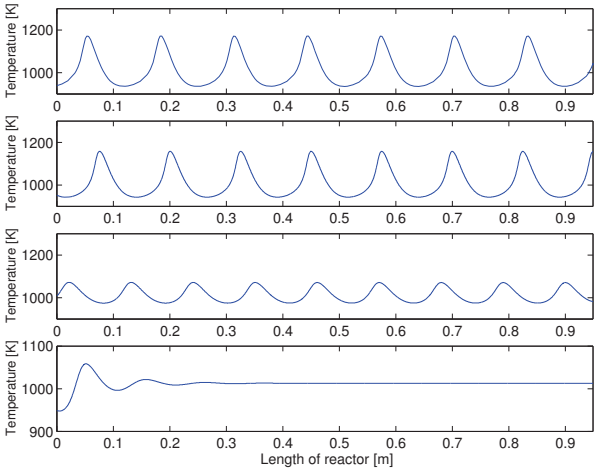

Figure 5.8: Stationary patterns of an ideal plug flow membrane reactor and of a membrane reactor model with axial heat dispersion for λ=0.1, 0.4 and 1.0 W/m/K (from top to bottom respectively); T_0=848.0K, $X_{0,C2H6}$=0.027, other parameters as in Figure 5.5.

and 5.11. A spatially homogeneous profile is used as initial condition. At the beginning of the simulation, a pattern with a rather short wavelength forms. This pattern moves in the direction of the gas flow towards the reactor outlet. The remaining stationary pattern possesses a longer wave length and a smaller amplitude.

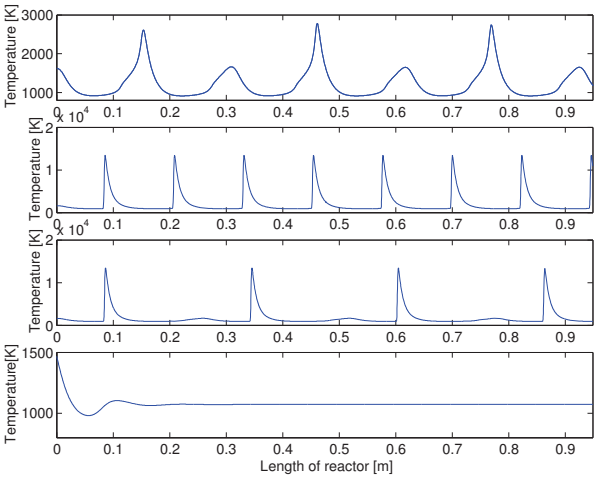

Figure 5.9: Stationary patterns of temperature for λ =0.01, 0.0201, 0.0202, 1.0 W/m/K (from top to bottom respectively) as T_0=820.0 K and $X_{0,C2H6}$=0.02 $X_{0,C2H4}$=0.0319 other parameters as in Figure 5.5.

5.5 Detailed membrane model

5.5.1 Assumptions of the detailed model

In this section, the detailed membrane reactor model as described in figure 2.2 is implemented in the process modeling tool ProMot using a model library for membrane reactors available in this software [55]. The model describes the catalytic fixed bed inside a porous membrane, the heat and mass transport through the membrane, the sweep gas side outside the membrane as well as the inlet and outlet boundary conditions. The model structure implemented in ProMot is given in figure 5.12.

The mass and energy balance for both fixed bed side and sweep gas side are already given

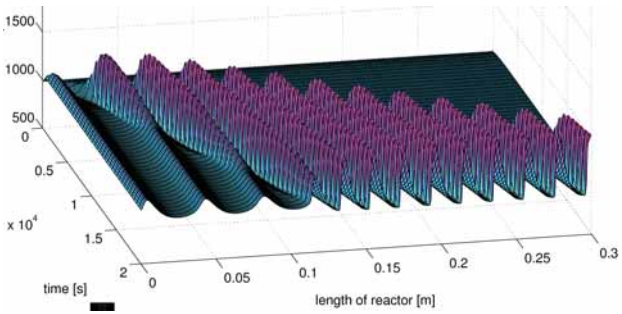

Figure 5.10: Surf plot showing the formation of a sustained pattern starting from a spatially homogeneous initial profile; T_0=848.0 K, $X_{0,C2H6}$=0.025 and λ =0.01 J/m/s all other parameter as in Figure 5.9.

in equation 2.6 to 2.12. Some of the parameters are already given in table 5.3, the new parameters are given in table 5.5.

The main differences between detailed model and simple model are:

1. In addition to the fixed bed side, the detailed model also calculates the sweep gas side.

2. In the detailed model, the experimentally identified mass transfer coefficients are applied.

3. The dependence of the heat capacities and of the total molar mass on the composition of the gases is taken into account.

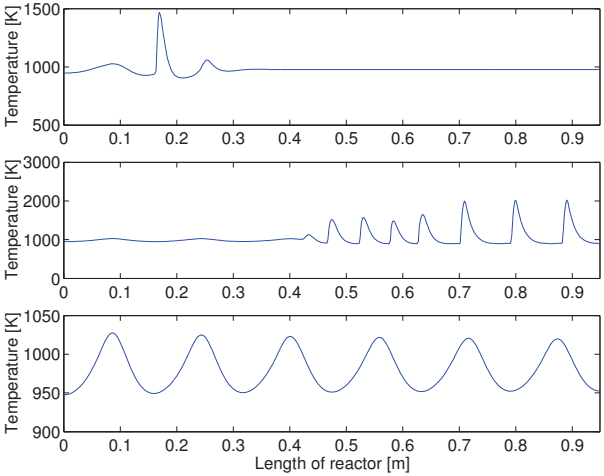

Figure 5.11: Transient pattern at time=60s, 300s, 780s, from top to bottom, respectively, all parameters as in Figure 5.10.

The mass transfer model of the membrane is identified by Hussain et al. [13]. The identified membrane model is composed of 4 layers with the mass transfer coefficients given in table 5.4. The model equations describing the mass transfer is given in section 4.2.1, for simplicity the molecular diffusion effect is not considered.

Layer i	Thickness [m]	K_{0i} [m]	B_{0i} [m^2]
1	5.5×10^{-3}	8.16×10^{-8}	2.96×10^{-14}
2	25×10^{-6}	7.99×10^{-8}	2.73×10^{-14}
3	25×10^{-6}	2.98×10^{-8}	2.88×10^{-17}
4	2×10^{-6}	2.03×10^{-9}	7.47×10^{-18}

Table 5.4: Parameters of the multi-layer ceramic membrane

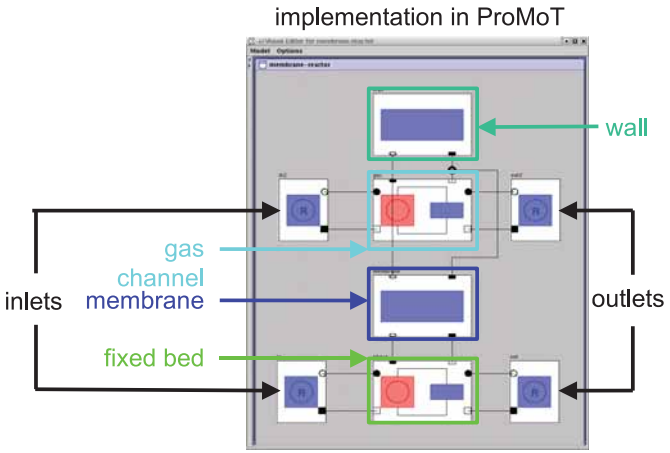

Figure 5.12: Detailed membrane reactor model implemented in ProMot

The temperature of the membrane T_{mem} is not constant now and should be calculated by

$$T_{mem} = \frac{(T_{sw} + T_{fl})}{2}, \tag{5.12}$$

where T_{sw} is the local temperature on the sweep gas side, and T_{fl} is the local temperature of the fixed bed.

The heat transfer from the sweep gas through the membrane to the fixed bed is described by

$$\dot{q} = \alpha_{mem} \times (T_{sw} - T_{fl}) \tag{5.13}$$

The effect of the heat transfer coefficient will be discussed in the following sections.

5.5.2 Simulation results

The formation of temperature and concentration patterns is also observed in the more detailed reactor model, as is shown in Figure 5.13. The pattern is very obvious in the tubular side, but on the annulus side the temperature is almost constant, and the molar fraction of ethane and ethene decreases and increases almost monotonously. In contrast to the simplified model, only patterns with decaying amplitude are found. The main reason for this may be that the concentration of the reactant ethane decreases on the sweep gas side along the reactor coordinate, which is constant in the simple model. All the parameters and conditions for the pattern formation are listed in table 5.5.

The conditions for the pattern formation are obtained by continuation of the *similar* simple membrane reactor model, since the detailed model is too big and can not use the continuation function in DIVA. Of course the similarity between the simple model and detailed model is only relative, because it's not possible to accurately represent the mass transfer through multi-layer membrane with only one parameter. However, the purpose of the research of the detailed model is not to locate the precise bifurcation points but to explore the possibility of observing such pattern in a real membrane reactor. Therefore, the study is focused on looking for the lowest possible temperature for pattern formation. As can be seen the pattern in figure 5.13 occurs at a temperature and concentration range that can possibly be obtained in a laboratory reactor.

5.5.3 Influence of the heat transfer coefficient

Another important parameter that will affect pattern formation is the heat transfer coefficient α_{mem}. However, in this simulation the identified heat transfer coefficient by Hussain [13] is not applied. Firstly the thermal conductivity λ_m only represents the heat transfer inside the membrane, but may not be enough for describing the heat transfer between

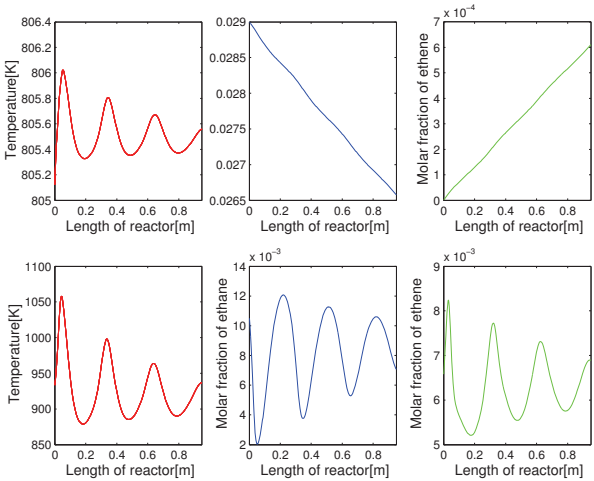

Figure 5.13: Stationary pattern for the detailed membrane reactor model. Shell side(a,b,c): T_0=805 K, $X_{0,C2H6}$=0.027, $X_{0,O2} = 0.2$ Reactor side(d,e,f): $X_{in,C2H6}$=0.97E-02, $X_{in,C2H4}$=0.65E-02, $X_{in,CO2}$=0.18E-01, $X_{in,CO} = 0.174E-01$, $X_{in,O2} = 0.196$, $X_{in,H2O}$=0.268E-01, T_{in}=928K, other parameters see table 5.5

the tubular gas and annulus gas. Secondly, the identified relationship of α_{mem} in [13] is described by equation:

$$\alpha_{mem} = -5.7372 \ln T_m + 38.853 \tag{5.14}$$

The relationship is apparently only valid within a certain temperature region, since when the temperature goes above 873.15K, the α_{mem} becomes negative which will inevitably cause the solver to collapse.

Therefore, in this simulation various values of α_{mem} are studied. The pattern turns out to be rather sensitive against α_{mem}. An increase of α_{mem} reduces the temperature level in the

$J_{Di,sw}$=$J_{Di,fl}$=1.0×10^{-8} kg/m^3/s (i = 1,...,7)	$\varepsilon = 0.5$
λ_{fl}=0.1 W/m/K	λ_{sw}=0.01 W/m/K
$T_{in,fl}$=928.0 K	α_{mem}= 60 W / m^2/ K
$T_{in,sw}$=805.0 K	α_{wall}= 140 W / m^2/ K
T_{wall}=805.0 K	r_{sw}=0.15 m
Cp, pellet=480 J/kg/K	ρ_{pellet}=1650 kg/m^3
T,pellet,ref=300.0 K	H,pellet,ref= 0.0 J/mol
u_{fl}=0.3 m/s	u_{sw}=0.3 m/s
$P_{sw,tot}$=100000 Pa	$P_{fl,tot}$=100000 Pa
$\eta = 39.16 \times 10^{-6}$N.s/$m^2$	L= 0.95 m

Table 5.5: parameters used in the detailed membrane reactor model in section 5.5 , parameters not listed are the same as in simple models; subscript 'fl' denotes fixed bed side; subscript 'sw' denotes sweep

fixed bed, especially in the inlet region, and dampens the temperature oscillations strongly. A decrease of α_{mem} causes a high temperature peak at the reactor inlet, but also reduces the oscillation amplitudes in the rear part of the reactor, see Figure 5.14. One may argue the α_{mem} set is smaller than the realistic case. In fact, the really effective parameter is not α_{mem} but the Péclet number($Pe = \frac{LV}{\alpha}$). It could be proved that if the length of the reactor is proportional to the square root of α_{mem}, the exactly same pattern could be observed in the corresponding reactor. Therefore, the pattern is still possible to be observed even for bigger α_{mem}, but only within a longer reactor.

5.6 Conclusions

The objective of this contribution is to explore the possibility of obtaining spatial stationary patterns in a membrane reactor with the selective oxidation of ethane. First an ideal plug flow reactor model is used to locate the region of parameters, where spatially periodic

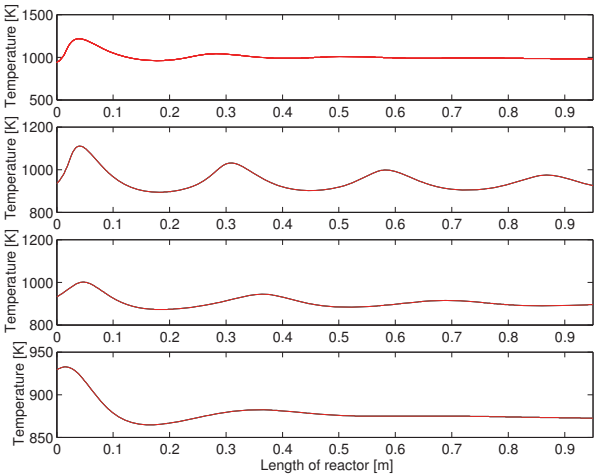

Figure 5.14: Stationary patterns for different heat transfer coefficients. 48, 56, 64 and 72 W / m2 / K respectively (from top to bottom respectively), all other parameters as in Figure 5.13

patterns may exist. As expected, many oscillatory solutions are found. The continuation method of DIVA is used to locate the region of unstable solutions. In addition to hopf bifurcation points, real bifurcation points are also found and the entire bifurcation graph with respect to shell side temperature and molar fraction of ethane is plotted.

When ethene is also supplied to the membrane reactor,quite complicated oscillatory solutions including period-1, period-2, period-4 and chaotic solutions are also found. By continuation of the oscillatory solution, the period doubling sequence is observed. As expected, a period doubling bifurcation finally leads to a chaotic solution.

In a next step, the influence of the heat dispersion is studied. When the heat dispersion

coefficient λ changes, the stationary patterns can vary both in amplitude and wave length, which indicates that λ is also an important bifurcation parameter. The transient behavior of membrane reactor model is also studied, and different kinds of stationary and transient patterns are observed.

Finally, a detailed membrane reactor model is analyzed. The simulation results show decaying stationary spatial patterns, which can be obtained in a laboratory membrane reactor under realistic operating conditions. The wave length of the patterns is in an order of magnitude that can be measured easily.

Chapter 6

Conclusion and discussion

Three different but connected problems are investigated in this work.

1. Model identification and model based optimal experimental design for the gas transport in porous membranes.

2. The global optimization algorithm, in order to solve the complex optimization problems.

3. The model simulation of a membrane reactor, focused on the pattern formation, with detailed reaction kinetics and membrane model.

In chapter 3, the problems for traditional genetic algorithm to solve optimization tasks with highly correlated parameters are discussed. An improved method with correlation analysis and coordinate transformation is developed. The method is applied to deal with the practical identification problems in chapter 4 and proves to be successful. In fact, the decorrelation method can be viewed as automatic reparametrization process. The difference of this method to traditional reparametrization method is that the task is not controlled by the modeler but finished automatically by the optimizer. And since only the optimizer part

is modified, one could expect that such method is not only limited to a certain model but also suitable for solving all global optimization problems with correlated parameters.

In chapter 4, the parameter identification and optimal experimental problems are investigated for both single and multi layer membranes. The purpose of the study of single layer membrane is to theoretically compare the effectiveness of several experimental schemes. The compared experimental schemes may be already widely applied, such as the steady state gas permeation, isobaric diffusion and transient diffusion, or just proposed in this paper, such as the single, or multi-component gas dynamic transport experiments. The results suggest the dynamic multi-component gas transport experiment provides much smaller confidence interval for identified gas transport coefficients.

The identification of a multi-layer membrane is a more complex problem. The most difficult part is the optimization of highly correlated multi-minima identification problems, the numerical solution for which is discussed in chapter 3. An ideal two-layer membrane is studied to prove the global identifiability of a multi-layer membrane. In simulation, the dynamic multi-component gas transport experiment is again found to be more efficient than the steady state single gas permeation experiment. However, such method is never tested in real experiments and the realistic dynamic model could be much more complicated than the ideal case considered in this work. Therefore the advantage of dynamic multi-component gas transport experiment for parameter identification of mass transfer coefficients is still to be investigated by real experiments.

In the end of chapter 4 a real metallic membrane is studied. The identification of mass transfer coefficients from experimental data is performed for both single-layer and multi-layer assumptions. The multi-layer model is more coherent to the experimental data, but the identified parameters still show wide confidence interval. Some experiments are designed to increase the preciseness of the identified parameters.

Chapter 5 is focused on the model synthesis and model simulation of a detailed membrane reactor. The objective of this chapter is to explore the possibility of pattern formation in the membrane reactor. Quite complicated oscillatory solutions are found for the steady state ideal plug flow membrane reactor. The influence of the heat dispersion λ is investigated, and different bifurcation for patterns is found. Finally the analysis is extended to a detailed membrane reactor with both detailed reaction kinetics and mass transfer model. The simulation results show the possibility of observing the pattern experimentally.

Appendix A

A.1 Parameter identification

A.1.1 Point estimation theory

The "parameter identification" problem is also called "point estimation" in statistic language. The objective of point estimation is to use a sample to compute parameter values which represent a good guess for the true value of some parameters. The first problem of point estimation is how to choose an appropriate estimator to make the estimation as precise as possible. We represent the vector of real parameters to be $\boldsymbol{p}$ and the estimation to be $\hat{\boldsymbol{p}}$, then the best choice of estimator $\hat{\boldsymbol{p}}$ should follow two principles:

1. The estimator should be *unbiased*, i.e. $E(\hat{\boldsymbol{p}}) = \boldsymbol{p}$.

2. The estimator should have *minimal variance*, i.e. $\min V(\hat{\boldsymbol{p}})$

The resulting $\hat{\boldsymbol{p}}$ is called the *minimum variance unbiased estimator*(MVUE) of $\boldsymbol{p}$. Unfortunately, there's no general method to derive a MVUE for any specific problem. The most commonly used estimator is called *Maximum Likelihood Estimator* (MLE), and was first introduced by R.A. Fisher in the 1920s. It can be prooved that, when the sample size is large enough, the MLE is approximately MVUE.

Let $\boldsymbol{y}$ be a vector of observed sample values which is a function of a vector of parameters $\boldsymbol{p}$. The probability given by the model, that an observed sample occurs, depends on the estimated parameter vector $\hat{\boldsymbol{p}}$, as will be shown in the next section. The probability density is expressed as $f(\boldsymbol{y}; \hat{\boldsymbol{p}})$. The MLE means to find a parameter vector $\hat{\boldsymbol{p}}$ that maximizes f for a given observation $\boldsymbol{y}$: $\arg\max f(\boldsymbol{y}; \hat{\boldsymbol{p}})$.

A.1.2 Identification criteria for dynamic model

For a dynamic parameter identification problem, suppose we have n observations measured at nt time points, and all the measurements are independent with Gaussian distribution $N(\mu_{i,j}, \sigma_{i,j}^2)$, where $\mu_{i,j}$ is the expectation of observation i at time point j, which depends on the real values of the paramter vector $\boldsymbol{p}$. Then the probability density for a single measurement is:

$$f(y_{i,j}; \boldsymbol{p}) = \frac{1}{\sqrt{2\pi}\sigma_{i,j}} e^{-\frac{(y_{i,j} - \mu_{i,j}(\boldsymbol{p}))^2}{2\sigma_{i,j}^2}} \tag{A.1}$$

and the joint probability density is:

$$f(\boldsymbol{y}; \boldsymbol{p}) = \prod_{i=1}^{n} \prod_{j=1}^{nt} \frac{1}{\sqrt{2\pi}\sigma_{i,j}} e^{-\frac{(y_{i,j} - \mu_{i,j}(\boldsymbol{p}))^2}{2\sigma_{i,j}^2}} \tag{A.2}$$

The parameter identification problem is to choose a vector of estimated parameters $\hat{\boldsymbol{p}}$ to maximize the joint probability density $f(\boldsymbol{y}; \hat{\boldsymbol{p}})$.

$$\arg\max_{\hat{\boldsymbol{p}}} \prod_{i=1}^{n} \prod_{j=1}^{nt} \frac{1}{\sqrt{2\pi}\sigma_{i,j}} e^{-\frac{(y_{i,j} - y_{m,i,j}(\hat{\boldsymbol{p}}))^2}{2\sigma_{i,j}^2}} \tag{A.3}$$

In equation A.3, $y_{m,i,j}$ is the simulated model output that should be equal to $\mu_{i,j}$.In practice, normally the logarithm function is used as criteria since it's increasing monotonically.

$$J_{ml} = \ln f(y;\hat{p}) = -\frac{1}{2}\sum_{i=1}^{n}\sum_{j=1}^{nt}\ln(2\pi\sigma_{i,j}^2) - \sum_{i=1}^{n}\sum_{j=1}^{nt}\frac{1}{2\sigma_{i,j}^2}(y_{i,j} - y_{m,i,j}(\hat{\boldsymbol{p}}))^2 \tag{A.4}$$

Generally, it's impossible to solve this maximization problem analytically, and some optimizer should be used to find the maximum. For known and constant $\sigma_{i,j}$, the MLE becomes:

$$\arg\min_{\hat{\boldsymbol{p}}} \sum_{i=1}^{n}\sum_{j=1}^{nt}\frac{1}{2\sigma_{i,j}^2}(y_{i,j} - y_{m,i,j}(\hat{\boldsymbol{p}}))^2 \tag{A.5}$$

which is exactly the same as the least squares estimator. When the amplitude of noise $\sigma_{i,j}$ is unknown, one can try to parametrize $\sigma_{i,j}$ and to estimate those additional parameters as well [56]. A common assumption is that the standard deviation of noise is proportional to the absolute value of the measurement, i.e. $\sigma_{i,j} = a|y_{m,i,j}(\hat{\boldsymbol{p}})|$, where a is the additional unknown parameter. Then the equation A.4 becomes:

$$J_{ml} = -\frac{n \times nt \ln 2\pi}{2} - n \times nt \ln a - \sum_{i=1}^{n}\sum_{j=1}^{nt}\ln|y_{m,i,j}| - \sum_{i=1}^{n}\sum_{j=1}^{nt}\frac{(y_{i,j} - y_{m,i,j})^2}{2a^2 y_{m,i,j}^2} \tag{A.6}$$

To maximize the function, notice that:

$$\frac{\partial J_{ml}}{\partial a} = -\frac{n \times nt}{a} + \frac{1}{a^3}\sum_{i=1}^{n}\sum_{j=1}^{nt}\frac{(y_{i,j} - y_{m,i,j})^2}{y_{m,i,j}^2} = 0 \tag{A.7}$$

therefore,

$$a_{ml}^2 = \frac{1}{n \times nt}\sum_{i=1}^{n}\sum_{j=1}^{nt}\frac{(y_{i,j} - y_{m,i,j})^2}{y_{m,i,j}^2} \tag{A.8}$$

Substituting a_{ml} for a in equation A.6 and dropping the constant terms, we get:

$$J_{ml} = -\sum_{i=1}^{n}\sum_{j=1}^{nt} \ln|y_{m,i,j}| - \frac{n \times nt}{2} \ln(\frac{1}{n \times nt}\sum_{i=1}^{n}\sum_{j=1}^{nt} \frac{(y_{i,j} - y_{m,i,j})^2}{y_{m,i,j}^2}) \tag{A.9}$$

It's not exactly the same as least square estimator, but for most case the first term has much smaller effect on the result than the second term. So is still very close to a least square estimator .

A.2 Bootstrap method

The bootstrap method [25] is used to measure the quality of the estimates of the parameters, such as the probability distribution or the confidence interval of the estimates. The approach is rather simple but very time consuming:

1. first a set of measurements is generated by the model with nominal parameter values $\boldsymbol{p}$, $\boldsymbol{y_m} = f(\boldsymbol{p})$

2. then some quasi-experimental data sets are generated by adding noise with zero mean and standard relative deviation, $\boldsymbol{y} = \boldsymbol{y}_m + N(0, \boldsymbol{\sigma_y y_m})$

3. finally a new set of parameters is identified by some kind of optimizer (here we test both the hybrid and the ld optimizer),

4. step 2 and step 3 are repeated, and the corresponding statistics are calculated from all the sets of identified parameters

A.3 Calculation of the sensitivity

A DAE system can be described by:

$$\boldsymbol{B}\dot{\boldsymbol{x}} = \boldsymbol{f}(\boldsymbol{x}) \tag{A.10}$$

where $\boldsymbol{x}$ is the vector of states in the system with length n, $\boldsymbol{f}$ is the length n vector of function expressions and $\boldsymbol{B}$ is a n.n matrix. $\dot{\boldsymbol{x}}$ denotes the time derivatives of the state vector $\boldsymbol{x}$: $\dot{\boldsymbol{x}} = \frac{\partial \boldsymbol{x}}{\partial t}$.The partial derivative of $\boldsymbol{x}$ for a certain parameter p is calculated by differentiation of both sides of the equation:

$$\frac{\partial(\boldsymbol{B}\dot{\boldsymbol{x}})}{\partial p} = \frac{\partial \boldsymbol{f}(\boldsymbol{x})}{\partial p} \tag{A.11}$$

In addition to the function $\boldsymbol{f}$, $\boldsymbol{x}$ and $\boldsymbol{B}$ may also depend on parameter p, the above equation must be expended to:

$$\frac{\partial \boldsymbol{B}\dot{\boldsymbol{x}}}{\partial \boldsymbol{x}}.\frac{\partial \boldsymbol{x}}{\partial p} + \frac{\partial \boldsymbol{B}\dot{\boldsymbol{x}}}{\partial p} + \boldsymbol{B}.\frac{\partial}{\partial t}(\frac{\partial \boldsymbol{x}}{\partial p}) = \frac{\partial \boldsymbol{f}}{\partial \boldsymbol{x}}.\frac{\partial \boldsymbol{x}}{\partial p} + \frac{\partial \boldsymbol{f}}{\partial p} \tag{A.12}$$

We denote the sensitivity by $\boldsymbol{s} = \frac{\partial \boldsymbol{x}}{\partial p}$, and the above equation becomes:

$$\frac{\partial \boldsymbol{B}\dot{\boldsymbol{x}}}{\partial \boldsymbol{x}}.\boldsymbol{s} + \frac{\partial \boldsymbol{B}\dot{\boldsymbol{x}}}{\partial p} + \boldsymbol{B}.\dot{\boldsymbol{s}} = \frac{\partial \boldsymbol{f}}{\partial \boldsymbol{x}}.\boldsymbol{s} + \frac{\partial \boldsymbol{f}}{\partial p} \tag{A.13}$$

For the models considered in this work, the matrix $\boldsymbol{B}$ is only composed of constants, therefore the first term of the above equation can be ignored, and the equation is simplified to:

$$\boldsymbol{B}.\dot{\boldsymbol{s}} = \frac{\partial \boldsymbol{f}}{\partial \boldsymbol{x}}.\boldsymbol{s} + \frac{\partial \boldsymbol{f}}{\partial p} \tag{A.14}$$

The above equation is incorporated into the original model system, and calculated together

by the integrator.

Bibliography

[1] Richard W.Baker, *Membrane technology*, John Wiley & Sons, Ltd, 2 Edition, 2004.

[2] C. Gijiu J. Romero, J. Sanchez, and G.M. Rios, "A unified appoach of gas, liquid and supercritical solvent transport through microporous membranes," *Chemical Engineering Science*, vol. 59, pp. 1569–1576, 2004.

[3] Petr Uchytil, Oliver Schramm, and Andreas Seidel-Morgenstern, "Influence of the transport direction on gas permeation in two-layer ceramic membranes," *Journal of Membrane Science*, vol. 170, pp. 215–224, 2000.

[4] G. Saracco, H. W.J.P.Neomagus, G.F. Versteeg, and W.P.M. van Swaajj, "High-temperature membrane reactors:potential and problems," *Chemical Engineering Science*, vol. 54, pp. 1997–2017, 1999.

[5] A. Tota, C. Hamel, S. Thomas, M. Joshi, F. Klose, and Seidel-Morgenstern, "Theoretical and Experimental Investigation of Concentration and Contact Time Effects in Membrane Reactors," *Chemical Engineering Research and Design*, vol. 82, no. 2, pp. 236–244, 2004.

[6] Sascha Thomas Frank Klose, Tania Wolff and Andreas Seidel-Morgenstern, "Operation modes of packed-bed membrane reactors in the catalytic oxidation of hydrocarbons," *Applied Catalysis A: General*, vol. 257, no. 2, pp. 193–199, 2004.

[7] Christof Hamel, Sascha Thomas, Kuno Schädlich, and Andreas Seidel-Morgenstern, "Theoretical analysis of reactant dosing concepts to perform parallel-series reactions," *Chemical Engineering Science*, vol. 58, no. 19, pp. 4483–4492, 2003.

[8] Frank Klose, Tania Wolff, Sascha Thomas, and Andreas Seidel-Morgenstern, "Concentration and residence time effects in packed bed membrane reactors," *Catalysis Today*, vol. 82, no. 1-4, pp. 25–40, 2003.

[9] C. Téllez, M. Menéndez, and J. Santamaría, "Simulation of an inert membrane reacor for the oxidative dehydrogenation of butane," *Chemical Engineering Science*, vol. 54, pp. 2917–2925, 1999.

[10] P. Capek and A. Seidel-Morgenstern, "Multicomponent mass transport in porous solids and estimation of transport parameters A: Gen.," *Appl. Catal.*, vol. 211, no. 2, pp. 227–237, 2001.

[11] A. Tuchlenski, O. Schramm, and A. Seidel-Morgenstern, "Steady state and dynamic mass transfer of gases in porous materials," *Collection of Czechoslovak Chem. Commun.*, vol. 62, no. 7, pp. 1043–1056, 1997.

[12] A. Tuchlenski, P. Uchytil, and A. Seidel-Morgenstern, "An experimental study of combined gas phase and surface diffusion in porous glass," *J. of Mem.Sci.*, vol. 140, no. 2, pp. 165–184, 1998.

[13] A. Hussain, A. Seidel-Morgenstern, and E.Tsotsas, "Heat and mass transfer in tubular ceramic membranes for membrane reactors," *J. Heat and Mass transfer*, vol. 49, pp. 2239–2253, 2006.

[14] Moshe Sheintuch and Olga Nekhamkina, "Stationary Spatially Complex Solutions in Cross-Flow Reactors with Two Reactions," *AIChE Journal*, vol. 49, no. 5, pp. 1241–1249, 2003.

[15] Tereza Trávnícková, Martin Kohout, Igor Schreiber, and Milan Kubícek, "Effects of convection on spatiotemporal solutions in a model of a cross-flow reactor," *Proceedings of CHISA 2004 Prague*, 22-26 August 2004.

[16] Olga Nekhamkina, Boris Y.Rubinstein, and Moshe Sheintuch, "Spatiotemporal Patterns in Thermokinetic Model of Cross-Flow Reactors," *AIChE Journal*, vol. 46, no. 8, pp. 1632–1641, 2000.

[17] A.Uppal and W. H. Ray, "On the dynamic dehavior of continuous stirred tank reactors," *Chemical Engineering Science*, vol. 29, pp. 967–985, 1974.

[18] A.Uppal and W. H. Ray, "The classification of the dynamic behavior of continuous stirred tank reactors=influence of reactor residence time," *Chemical Engineering Science*, vol. 31, pp. 205–214, 1976.

[19] Éric Walter and Luc Pronzato, *Identification of Parameteric Models from Experimental Data*, Springer, 1st Edition, 1997.

[20] E.A.Mason and A.P.Malinauskas, *Gas Transport in porous media: the dusty-gas model*, Elsevier, 1983.

[21] Reid Robert, C. Prausnitz, John Michael, and Bruce E Poling, *The properties of gases and liquids*, New York [u.a.], McGraw-Hill, 4.ed Edition, 1987.

[22] Frank Klose, Milind Joshi, Christof Hamel, and Adreas Seidel-Morgenstern, "Selective Oxidation of Ethane over a $VO_x/\gamma - Al_2O_3$ Catalyst - Investigation of the Reaction Network," *Applied Catalysis A*, vol. 260, pp. 101–110.

[23] M. Joshi, *Statistical analysis of models and parameters in chemical and biochemical reaction networks*, Ph.D. thesis, Otto-von-guericke-Universität Magdeburg, 2007.

[24] W. Härdle. and L. Simar, *Applied Multivariate Statistical Analysis*, Springer, 2 Edition, 2007.

[25] B. Efron and R. Tibshirani, *An introduction to the bootstrap*, Chapman & Hall, Boca Raton, 1998.

[26] Simon Haykin, *Kalman Filtering and Neural Networks*, Wiley-Interscience, 2001.

[27] U.SCHWARZ A.SITZ and J.KURTHS, "The unscented kalman filter, a powerful tool for data analysis," *International Journal of Bifurcation and Chaos*, vol. 14, no. 6, pp. 2093–2105, 2004.

[28] R. Schenkendorf, A. Kremling, and M. Mangold, "Optimal Experimental Design with the Sigma Point," *IET systems biology*, vol. accepted, 2008.

[29] E.Walter and L. Pronzato, "Qualitative and quantitative experiment design for phenomenological Models- a Survey," *Automatica*, vol. 26, no. 2, pp. 195–213, 1990.

[30] Lennart Ljung, *System Identification: Theory for the User*, Prentice Hall PTR, 2nd Edition, 1999.

[31] A.C. Atkinson and A.N. Donev, *Optimum Experimental Designs*, Oxford University Press, Oxford, 1992.

[32] Irene Bauer, Hans Georg Bock, Stefan Körkel, and Johannes P. Schlöder, "Numerical methods for optimum experimental design in DAE systems," *J. of Comp. and App. Math.*, vol. 120, pp. 1–25, 2000.

[33] Douglas C. Montgomery, *Design and Analysis of Experiments*, John Wiley & sons, 6 Edition, 2005.

[34] K. Teplinskiy, V. Trubarov, and V. Svjatnyj, "Optimization Problems in the Technological-Oriented Parallel Simulation Environment," in *18-th ASIM-Symposium Simulationtechnique*, Erlangen, 2005, pp. 582–587, SCS Publishing House.

[35] K. Teplinskiy, V. Trubarov, and V. Svjatnyj, "Optimization subsystem based on evolutionary computations for parallel simulation environment," in *First international scientific conference "Simulation and computer graphics"*, Donetsk, 2005, DonNTU.

[36] R. H. Byrd, P. Lu, J. Nocedal, and C. Zhu, "A limited memory algorithm for bound constrained optimization," *SIAM J. Scientific Computing*, vol. 16, pp. 1190–1208, 1995.

[37] M. Krasnyk, K. Bondareva, O. Mikholov, K. Teplinskiy, M. Ginkel, and A. Kienle, "The ProMoT/DIANA simulation environment," in *16th European Symposium on Computer Aided Process Engineering*. 2006, pp. 445–450, Elsevier.

[38] Thomas Bäck, *Evolutionary Algorithms in Theory and Practice*, Oxford University Press, 1996.

[39] William E. Hart and Richard K. Belew, "Optimizing an Arbitrary Function is Hard for the Genetic Algorithm," in *Proceedings of theFourthInternational Conference on Genetic Algorithms(ICGA '91)*, 1991.

[40] John H. Holland, *Adaptation in natural and artificial systems*, The University of Michigan Press, U.S.A., 1975.

[41] Darrel Whitley, "An overview of evolutionary algorithms: practical issues and common pitfalls," *informaition and software technology*, vol. 43, pp. 817–831, 2001.

[42] Cruise Scientific, *http:www.visualstatistics.net*.

[43] S. Thomas, R.Schäfer, J. Caro, and A. Seidel-Morgenstern, "Investigation of mass transfer through inorganic membranes with several layers," *Catal. Today*, vol. 67, no. 1-3, pp. 205–216, 2001.

[44] R.C. Reid, J.M. Prausnitz, and B.E. Powling, *The Properties of Gases and Liquids*, McGraw Hill, New York, 1987.

[45] P.M. Biesheuvel and H. Verweij, "Design of ceramic membrane supports: permeability, tensile strength and stress," *J. Membr. Sci.*, vol. 156, no. 1, pp. 141–152, 1999.

[46] M.Joshi, A.Kremling, and A.Seidel-Morgenstern, "Model based statistical analysis of adsorption equilibrium data," *Chem. Eng. Sci.*, vol. 61, pp. 7805–7818, 2006.

[47] K.P. Zeyer, M.Mangold, T. Obertopp, and E.D. Gilles, "The Iron(III)-Catalyzed Oxidation of Ethanol by Hydrogen Peroxide: A Thermokinetic Oscillator," *J. Phys. Chem.*, vol. 103, pp. 5515–5522, 1999.

[48] D. V. Jorgensen and Rutherford Aris, "On the dynamics of a stirred tank with consecutive reactions," *Chemical Engineering Science*, vol. 38, no. 1, pp. 45–53, 1983.

[49] M. Mangold, A. Kienle, E. D. Gilles, and K. D. Mohl, "Nonlinear computation in DIVA ? methods and applications," *Chemical Engineering Science*, vol. 55, no. 2, pp. 441–454, 2000.

[50] A. Wolf, J.B. Swift, H.L. Swinney, and J.A. Vastano., ," *Physica D*, vol. 16, pp. 285–317, 1985.

[51] A. Giogilli G. Benettin, L. Galgani and J.M. Strelcyn, "Lyapunov characteristic exponents for smooth dynamical systems and for Hamiltonian systems; a method for computing all of them," *Meccanica*, vol. 15, no. 9, 1980.

[52] I. Shimada and T. Nagashima, "A numerical approach to ergodic problem of dissipative dynamical systems," *Progress of Theoretical Physics*, vol. 61, pp. 1605, 1979.

[53] U. Nowak and L. Weimann, *A family of Newton codes for systems of highly nonlinear equations - algorithm, implementation, application. Technical Report TR 90-10*, Konrad Zuse Zentrum für Informationstechnik, Berlin, 1990.

[54] M. Caracotsios and W.E. Stewart, "Sensitivity analysis of initial value problems with mixed ODES and algebraic equations," *Computer and Chemical Engineering*, vol. 9, pp. 359–365.

[55] M. Mangold, M.Ginkel, and E.D. Gilles, "A Model Library for Membrane Reactors Implemented in the Process Modelling Tool ProMoT," *Computers and Chemical Engineering*, vol. 28, pp. 319–332, 2004.

[56] Box, G.E.P., and W.J. Hill, "Correcting inhomogeneity of variance with power transformation weighting," *Technometrics*, vol. 16, pp. 385–389, 1974.